PONTIFICIA UNIVERSIDAD CATÓLICA DE CHILE

SCHOOL OF ENGINEERING

BIOMECHANICAL ANALYSIS AND INELASTIC DEFORMABLE IMAGE REGISTRATION OF LUNG CT IMAGES

CARLOS IGNACIO ANDRADE DE BONADONA

Thesis submitted to the Office of Graduate Studies in partial fulfillment of the requirements for the Degree of Doctor in Engineering Sciences

Advisor:

DANIEL E. HURTADO SEPÚLVEDA

Santiago de Chile, March 2022

PONTIFICIA UNIVERSIDAD CATÓLICA DE CHILE

SCHOOL OF ENGINEERING

BIOMECHANICAL ANALYSIS AND INELASTIC DEFORMABLE IMAGE REGISTRATION OF LUNG CT IMAGES

CARLOS IGNACIO ANDRADE DE BONADONA

Members of the Committee:

DANIEL HURTADO

SERGIO URIBE

CRISTIÁN TEJOS

JOSÉ DELPIANO

JOSEPH M. REINHARDT

JUAN DE DIOS ORTÚZAR

Thesis submitted to the Office of Graduate Studies in partial fulfillment of the requirements for the Degree of Doctor in Engineering Sciences

Santiago de Chile, March, 2022

Dedicated to my wife Mariajosé, who unconditionally supported me during this long journey, and to my son Tommy, who unknowingly gave me the strength to finish this arduous stage of my life.

ACKNOWLEDGEMENTS

First of all, I would like to express my sincere thanks to my advisor Prof. Daniel Hurtado for his continued support during my Ph.D., for his patience, motivation, and immense knowledge. My sincere thanks also to Prof. Sergio Uribe and Dr. Jaime Retamal for their insightful comments and encouragement throughout my doctoral research. I would also like to thank my lab colleagues for the thoughtful discussions, generosity, and willingness to help whenever I needed them.

Last but not least, I would like to thank my parents and sisters for their constant concern during these years. And to my close uncles, who in one way or another supported me in different processes of my Ph.D.

TABLE OF CONTENTS

LIST OF FIGURES

LIST OF TABLES

ABSTRACT

Deformable image registration allows studying lung mechanics in a non-invasive way, providing additional information on respiratory behavior that can positively impact the diagnosis of lung-related diseases. The first part of this thesis focuses on assessing the regional deformation that occurs in normal human lungs. To this end, we combine free form deformable image registration (FFD) models with finite-element (FE) stress recovery techniques. Spatial distributions of length, surface, and volumetric deformation are estimated by computing the invariants of the right stretch tensor. Normalized maps of deformation show a common spatial pattern of deformation among all subjects studied. All three invariants of deformation display a noticeable gradient of lung deformation along the ventral-dorsal direction, highlighting the role of gravity in the normal lung under spontaneous respiration. A significant limitation showed by the B-Spline-based FFD model was the inability to account for sliding mechanisms. This issue results in misleading estimations of lung deformation near discontinuity regions. Therefore, the second part of this work introduces an inelastic deformable image registration (i-DIR) model with the ability to automatically capture sliding surfaces without any knowledge of the spatial location of discontinuous boundaries. Using an inelastic regularizer, the registration problem is thoroughly described as a variational problem. The model is validated using synthetic images and further applied to lung CT images to demonstrate its clinical applicability. The inelastic model detects regions of high shear-induced deformation associated with sliding mechanisms and locally modifies effective mechanical properties. As a result, high levels of shear deformation are allowed without adding non-physiological levels of stress in localized domains, such as boundaries and fissures of the lung. The model produces accurate local lung strain estimates similar to those reported in the literature and does not exhibit spurious oscillatory patterns near discontinuities, typically observed in B-Spline or elastic DIR methods.

RESUMEN

Los modelos de registro deformable de imágenes permiten estudiar la mecánica asociada a los pulmones de forma no-invasiva. Tienen la capacidad de medir la deformación que se desarrollan a nivel regional del tejido, proporcionar información en cuanto al correcto funcionamiento respiratorio y el potencial de mejorar el diagnóstico de enfermedades. Esta tesis se enfoca en estudiar los mecanismos de deformación regional que se desarrollan en pulmones humanos sanos usando un modelo de registro deformable de código abierto. La deformación pulmonar es descrita mediante las tres invariantes del tensor de estiramiento derecho, las cuales se asocian a deformación longitudinal, superficial y volumétrica, respectivamente. Mapas normalizados muestran un patrón espacial de deformación que es común entre todos los sujetos analizados. Los mapas de deformación asociado a las tres invariantes muestran un notorio gradiente en la dirección ventral-dorsal, destacando el rol de la gravedad durante el proceso de respiración espontánea. Sin embargo, el estudio dejó en evidencia la incapacidad del modelo de registro en capturar deslizamiento de tejido, generando errores de medición cerca de discontinuidades. La segunda parte de este trabajo presenta un modelo de registro inelástico (i-DIR) cuya característica principal es la capacidad de capturar automáticamente superficies deslizantes sin ningún conocimiento sobre la ubicación espacial de las zonas discontinuas. El modelo es validado mediante imágenes sintéticas y luego utilizado en imágenes de tomografía de tórax para demostrar su aplicabilidad clínica. El modelo inelástico detecta regiones de alta deformación inducida por cizalla, las cuales se asocian a deslizamiento, y modifica localmente propiedades mecánicas. Como resultado, el modelo permite altos niveles de deformación por cizallamiento sin agregar altos niveles de estrés en regiones localizadas, tales como las fronteras y fisuras del pulmón.

Palabras Claves: registro deformable de imágenes, inelasticidad computacional, modelamiento biomecánico pulmonar.

1. INTRODUCTION

Regardless of the nature, there is a massive concern by society and the medical community around respiratory diseases since they have been among the top leading causes of death throughout humankind's history (World-Health-Organization, 2020; Office-For-National-Statistics, 2020). The impact of respiratory diseases on public health and their relation on pulmonary mechanics has motivated the development of this thesis and the study on the biomechanical analysis of lungs based on medical images.

To answer the question: *What is biomechanics and, how does it relate to lung function?* this work begins with a quick review of lung physiology and how the field of mechanics can contribute to the study of its behavior and provide information to specialists for the diagnosis of diseases.

1.1. Lung physiology and mechanics

1.1.1. Lung physiology

In few simple words, the respiratory system is responsible for gas exchange necessary for our cells to sustain life. It is a system of organs which includes, the nose, nasal cavities, pharynx, larynx, trachea, bronchi, and lungs. The latter are vital structures much more complex than mere air sacs that inflate and deflate cyclically throughout life. From a macroscopic and microscopic perspective, the lungs are part of a complex and sophisticated system, that requires the coordinated participation of various organs. Its function is not limited to pulmonary ventilation (mechanical phenomenon) but also the distribution and ventilation/perfusion ratio, diffusion of gases between air and blood, transport of molecules of O_2 and CO_2, metabolic regulation, mechanical and cellular defense mechanisms, and hemodynamics of the pulmonary circulation (Cruz Mena & Moreno Bolton, 1999).

The basic microscopic unit where gas exchange occurs are small air sacs called *alveoli*. Gas exchange takes place thanks to the large diffusion area of 40 to 100 m^2 available in the lungs, made up of hundred of million of alveoli. These alveoli are air sacs of a diameter of $250\mu m$ surrounded by a dense layer of capillaries, where oxygen and carbon dioxide move between air and blood by simple diffusion through an extremely thin barrier (Cruz Mena & Moreno Bolton, 1999). The blood vessels surrounding the alveolar wall are so thin that a single blood cell can travel at a time, creating enormous blood exposure to the gas within the alveoli space. However, because the barrier is so thin, they can be easily damaged by the internal pressure of the capillaries or the exposure to large volumes of air in the lungs. As a result, plasma and blood cells leak into the alveolar space directly affecting the process of oxygenation (West, 2012). Therefore, the alveolar air sacs are an efficient but fragile gas exchange system.

As the name implies, the *airways* are paths that connect the alveoli with the exterior. They are made up of a sequence of branching tubular structures that become narrower until they reach the alveolar sacs. The *conducting zone* starts with the nose, acting as a front door capable of warming the air to about $37°$C thanks to a rich vascularization. Moreover, it provides an essential barrier to aerosols, thanks to the adhesiveness of the mucus layer and the presence of hairs. The mouth becomes an alternative air intake when having a nasal obstruction. The airway continues with the pharynx that connects with the larynx responsible for phonation. The larynx also contains the crucial junction of the respiratory and digestive tracts (Cruz Mena & Moreno Bolton, 1999). The airways directly associated with the respiratory process adopt a tree-like composition as shown in Figure 1.1, with the trachea as the main trunk. The trachea is then divided into a right and left main bronchus, which in turn divides into lobar and segmental bronchi. These branches continue dividing, becoming narrower until they reach the terminal bronchioles, which constitute the thinnest airways with no alveoli. From this point onward, the *conducting zone* ends. The *respiratory zone* begins with the respiratory bronchioles characterized by a sporadic presence of alveoli that sprout from their walls. The airway system ends with the gas exchange area composed of alveolar ducts filled with alveoli (West, 2012).
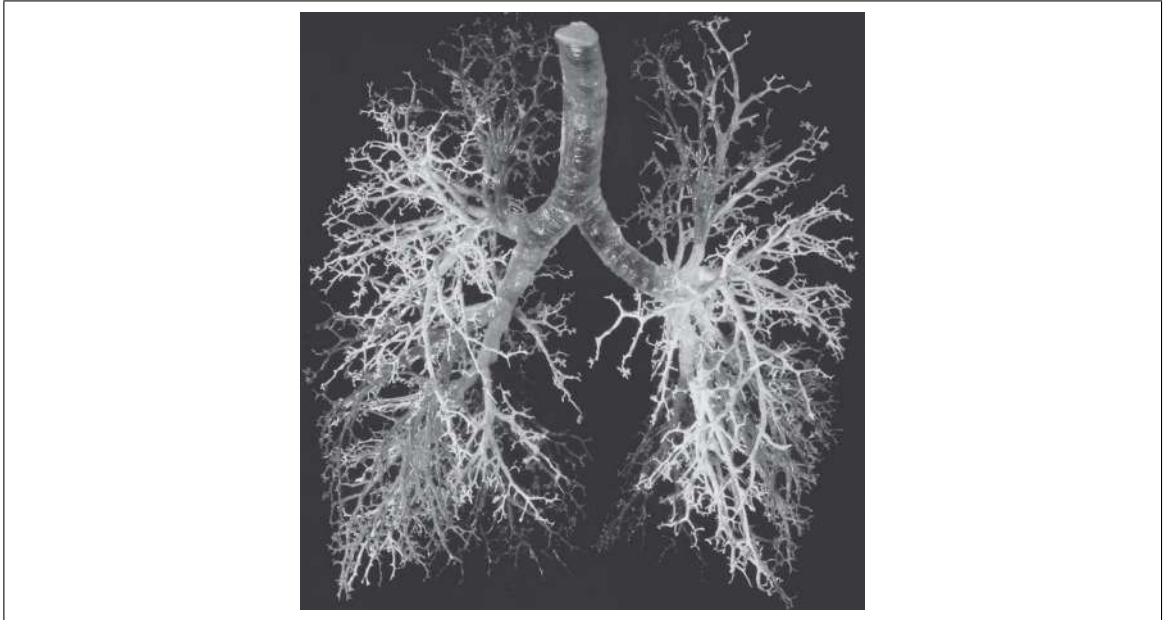
Figure 1.1. Representation of the airways within the human lung. The alveoli sacs have been removed, allowing to see the conducting airways, from the trachea to the terminal bronchioles. Image taken from (West, 2012)

From a macroscopic view, the alveolar tissue and the airways (from the distal portion of the main bronchi) are carefully arranged with a fibrous septum which confers structural support, giving rise to the left and right lung. They are independently enclosed within a double membrane called *pleura*, and between these membranes, we can find pleural fluid that serves as a lubricant, allowing the pleura to slide smoothly against each other during respiration. In humans, the right lung is shorter and broader than the left and can handle a larger volume of air. It is divided by a transverse and oblique fissures into three portions or lobes: upper, middle and lower. In contrast, the left lung is divided by an oblique fissure into two lobes: upper and lower; and has a cardiac notch where the heart accommodates (Lew, 2010; Whittemore, 2004; Cruz Mena & Moreno Bolton, 1999; Ward, 2010).

The thoracic cage is composed of a bony and cartilaginous structure, including ribs, the sternum, and thoracic vertebrae. They surround the thoracic cavity giving support to

the pectoral girdle, and due to their rigidity provide protection to all organs within the thorax. The process of lung deformation use various muscles intertwined with the rib cage. During *inspiration*, the thoracic cage expands due to the contraction of the intercostal muscles and the diaphragm, resulting in an upward and outward movement of the ribs and a downward movement of the diaphragm, respectively. When the thorax expands, the pleural surface pressure reduces relative to the atmospheric pressure, allowing the air to enter the lungs. This process, however, is not heterogeneous throughout the lung. For instance, when inspiration begins from a state of *functional residual capacity*, a person in an upright position experiences more deformation at the base of the lung (near the diaphragm). However, when inspiration follows from a state of *full expiration*, the apex of the lung (upper portion) initially undergo a more significant expansion than at the base. By contrast, *expiration* is a passive process characterized by the relaxation of the diaphragm and intercostal muscles. This results in an intrapleural pressure higher than the external pressure producing the deflation of the lungs to a resting state due to elastic recoil. The internal deformation of the lung is affected by a combination of gravitational, elastic, resistive, and inertial forces, which leads to a complex and not trivial mechanism of deformation (Cotes, Chinn, & Miller, 2006; Whittemore, 2004).

1.1.2. Lung mechanics

Spontaneous breathing is regulated and controlled by the medulla oblongata located in the upper brainstem. The control system responds to the levels of CO_2 in the bloodstream, involving an intricate interaction between chemoreceptors and mechanoreceptors scattered throughout the body. This region of the central nervous system send signals to various muscles causing a synergistic contraction in the thorax and abdomen, that results in the expansion of the rib cage (Rogers, 2011). As a result, differences in internal and external pressure arise, causing the lung to expand and relax.

Inside the pleural cavity, a thin layer of pleural liquid composed of proteins and blood cells reduces the friction between the visceral and parietal pleura. While breathing, this

allows energy dissipation and protection from shear-induced abrasion (Lai-Fook, 2004; D'Angelo, Loring, Gioia, Pecchiari, & Moscheni, 2004). As illustrated in Figure 1.2, this lubricant allows the lung to effortlessly glide freely with its surroundings and provide cohesion between the lung surface and the thoracic wall. In addition to pleural sliding, the contact surfaces between each lobe also exhibit sliding during respiration (Rodarte, Stamenovic, & Walters, 1985; Yin, Hoffman, & Lin, 2010). The absence of lung sliding may indicate the presence of pneumothorax, or it may manifest in patients with severe acute lung injury (Mallow & Isakow, 2019). Lobular and pleural gliding is a constant and intrinsic feature during normal respiration and plays a key role in lung behaviour.
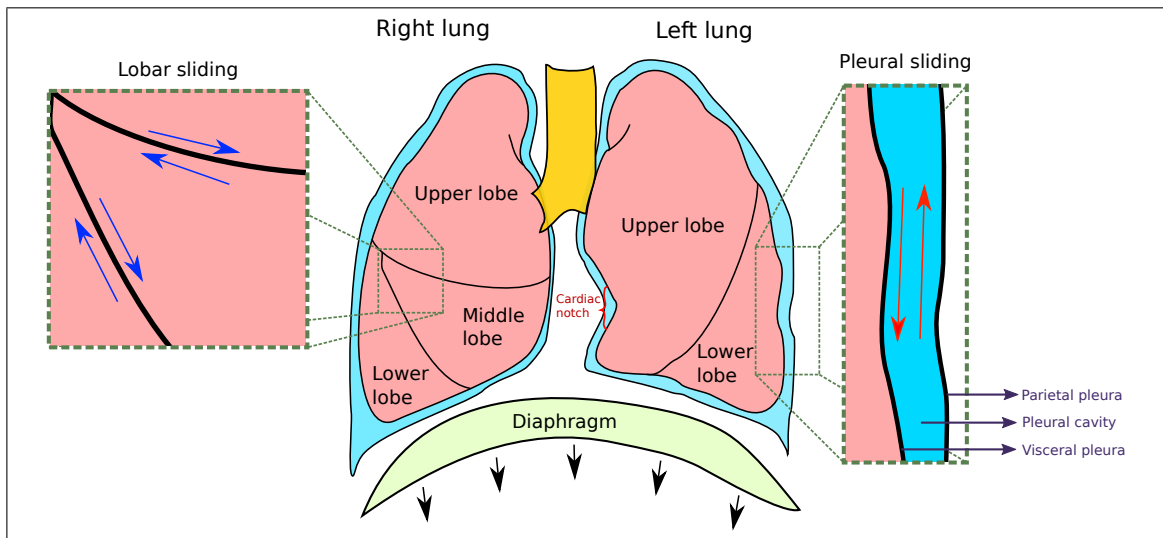
Figure 1.2. Schematics of lobar and pleural sliding in the human lung

The ability of the lung to stretch and expand can be measured by the slope of the pressure-volume curve. A particular characteristic of this curve in the lungs is that it exhibits hysteresis, that is, the trajectory that the curve follows during inspiration is different from the trajectory on expiration. The normal human lung is very distensible (easily deformed) in the normal range of pressure (expanding pressure of -5 to -10 cm water) and becomes stiffer at high expanding pressures (West, 2012). Overall the normal human lung is a very deformable organ. From a global deformation point of view, the lung can easily

accommodate twice the volume of air, that is, from a residual functional capacity of 3500 ml (resting state) it can expand to a total lung capacity of 7300 ml (Ward, 2010). Even though the lung is highly deformable, it is well known that deformation is not homogeneous inside the lung, largely due to the effect of gravity (Mitzner, 2011).

A pressure-volume curve that exceeds the typical values described for a healthy lung is sufficient evidence that the lung is not working correctly. An excessively distensible lung is a sign of loss of elastic capacity of the lung, frequently characterized by damage to the inner wall of the alveolus. In contrast, a stiff lung that cannot deform adequately suggests fibrosis or even pulmonary edema. (West, 2012, 2013). In an injured lung, structural and mechanical alterations reduce the magnitude of deformation experienced by the lung and alveoli. For example, in a common lung condition known as acute respiratory distress syndrome (ARDS), the alveoli and capillary inflammation cause a buildup of fluid within the air sacs that progressively prevent gas exchange. The large-scale manifestation is the hardening of the lung and, as a result, the inability to expand. This condition ultimately leads to a severe impact on the mechanical performance and physiological function of the lung, resulting in reduced lung capacity (abnormal compliance) (Gattinoni et al., 1998, 2006; Roan & Waters, 2011). During mechanical ventilation excessive lung deformation commonly known as ventilator-induced lung injury (VILI) can trigger damage and inflammation at the cellular level of the lungs (Dreyfuss & Saumon, 1998; Vlahakis, Schroeder, Limper, & Hubmayr, 1999). In (Retamal et al., 2018a), an experimental porcine study correlates local strain with inflammatory processes of the lung. Results show a positive spatial correlation between local strain and inflammation. Conclusions are that strain is one of the main determinants of VILI and are consistent with previous statements on the matter (Gattinoni et al., 2003; Valenza et al., 2005; Mentzelopoulos, Roussos, & Zakynthinos, 2005). The use of non-invasive (i.e., image-based) methods to measure mechanical changes within the lung can enrich our understanding of how local deformation occurs in a healthy and diseased lung, directly impacting early diagnosis. Also, improve our knowledge in VILI development and establish more conservatively and safely mechanical ventilation therapies.

1.2. Image registration

Medical imaging techniques are widely employed in medicine, with applications in treatments, diagnostics, surgical planning, and radiation therapy procedures. In general, the imaging modalities used in these applications are classified into anatomical and functional. The first group provides structural details within the body, including ultrasound, X-rays, computed tomography (CT), and magnetic resonance imaging (MRI). The second group provides information on biological behavior by providing metabolic information from the underlying anatomy. Common functional modalities include single-photon emission computed tomography (SPECT), positron emission tomography (PET), and functional magnetic resonance imaging. The integration of images from different modalities or acquired at different time periods provides useful information to improve the ability to identify lesions, influence treatment decisions, and patient management. This requires a process of spatial image alignment commonly known as *image registration* (Maintz & Viergever, 1998; Crum, Hartkens, & Hill, 2004; Viergever et al., 2016).

Image registration aims to find an optimal spatial transformation capable of correlating information in one image with others. In practice, no measurement is completely accurate and there is some error or tolerance associated with this estimated match, especially on finer scales (Hajnal, Hawkes, & Hill, 2001). The above gives the transformation a quality of asymmetry, where there is no guarantee that a point in one image can be related to its corresponding location in the other (Crum et al., 2004).

According to Crum and coworkers, image registration requires the definition of three elements: a *similarity measure*, a *transformation model*, and an *optimization algorithm* (Crum et al., 2004).

The similarity measure quantifies the difference between the images to be aligned. The similarity metric of choice depends on the application. These include the *sum of squared differences (SSD)*, *cross-correlation (CC)*, and *mutual information (MI)* or *normalized mutual information (NMI)*. SSD assumes that the tissues have the same intensities between

images, as in the case of mono-modal applications. CC used in multimodal registration assumes that the intensities within the images have a linear relationship. MI/NMI used for multimodal applications arises from information theory and seeks to minimize the joint entropy of gray values within images (Schmidt-Richberg, 2014; Crum et al., 2004).

The transformation model describes how an image is modified to align it with the others and characterize it by the number and type of deformations. The number of parameters that are used to define the spatial transformation during registration is called the number of degrees of freedom (DOF). Depending on the deformations they capture, the transformation models can be classified into: rigid and nonrigid (Hajnal et al., 2001). Rigid registration originates from the definition of rigid-body transformation and is the simplest form of image registration. Rigid models have global DOF that includes translational and rotational transformation. However, by definition, these parameters are expanded to describe scaling and shear deformation, as in *affine transformations* (Hajnal et al., 2001). Specifically, rigid registration is well suited to handle minor changes between the images, as in the case of structures with rigid morphological attributes such as brain images (Crum et al., 2004). By contrast, nonrigid models also known as *Deformable Image Registration (DIR)* models are adequate to characterize soft tissue deformation. Unlike rigid registration, nonrigid models allow a non-linear form of local deformation in the tissue. Usually, penalty terms or constraints must be considered to confer a physically plausible deformation in DIR models. These constrains, however, depend on the application at hand (Hajnal et al., 2001). Having more degrees of freedom, though, comes at some expense. The more parameters involved in the process, the higher the computational cost, both in memory consumption and computing time. Rigid registration takes a very small fraction of time compared with nonrigid models to estimate results (Crum et al., 2004). Nonrigid models often need a good initial estimation in order to have proper convergence. Several algorithms include a preliminary registration using rigid transformations followed by a nonrigid transformation model (Maintz & Viergever, 1998).

The registration model can be formulated as an optimization problem that seeks to measure the "optimal" transformation that maps one image onto another. This process aims to minimize a cost or objective function. Usually, DIR models are ill-posed because they do not have a unique solution or the solution may be too sensitive to input data, i.e. image noise (Abidi & Singh, 2020). To address this issue, in addition to a similarity distance, the objective function must consider an additional energy term that acts as a *regularizer* which constrains the domain of valid deformations. In most cases, the optimization process starts with an initial guess close enough to converge on an accurate result. Then the registration algorithm computes the similarity function and evaluates how well the images align. The procedure continues through an iterative process until achieving an optimal registration. This is done by processing several transformations that increase (or decrease) the objective function until reaching a maximum (or minimum) tolerance (Hajnal et al., 2001). Deciding the optimization strategy suitable for a particular application depends on the objective/cost function, the transformation model, the constraints, and the accuracy requirements (Crum et al., 2004).

1.2.1. A variational approach for deformable image registration (DIR)

This thesis aims to add physiologically plausible transformations to the image registration process. A particular type of registration model based on elastic deformations of the body helps to engage the challenge. By providing material properties using the Lamé parameters, the image domain is modeled as an elastic solid based on the Navier-Cauchy equations (Broit, 1981; Schmidt-Richberg, 2014). In such cases, the cost function becomes an energy functional. The image similarity metric acts as an external force and an elastic penalty term acts as an internal regularization force. The balance of these forces drives the deformation within the image. Typically, the solution of such type of registration techniques is computed by the minimization of the energy functional (Crum et al., 2004).

Following the mathematical approach set forth in (Modersitzki, 2003), the purpose of this section is to define a general framework of the registration problem, which lays the basis for an elastic formulation described in Section 3.2.1. The first step is to define the registration problem using a variational formulation that seeks to minimize a DIR functional. It is important to mention that although digital images are discrete domains that live in the space defined by the set of all integers ($\mathbb{Z}$), in this thesis, the images will be defined within the domain of the reals ($\mathbb{R}$). In this way, let $\Omega \subset \mathbb{R}^n$ be a domain of interest (i.e. image domain), where $R : \Omega \longrightarrow \mathbb{R}$ is a *reference* (fixed) image and $T : \Omega \longrightarrow \mathbb{R}$ a *target* (moving) image. Then a transformation mapping $\boldsymbol{\varphi} : \Omega \longrightarrow \mathbb{R}^n$ is defined, such that $T_\varphi(\boldsymbol{x}) := T(\varphi(\boldsymbol{x}))$ resembles $R(\boldsymbol{x})$, with $\boldsymbol{x} \in \Omega$. Conveniently, the deformation mapping field can be expressed in terms of a displacement field $\boldsymbol{u} : \Omega \longrightarrow \mathbb{R}^n$, such that

$$\varphi(\boldsymbol{x}) = \boldsymbol{x} + u(\boldsymbol{x}) \qquad \forall \boldsymbol{x} \in \Omega. \tag{1.1}$$

In medical imaging, an important assumption when using images of the same patient and acquired in short periods of time is to conceive $\boldsymbol{\varphi}$ as a diffeomorphic transformation. Diffeomorphic transformations are advantageous since they preserve the topology of the deformation (tissue folding is not allowed). They are characterized by a continuous and smooth bijective mapping field, with derivatives that are invertible (i.e., nonzero Jacobian)(Ashburner, 2007). Next, let $\mathcal{V} := \mathrm{H}^1(\Omega, \mathbb{R}^n)$ be a functional space, where a similarity metric $\mathcal{D} : \mathcal{V} \longrightarrow \mathbb{R}$ helps to seek the minimum distance (minimum dissimilarity) between R and $T_{\boldsymbol{u}}$ with respect to the displacement field $\boldsymbol{u}$,

$$\mathcal{D}[R, T; \boldsymbol{u}] := \mathcal{D}[R, T_{\boldsymbol{u}}] \xrightarrow{\boldsymbol{u}} \min \tag{1.2}$$

with $T_{\boldsymbol{u}} := T(\boldsymbol{x} + u(\boldsymbol{x}))$. As stated earlier, in practice a direct minimization of $\mathcal{D}$ is ill-posed leading to several drawbacks (e.g., no unique solution). Therefore, it is convenient to include a penalty term $\mathcal{S} : \mathcal{V} \longrightarrow \mathbb{R}$ which ensures a smooth transformation. Now, it is possible to define the registration problem as an energy minimization functional. The problem reads: *Given two images: R and T; and a positive scalar weighting parameter*

$\alpha \in \mathbb{R}^+$, *find a displacement field $\boldsymbol{u}$, such that*

$$\Pi[\boldsymbol{u}] := \alpha \mathcal{D}[R, T; \boldsymbol{u}] + \mathcal{S}[\boldsymbol{u}] \xrightarrow{\boldsymbol{u}} \min \qquad (1.3)$$

Traditional choices of elastic regularization are based on symmetric bi-linear forms of $a : \mathcal{V} \times \mathcal{V} \longrightarrow \mathbb{R}$, with $\mathcal{A} : \mathcal{V} \longrightarrow \mathcal{V}'$ as a partial differential operator, such that $a[\boldsymbol{u}, \boldsymbol{v}] :=< \mathcal{A}\boldsymbol{u}, \boldsymbol{v} >$. Given this understanding of bi-linearity, the regularizing term becomes

$$\mathcal{S}[\boldsymbol{u}] := \frac{1}{2} a[\boldsymbol{u}, \boldsymbol{u}] \qquad \forall \boldsymbol{u} \in \mathcal{V}. \qquad (1.4)$$

By now, the minimization functional becomes

$$\min_{\boldsymbol{u} \in \mathcal{V}} \Pi[\boldsymbol{u}] = \min_{\boldsymbol{u} \in \mathcal{V}} \alpha \mathcal{D}[R, T; \boldsymbol{u}] + \frac{1}{2} a[\boldsymbol{u}, \boldsymbol{u}] \qquad \forall \boldsymbol{u} \in \mathcal{V} \qquad (1.5)$$

A helpful way to solve (1.5), consists in finding the Gateaux derivatives of $\Pi[\boldsymbol{u}]$ for all suitable perturbations $\boldsymbol{v} \in \mathcal{V}$, such that

$$d\mathcal{S}[\boldsymbol{u}; \boldsymbol{v}] := a[\boldsymbol{u}, \boldsymbol{v}] = \int_{\mathbb{R}^n} < \mathcal{A}[u](\boldsymbol{x}), v(\boldsymbol{x}) >_{\mathbb{R}^n} dx \qquad (1.6)$$

and

$$d\mathcal{D}[R, T, \boldsymbol{u}; \boldsymbol{v}] := F_{\boldsymbol{u}}(\boldsymbol{v}) = \int_{\mathbb{R}^n} < f(\boldsymbol{x}, u(\boldsymbol{x})), v(\boldsymbol{x}) >_{\mathbb{R}^n} dx. \qquad (1.7)$$

The term $F_{\boldsymbol{u}} : \mathcal{V} \longrightarrow \mathbb{R}$ is linear given $\boldsymbol{u}$ and represents the so-called force f, which depends on the similarity measure. These first order conditions (1.6), (1.7) gives rise to the following non-linear problem: *Find $\boldsymbol{u} \in \mathcal{V}$, such that*

$$a[\boldsymbol{u}, \boldsymbol{v}] = \alpha F_{\boldsymbol{u}}(\boldsymbol{v}) \qquad \forall \boldsymbol{v} \in \mathcal{V} \qquad (1.8)$$

The preceding definition constitutes the simplest form of a variational framework associated with the registration problem. A variety of numerical schemes can be applied to find its solution, such as gradient-based descent methods or even higher order schemes (e.g., Newton-Raphson method)(Modersitzki, 2003; Barnafi, Gatica, & Hurtado, 2018).

1.3. Image-based quantification of pulmonary deformation

The gold-standard in the assessment of lung respiratory function is spirometry. This test uses a spirometer, an instrument that provides relevant information on impaired respiratory function by measuring *tidal volume* and *vital capacity*. However, given the global measurements found in these types of instruments, they cannot determine how the lung is deformed locally (West, 2012). The use of image-based techniques brings relevant data related to the spatial heterogeneity of the lung's deformation. One of the first attempts in measuring local lung deformation date back to the work of Rodarte et al., where lead markers were implanted percutaneously in the lung parenchyma of adult dogs and then tracked using fluoroscopic signals. Their results suggest that an important interaction between the lung and thoracic cage exists and that thoracic cavity shape is an important determinant of regional volume distribution. However, according to the authors, without a better definition of the lobe shape and the location of the interlobar surfaces, the displacement in these surfaces and its importance with respect to the stress and volume distributions cannot be determined (Rodarte et al., 1985).

The need of a regional assessment of lung deformation motivated the development of computational techniques and improved imaging equipment. Today, image registration techniques allow for the assessment of displacement fields from two ventilatory levels (i.e. inspiration and expiration), providing useful information of the complex mechanisms of lung deformation. Variants of image registration methods that allows for the quantification of regional deformation in the lungs are deformable image registration (DIR) models (see Figure 1.3). In DIR, the lung tissue is assumed to be a continuum subject to continuous (and differentiable) deformation fields (Reinhardt et al., 2008; Amelon, Cao, Reinhardt, Christensen, & Raghavan, 2012; Jahani et al., 2015). Using non-rigid image-based registration techniques, Reinhardt and coworkers measured lung expansion (volumetric change) in sheeps by means of the Jacobian. Later, using human lung CT images the authors characterized regional lung deformation by quantifying: a) the Jacobian (J), b) the anisotropic deformation index (ADI), which measures the magnitude of the orientational

preference of volume change and c) the slab-rod index (SRI), which is a measure of the nature of directional preference in the volume change. These three indexes were selected so that different, but complimentary features of regional lung deformation could be identified independently. Results showed that for different subjects, spatial distribution can be highly non-homogeneous in terms of J, ADI and SRI. In terms of J, subjects presented high values at the dorsal-inferior regions, suggesting a localized region of high volumetric change (Amelon et al., 2011). Abnormally high values of ADI were present in the fissures of the lung, which has been attributed to registration artifacts and the inability of the DIR method to capture lobar sliding without resulting in spurious shear deformation (Amelon et al., 2012; Amelon, Cao, Reinhardt, Christensen, & Raghavan, 2014).
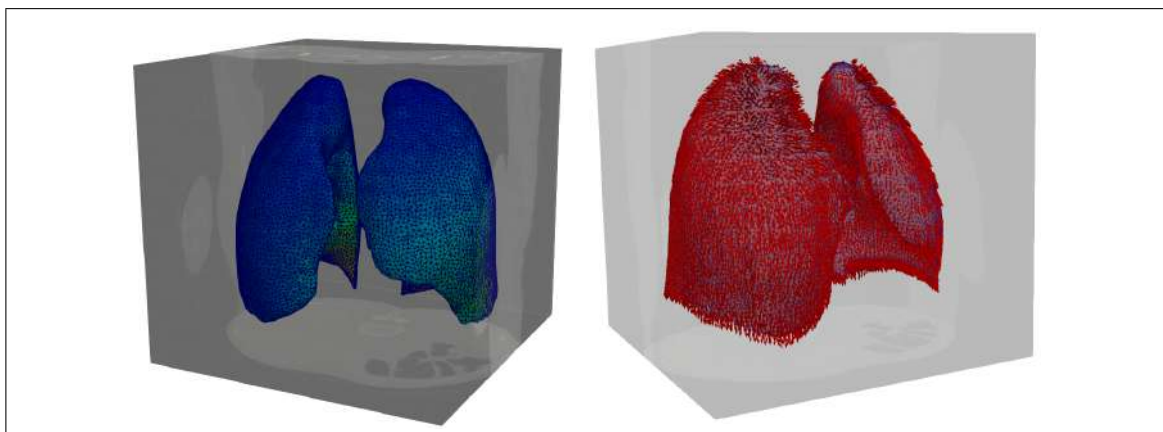
Figure 1.3. 3D visualization schematics of regional deformation in human lungs, computed from image-based registration models. *Left:* strain fields interpolated over a tetrahedral finite element mesh. *Right:* displacement field vectors overlapped on a finite element mesh.

To improve the accuracy and robustness of DIR-based biomechanical analysis, (Hurtado, Villarroel, Retamal, Bugedo, & Bruhn, 2016) introduced a computational method for the analysis of regional deformations based on finite element (FE) projections. The combination of non-rigid registration, FE interpolation and a variational recovery approach show that regional strain maps in synthetic images, and in particular volumetric strain, result in more accurate predictions without spurious oscillations. With

this method, the levels of ADI deformation around lobar fissures are reduced. However, it still remained high compared to regions without sliding surfaces, as one of the main assumptions of the method is the continuity of displacement fields (Hurtado et al., 2017). In spite of the novel methods described above, DIR methods for image-based biomechanical analysis of lungs are far from perfection and several limitations are evidenced. For example, registration methods based on B-Splines interpolations cannot capture material interfaces due to the complex organ geometry. This results in misleading image registration errors, directly affecting regional lung deformation estimations, which possess no physiological basis (Amelon et al., 2011; Hua, Pozo, Taylor, & Frangi, 2015; Hurtado et al., 2017; Al-Mayah, Moseley, Velec, & Brock, 2009; Ding et al., 2009). While there are some promising attempts that incorporate additional constraints that accounts for organ sliding (Hua et al., 2015; Pace, Aylward, & Niethammer, 2013; Delmon, Rit, Pinho, & Sarrut, 2013; Schmidt-Richberg, Werner, Handels, & Ehrhardt, 2012), several limitations are evidenced that preclude them from their direct applicability to the analysis of regional strain deformation in tissue. Moreover, despite the advances in terms of biomechanical quantification in lungs, most studies have been focused on volumetric changes, and they do not include any other metric that describes the energy of a solid (i.e. preferential orientation of deformation). In this context, a promising research area is an image-based method for biomechanical analysis of the lung that may include other deformation metrics (e.g., length and surface deformation), along with the ability to capture sliding on irregular geometries such as pleural space and lobe fissures without a priori knowledge of the position of such discontinuities.

1.4. Objectives

Due to the complex nature of lung kinematics, where lobular and pleural sliding play a key role in regional lung deformation, questions arise: Are there any additional metrics, other than volumetric deformation, that might help describe regional strain in the lungs? Is it possible to capture the deformation mechanisms that reveal lobular and pleural sliding

within the image registration process? This doctoral thesis aims to answer these questions by studying the spatial patterns of distributions of regional lung deformation in normal lungs and developing an inelastic deformable image registration model capable of capturing tissue sliding.

1.5. Thesis structure

The structure of this thesis is as follows: Chapter 2 describes the study of spatial distributions of regional deformation in normal lungs using computed tomography (CT) images. It introduces the mechanical framework of how regional deformation is measured and presents a novel score that facilitates a better inter-subject comparison. Chapter 3 describes the theory, motivation, and development of an inelastic deformable image registration (i-DIR) model that can automatically detect sliding surfaces, which has direct applicability in the analysis of deformation mechanisms on lung CT images. Chapter 4 summarizes the conclusions and future work relevant to the biomechanical analysis of lungs.

2. SPATIAL DISTRIBUTION OF REGIONAL DEFORMATION IN NORMAL HUMAN LUNGS

Abstract Understanding regional deformation in the lung has long attracted the medical community, as parenchymal deformation plays a key role in respiratory physiology. Recent advances in image registration make it possible to noninvasively study regional deformation, showing that volumetric deformation in healthy lungs follows complex spatial patterns not necessarily shared by all subjects, and that deformation can be highly anisotropic. In this work, we systematically study the regional deformation in the lungs of eleven human subjects by means of in vivo image-based biomechanical analysis. Regional deformation is quantified in terms of 3D maps of the invariants of the right stretch tensor, which are related to regional changes in length, surface and volume. Based on the histograms of individual lungs, we show that log-normal distributions adequately represent the frequency distribution of deformation invariants in the lung, which naturally motivates the normalization of the invariant fields in terms of the log-normal score. Normalized maps of deformation invariants allow for a direct intersubject comparison, as they display spatial patterns of deformation in a range that is common to all subjects. For the population studied, we find that lungs in supine position display a marked gradient along the gravitational direction not only for volumetric but also for length and surface regional deformation, highlighting the role of gravity in the regional deformation of normal lungs under spontaneous breathing.

2.1. Introduction

The ability of lung tissue to cyclically deform is fundamental to life, as tens of millions of respiratory cycles are needed during a lifetime to uninterruptedly supply the lungs with air for gas exchange. The underlying mechanisms of lung deformation and its relation to airway flow and alveolar ventilation during breathing have long attracted respiratory physiologists. Indeed, the quantitative characterization of functional parameters that describe the global biomechanical behavior of the lung constitutes the basis for many tests

routinely performed in the clinical practice to study pulmonary function and diagnose respiratory disease in patients, such as the spirometry and gas diffusion tests (West, 2012). Despite the usefulness of current pulmonary function tests, there is an increasing interest in obtaining respiratory functional information at a regional level, as global pulmonary parameters are not capable of detecting the onset of several pathologies. One particular example is chronic obstructive pulmonary disease, a progressive disease that severely diminishes pulmonary capacity. It has been shown that the measurement of emphysema through a regional intensity analysis of CT images can be more sensitive than spirometry, reducing the number of false negatives as well as allowing for earlier diagnosis (Spaggiari et al., 2005; Lynch & Newell, 2009).

Deformable image registration based on computed tomography (CT) imaging of the lung provides a noninvasive tool to study the motion and deformation of the lung at a regional level (Sotiras, Davatzikos, & Paragios, 2013a). Using a continuum mechanics approach a handful of attempts have been made to study the regional deformation of the human lung parenchyma from chest CT images, predominantly focussing on volumetric change (Christensen, Song, Lu, El Naqa, & Low, 2007; Reinhardt et al., 2008; Jahani, Yin, Hoffman, & Lin, 2014). (Amelon et al., 2011) proposed the use of deformation-based indices to characterize the anisotropy of regional deformation in six human healthy subjects. In a larger study, (Choi et al., 2013) employed image registration tools to quantitatively study the regional distribution of volumetric deformation, air volume change and the anisotropic deformation index for 14 normal subjects and 30 severe asthmatics. When comparing between normal and severe asthmatic populations, they were able to describe significant regional differences in anisotropy and air volume change, demonstrating the potential of image-based biomechanical analysis in distinguishing normal from diseased lungs. In chronic obstructive pulmonary disease, the spatial distribution, anisotropy and magnitude of regional volumetric strain has been shown to be significantly different depending on the level of severity of the disease (Bodduluri, Newell, Hoffman, & Reinhardt, 2013). In the case of ventilator-induced lung injury, local parenchymal inflammation has

been shown to develop proportional to the regional tidal volumetric strain induced by mechanical ventilation (Wellman et al., 2014) and may occur even in cases where global values of tidal volumetric strain are below what is considered to be critical (Paula et al., 2016).

As the examples mentioned above clearly confirm, a quantitative characterization of the regional lung mechanics does have profound medical implications. We note that, to date, regional characterization of lung mechanics has mainly focussed on volumetric deformation and anisotropic indices for deformation. Biomechanical testing has shown that parenchymal tissue displays a marked isotropic constitutive behavior (Hoppin, Lee, & Dawson, 1975), which has been also suggested based on the randomly oriented microstructural arrangement of collagen and elastin fibers observed through electron microscopy (Mercer & Crapo, 1990). Considering the hyperelastic behavior, and the isotropic architecture of lung tissue, it can be shown that the deformation energy density, and the constitute response in general depends not only on the local volumetric deformation, but also on other deformation invariants of the stretch tensor that are related to surface and length deformation (Ogden, 1984). Further, mechanical testing of lung tissue samples has revealed that not only volumetric deformation, but also length deformation governs the constitutive response of the lung parenchyma (Rausch, Martin, Bornemann, Uhlig, & Wall, 2011). Thus, from a biomechanical perspective, the spatial characterization of not only regional volumetric deformation, but also invariants related to the surface and length deformation are crucial to better understand lung mechanics. Further, a complete in vivo quantification of relevant metrics of local deformation in terms of invariants may serve as validation to continuum constitutive models of lung parenchyma (Freed & Einstein, 2012).

In light of the clinical and biomechanical relevance of regional deformation in the lung, the fundamental question that motivates this investigation is: Do regional deformation metrics in healthy human lung parenchyma follow common spatial pattern, or frequency distribution that can be quantitatively described? In this work, we study the spatial patterns and distribution of relevant deformation metrics of regional deformation in 11

healthy human subjects. To this end, we use the image-based finite-element biomechanical analysis introduced by the authors in a previous contribution (Hurtado, Villarroel, et al., 2016), which has been shown to drastically improve the accuracy of regional deformation estimates. With the resulting regional maps of deformation, we perform an analysis of possible spatial patterns and frequency distributions of different measures of deformation.

2.2. Materials and methods

Eleven healthy subjects, 2 females and 9 males, were recruited for this study and underwent a protocol approved by the institutional review board of the Pontificia Universidad Católica de Chile. All subjects declared to be non-smokers and did not report any pulmonary disease or condition at the time of the study, nor that they have suffered any major illness in the past that could leave a lung sequelae (e.g., pneumonia). Complete information about the age, gender and other anthropometric data for the population studied is included in Table 2.1. Two CT thorax data sets were acquired in all subjects who remained in supine position during the entire acquisition time. First, subjects were directed to take a full inspiration (total lung capacity, TLC) and hold their breath for the first image acquisition. Then, a spontaneous expiration (functional residual capacity, FRC) was directed for the second image acquisition. The size of the CT images at TLC and FRC was $512 \times 512 \times 285$ voxels, with a voxel spatial resolution of 0.73[mm], 0.73[mm] and 1.25[mm] in the x, y, z direction, respectively. In all subjects, the data acquisition was performed using a CT scanner (LightSpeed VCT, GE Healthcare, UK) with the following settings: collimation, 1.25; interval, 1.25[mm]; bed speed, 27.5[mm] per second; voltage, 100[kV]; and current, 150[mA].

Table 2.1. Anthropometric information of the population studied. TLC and FRC are computed from CT image analysis

Subject	Gender	Age (yr)	Weight (kg)	Height (m)	BMI $\left(\frac{\text{kg}}{\text{m}^2}\right)$	TLC (L)	FRC (L)
S01	M	30	73	1.80	22.5	5.68	2.97
S02	M	31	61	1.65	22.4	5.93	2.71
S03	M	35	85	1.80	26.2	6.21	3.09
S04	M	25	75	1.83	22.4	5.84	3.16
S05	M	26	84	1.84	24.8	8.07	2.41
S06	F	30	70	1.69	24.5	5.15	1.59
S07	M	22	66	1.73	22.1	5.31	2.71
S08	M	32	89	1.65	32.7	6.06	2.04
S09	M	43	76	1.71	26.0	5.56	3.83
S10	F	24	62	1.70	21.5	4.91	1.97
S11	M	25	71	1.72	24.0	7.53	2.64
	Mean	29.4	73.8	1.74	24.5	6.02	2.65
	Std	6.0	9.2	0.07	3.2	0.97	0.63

M: Male, F: female, BMI: body-mass index, TLC: total lung capacity, FRC: functional residual capacity.

To study the regional deformation in lung parenchyma, we adopt a nonlinear continuum mechanics framework (Ogden, 1984). Because FRC is associated with a resting state of the diaphragm and other respiratory muscles that can be naturally achieved by all healthy subjects, we consider the domain of the lung at FRC as the *reference configuration*, represented by the open set $B \in \mathbb{R}^3$. Likewise, we identify the lung domain at the inspiration phase as the *current configuration* and define the deformation mapping $\varphi : B \longrightarrow \mathbb{R}^3$ as the field that transforms all points from the reference to the current

configuration. We further define the *deformation gradient* tensor as

$$\boldsymbol{F} := \nabla_{\boldsymbol{X}} \boldsymbol{\varphi}, \tag{2.1}$$

where $\nabla_{\boldsymbol{X}}$ represents the gradient operator with respect to the reference coordinates $\boldsymbol{X}$. Given a unitary vector in the reference configuration $\boldsymbol{M} \in \mathbb{R}^3$, we compute the *stretch ratio* along such direction as

$$\lambda(\boldsymbol{M}) := \sqrt{\|\boldsymbol{F}\boldsymbol{M}\|^2}. \tag{2.2}$$

The stretch ratio delivers the change of length of a segment originally in the direction $\boldsymbol{M}$ normalized by its length in the reference configuration. The volumetric deformation or volume change is given by the determinant of the deformation gradient tensor, also known as the Jacobian,

$$J := \det \boldsymbol{F}. \tag{2.3}$$
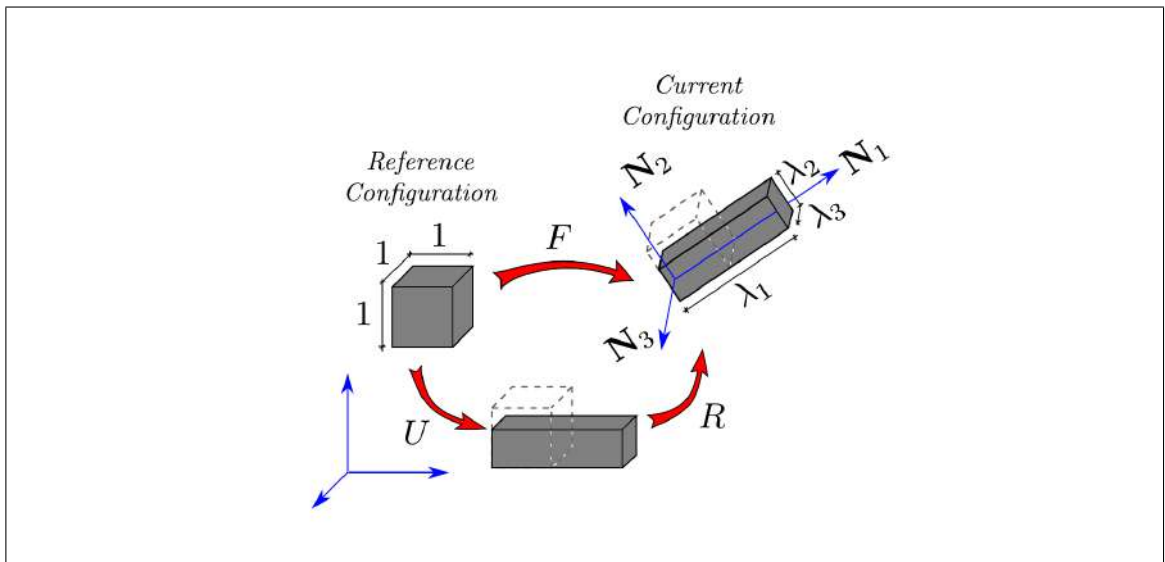
Figure 2.1. Sketch of the polar and spectral decomposition of the deformation gradient tensor

It follows from the polar decomposition theorem (Ogden, 1984) that the deformation gradient can be uniquely decomposed as

$$\boldsymbol{F} = \boldsymbol{R}\boldsymbol{U}, \tag{2.4}$$

where $\boldsymbol{R} \in SO(3)$ is a rotation tensor and $\boldsymbol{U}$ is a symmetric positive-definite tensor, also known as the right stretch tensor. Further, the spectral decomposition theorem allows for the expansion

$$\boldsymbol{U} = \sum_{\alpha=1}^{3} \lambda_\alpha \boldsymbol{N}_\alpha \otimes \boldsymbol{N}_\alpha, \tag{2.5}$$

where $\{\lambda_1, \lambda_2, \lambda_3\}$ with $\lambda_1 \geq \lambda_2 \geq \lambda_3 > 0$ are the principal stretches, and $\{\boldsymbol{N}_1, \boldsymbol{N}_2, \boldsymbol{N}_3\}$ are the material principal directions, depicted in Figure 2.1. To study the anisotropy of deformation, we consider the anisotropic deformation index (ADI) and the slab-rod index (SRI) defined as (Amelon et al., 2011; Jahani et al., 2015)

$$\text{ADI} := \sqrt{\left(\frac{\lambda_1 - \lambda_2}{\lambda_2}\right)^2 + \left(\frac{\lambda_2 - \lambda_3}{\lambda_3}\right)^2} \tag{2.6}$$

$$\text{SRI} := \frac{\tan^{-1}\left(\frac{\lambda_3(\lambda_1 - \lambda_2)}{\lambda_2(\lambda_2 - \lambda_3)}\right)}{\frac{\pi}{2}} \tag{2.7}$$

An ADI value of 0 implies an isotropic deformation, i.e., $\lambda_1 = \lambda_2 = \lambda_3$, while departure from zero indicates that deformation is anisotropic. The SRI ranges from 0 to 1, with values closer to 0 indicating a slab-like deformation, and values closer to 1 indicate a rod-like deformation, given that ADI is not close to zero.

Assuming a hyperelastic constitutive behavior for the parenchymal tissue, it follows that the biomechanical response can be modeled by a deformation energy density $W(\boldsymbol{F})$. From isotropy and objectivity considerations and the isotropic function representation theorem (Truesdell & Noll, 1965) it follows that

$$W(\boldsymbol{F}) = \tilde{W}(I_1, I_2, I_3) \tag{2.8}$$

that is, the deformation energy density will only depend on the invariants of the right stretch tensor $\boldsymbol{U}$, which can be defined as

$$I_1 := \frac{1}{3} \operatorname{trace}(\boldsymbol{U}) \equiv \frac{1}{3}(\lambda_1 + \lambda_2 + \lambda_3), \tag{2.9}$$

$$I_2 := \frac{1}{6} \left((\operatorname{trace}(\boldsymbol{U}))^2 - \operatorname{trace}(\boldsymbol{U}^2) \right) \equiv \frac{1}{3}(\lambda_1\lambda_2 + \lambda_2\lambda_3 + \lambda_3\lambda_1), \tag{2.10}$$

$$I_3 := \det(\boldsymbol{U}) \equiv \lambda_1\lambda_2\lambda_3. \tag{2.11}$$

We note here that our definition of invariants differs by a constant of $\frac{1}{3}$ from standard definitions of the first and second invariants for normalization purposes, i.e., all invariants will take a unitary value when no deformation is applied ($\boldsymbol{F} = \boldsymbol{I}$). From a kinematic perspective, we note from Figure 2.1 that I_1 corresponds to a length deformation measured in terms of the Manhattan distance, i.e., the ratio of the sum of edge lengths in the deformed configuration over the sum of edge lengths in the undeformed configuration. Further, I_2 corresponds to a surface deformation, i.e., the ratio of the surface area in the deformed configuration over the surface area of the undeformed unitary cube. Finally, we note that $I_3 \equiv J$, i.e., the third invariant is equal to the volumetric deformation, or Jacobian.

To construct 3D maps of the deformation gradient tensor and its associated deformation measures, we perform biomechanical analysis on the acquired data sets using the finite-element (FE)-based method proposed in (Hurtado, Villarroel, et al., 2016). FE methods have been widely employed in the field of biomechanics, ranging from modeling the mechanical behavior of complex alveolar structures (Hobrack, Haberthür, Stampanoni, Schittny, & Wall, 2011) and respiratory airways (Eskandari, Kuschner, & Kuhl, 2015) up to understanding the physiological behavior of tissue and organs in the cardiovascular system (Hurtado & Henao, 2014; Hurtado, Castro, & Gizzi, 2016), mainly due to its capability to accurately represent intricate geometries spanning several scales in the human body. Further, the quantification of biomechanical properties using FE analysis has proven to be robust to the inherent image noise in many applications (Sotelo et al., 2015, 2016). For the particular case of lung tissue, FE-based biomechanical analysis delivers

deformation gradient maps that are more accurate than those obtained by direct differentiation of the transformation mapping resulting from image registration, as demonstrated in (Hurtado, Villarroel, et al., 2016).

In order to perform the biomechanical analysis, CT datasets are first registered using the free-form deformation non-rigid registration Nifty-Reg package (Modat, Ridgway, et al., 2010). The Nifty-Reg package finds an optimal transformation between two CT images by minimizing a cost function that includes different voxel-based similarity measure, as well as an elastic regularization to ensure smoothness of the optimal transformation. The transformation model is based on cubic B-spline basis functions that deliver a C^2 continuous image transformation. Convergence issues may arise during the optimization as the deformation levels experienced by the lung parenchyma can be large. To improve the convergence and accuracy of the registration, we adopted the recommendations of (Modat, Mcclelland, & Ourselin, 2010) on control-point spacing, registration parameters and solution strategy (further details in A.1). During the registration process (non-rigid model), two penalty terms were used. The first, known as "bending energy", favors a smooth mapping between both images, and the second, based on the Jacobian, ensures a one-to-one mapping to avoid folding problems. Although these parameters were adjusted to generate adequate results, it is worth mentioning that the Jacobian constraint could cause a certain degree of bias when quantifying regional volumetric strain. At the end of the registration process, all results were verified to have converged correctly. Clinical experts also performed a visual inspection to confirm that the results were reasonable.

To construct the FE discretization of the lung domain, we use the active contour segmentation method implemented in ITK-Snap (Yushkevich et al., 2006) (www.itksnap.org). ITK-Snap implements an active contour algorithm using a geodesic flow formulation, a particular case of an "*energy snakes*" model to detect edges that is based on finding a geodesic curve in a Riemannian space derived from the content of an image (Caselles, Kimmel, & Sapiro, 1997). Regarding the segmentation procedure, first, the lung under

study is isolated by defining a region of interest, and a threshold filter is used to differentiate the lung from the surrounding tissue. Then, seeds are manually planted inside the lung domain, and the active contour tool is executed. The resulting segmented image is visually checked, and manual segmentation is performed in regions where semi-automated methods could not correctly resolve the lung anatomy. Final image segmentation is always checked by clinical experts. Tetrahedral FE meshes are then constructed from the segmented lung images using automated mesh generation libraries (*Computational geometry algorithms library*, 2016) (http://www.cgal.org). In particular, 3D triangulation functions were used to mesh the surface of the segmented image and then tetrahedralization functions to generate the full mesh. The parameter that controls the tetrahedron size in the mesh is called "*cell_size*" and was set to 8 for all cases. This process resulted in unstructured meshes with a tetrahedron mean size of $29.6[\text{mm}^3]$ with a standard deviation of $20.1[\text{mm}^3]$. To ensure a good mesh quality, the minimum dihedral angle for each tetrahedral element is tracked during the mesh generation. A variational strain recovery method is then employed to obtain a continuous FE approximation to the deformation gradient tensor field (Hurtado, Villarroel, et al., 2016), from which regional volumetric strain and principal stretch ratios are computed.

Histograms of all three deformation invariants are constructed from the 3D maps of regional deformation. To this end, we consider the value of the field of interest at the barycenter for each element of the mesh and its associated element volume. Statistical descriptors typically employed in nonparametric analysis are computed for all the histograms generated. In particular, we compute kurtosis to understand how *localized* around the mean value are the distributions. Skewness is also computed for all histograms, in order to assess the asymmetry of the resulting distributions. After inspecting the resulting histograms and associated statistical descriptors, a parametric distribution function is sought in order to explain the frequency distribution of the deformation metric under analysis.

To compare the spatial patterns of regional deformation along the dorsal-ventral direction between all subjects in an average sense, we divide each lung domain in ten regions

of interest (ROI). A ROI is defined by the intersection of one rectangular cuboid with the lung domain, where cuboids are contiguously stacked along the dorsal-ventral direction and have the same height, see inset in Figure 2.7(**a**). For each ROI, we compute the weighed mean value of the deformation metric under study using all the nodes that are located within a particular ROI and their corresponding adjacent element volumes.

All models, such as FE discretization (meshing), biomechanical analysis, image processing, and statistics, were coded in Python using a processor Intel Core i7-4710MQ CPU @ 2.50GHz × 8.

2.3. Results

The results obtained from the biomechanical analysis were all volumetric in nature, as shown in Figure 2.2; however, for a matter of practicality and clinical reasoning, the results shown in the following figures consider a single plane (i.e., sagittal). The coronal and axial planes did not show relevant deformation trends (results not shown). Moreover, to avoid the bias that can occur when displaying results on color maps that do not have a linear scale, the results shown in this chapter differ from the images in the published article. In particular, the biomechanical results are presented in a gray-scale palette instead of the original rainbow-type color-map. However, the Supplementary Material in the First Appendix includes the original version of the figures.
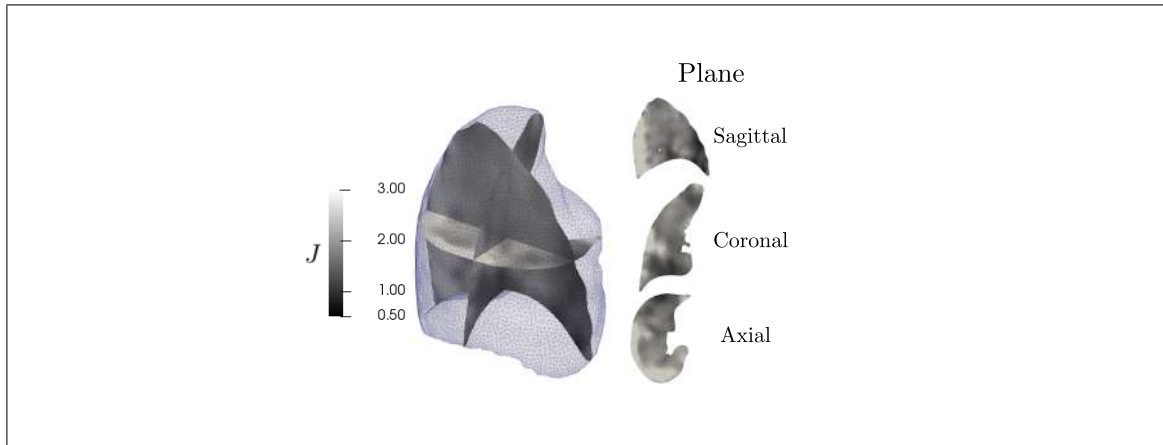
Figure 2.2. Schematic of regional volumetric deformation of the right lung for an arbitrary subject showing the different anatomical planes.

Sagittal planes of I_1 , I_2 and J for the right lung of two representative subjects are shown in Figure 2.3. A highly heterogeneous spatial distribution is observed for all deformation metrics and all subjects under analysis (see Supplementary Material 1 in Appendix A.2). In particular, subject 05 shows markedly high levels of Jacobian ($J > 3$) in a significant portion of the section, located predominantly in the dorsal region but without a clear pattern. For the planes shown, subject 05 displays $J > 1$ everywhere, which are indicative of a predominant parenchymal expansion. In contrast, Subject 02 displays small regions of volumetric compression ($J < 1$) associated with alveolar compression. A similar trend is observed for the case of surface deformation I_2 , where higher values are located close to the dorsal region in both lungs shown, with Subject 05 always showing $I_2 > 1$ everywhere, and greater values of I_2 than Subject 02 for a similar location in space.
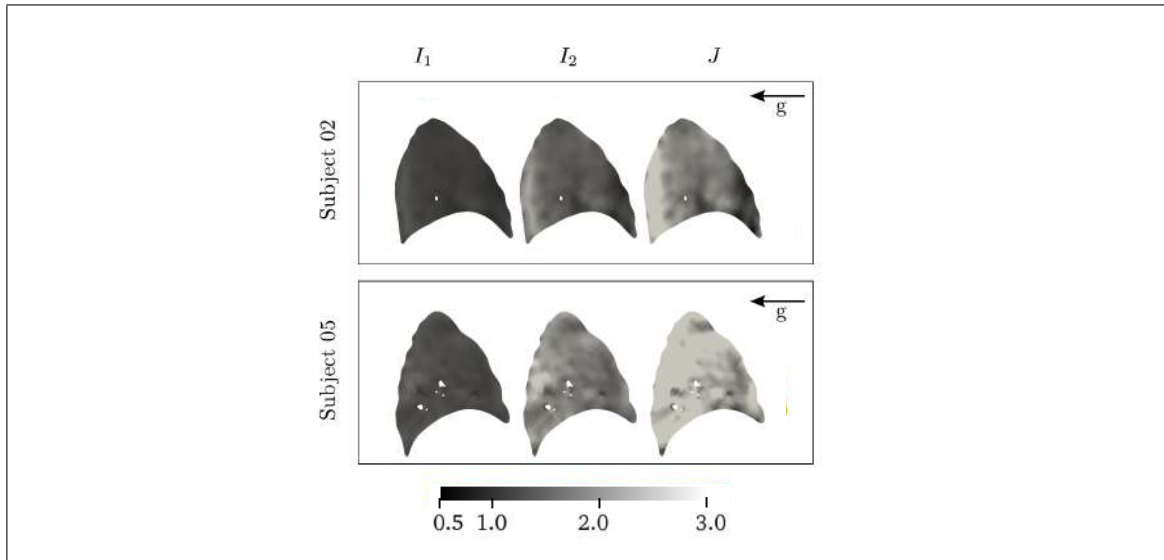
Figure 2.3. Deformation invariant maps for the right lung of two representative subjects. *Black arrows* indicate the direction of gravity

The ADI and SRI index maps for the same representative lungs are shown in Figure 2.4. The ADI index is significantly greater than zero in a considerable region of the slice shown, with no clear spatial trend. The SRI randomly oscillates between 0 and 1 throughout the lung, a trend also observed in all other subjects studied (see Supplementary Material 1 in Appendix A.2).
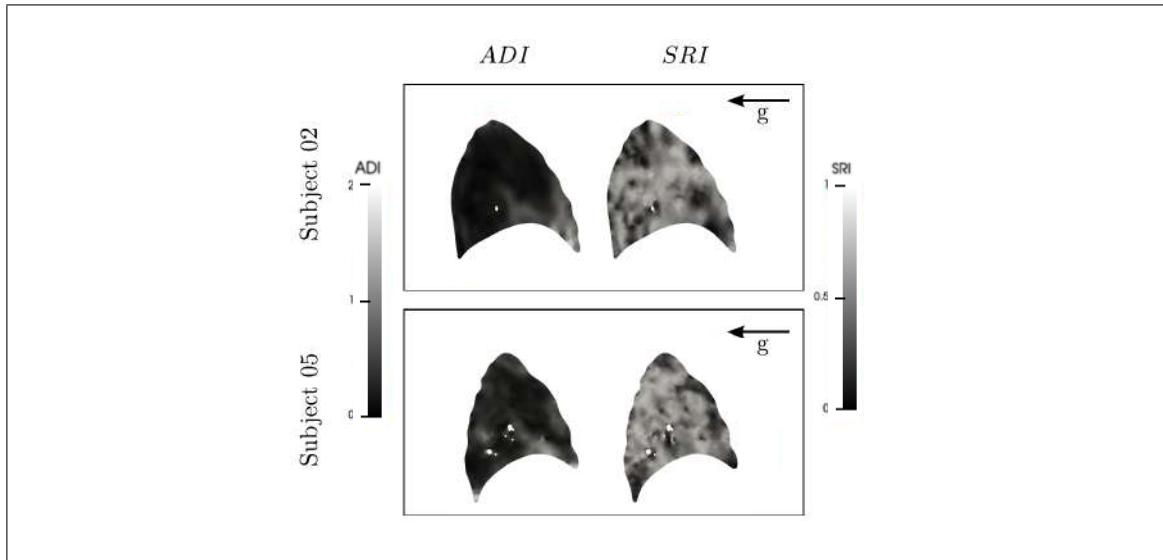
Figure 2.4. ADI and SRI maps for the right lung of two representative subjects. *Black arrows* indicate the direction of gravity

Table 2.2 reports the sample mean, standard deviation, kurtosis and skewness of the Jacobian field for the left and right lungs of all subjects. The mean Jacobian ranges from 1.45 to 3.41 for the left lung, and from 1.41 to 3.12 for the right lung, which confirms a large intersubject variability. The standard deviation also shows intersubject variability, but with less spread than the sample mean. In contrast with intersubject dispersion, the mean and standard deviation values for the left and right lung of each subject were very similar. A marked positive skewness is found in all cases, with the exception of the left lung of S06, for which skewness is roughy zero. Deformation invariants I_1 and I_2 display also display marked positive skewness, with a few exceptions where skewness is roughly zero (See Tables A.4 and A.5 of Supplementary Material 2 for the case of I_1 and I_2, respectively in Appendix A.3).

Table 2.2. Statistical measures for the left lung (LL) and right lung (RL) Jacobian distributions

Subject	Mean		Std		Kurt.		Skew.	
	LL	RL	LL	RL	LL	RL	LL	RL
S01	1.87	1.80	0.62	0.55	2.36	6.07	1.22	1.58
S02	2.15	2.19	0.50	0.60	1.78	1.78	0.92	0.77
S03	1.96	1.97	0.56	0.68	3.43	1.85	1.06	1.12
S04	1.87	1.74	0.40	0.33	2.13	2.03	0.75	0.57
S05	3.41	3.01	0.86	0.79	1.07	0.98	0.53	0.44
S06	3.22	3.13	0.62	0.66	0.84	1.06	-0.02	0.32
S07	1.96	1.83	0.48	0.43	2.58	1.53	0.94	0.18
S08	2.89	2.82	1.02	0.87	0.82	0.28	0.40	0.27
S09	1.45	1.41	0.28	0.31	2.49	4.15	0.64	1.00
S10	2.48	2.37	0.63	0.57	1.08	1.04	0.54	0.17
S11	2.92	2.75	1.13	1.23	3.50	4.71	1.49	1.62

To validate our method, we computed the relative error between the average Jacobian value obtained from the FE biomechanical analysis and the FRC-TLC volumetric deformation for each lung, defined as the ratio of the inspired volume over the expired volume estimated directly from CT lung images, see Table 2.3. We note that the average error values are 2.5% and 2.3% for the left and right lung, respectively, with a maximum relative error of 4% for subject S08.

Table 2.3. Method validation: comparison between average Jacobian and volumetric deformation obtained from image segmentation

Subject	Ins.-Exp. ratio		Error (%)	
	LL	RL	LL	RL
S01	1.94	1.88	3.9	3.9
S02	2.17	2.21	0.8	0.9
S03	2.03	2.00	3.1	1.5
S04	1.93	1.79	3.2	3.1
S05	3.54	3.21	3.6	3.3
S06	3.29	3.18	1.9	1.8
S07	2.02	1.91	2.2	1.9
S08	3.02	2.92	4.0	3.5
S09	1.47	1.44	1.5	1.6
S10	2.55	2.44	3.0	2.8
S11	2.94	2.77	0.8	0.8
		Average	2.5	2.3

Based on the histograms obtained from the biomechanical analysis for the deformation invariants, which were unimodal and positively skewed, we propose a log-normal distribution to explain them. The associated probability distribution functions take the form

$$\mathrm{pdf}(x) = \frac{1}{x\sigma\sqrt{2\pi}}\, e^{-\frac{(\ln x - \mu)^2}{2\sigma^2}}, \tag{2.12}$$

where μ and σ are the location and scale parameters, respectively. The maximum-likelihood estimators for these parameters read

$$\hat{\mu} = \frac{\sum_{k=1}^{n} \ln x_k}{n}, \tag{2.13}$$

$$\hat{\sigma}^2 = \frac{\sum_{k=1}^{n} (\ln x_k - \hat{\mu})^2}{n}. \tag{2.14}$$

Table 2.4. Log-normal fit: location and scale parameters, and fit error for J

Subject	$\hat{\mu}$		$\hat{\sigma}$		Error (%)	
	LL	RL	LL	RL	LL	RL
S01	0.574	0.548	0.318	0.283	9.5	11.1
S02	0.739	0.746	0.228	0.279	10.7	20.0
S03	0.636	0.622	0.280	0.333	12.5	12.5
S04	0.604	0.533	0.213	0.190	13.5	13.1
S05	1.196	1.097	0.259	0.268	14.7	20.0
S06	1.150	1.117	0.207	0.217	20.3	18.7
S07	0.657	0.584	0.230	0.324	17.8	31.6
S08	0.992	0.984	0.394	0.342	21.9	16.7
S09	0.353	0.322	0.198	0.219	13.8	19.0
S10	0.874	0.832	0.261	0.262	9.8	23.7
S11	1.004	0.919	0.366	0.437	17.9	22.6
				Average	14.8	18.9

Table 2.4 shows the values for these estimators for the Jacobian distribution of all subjects analyzed. The relative error between the histograms and the frequency distribution functions was computed as

$$\text{error} = \frac{\|\text{pdf} - \text{hist}\|_{L^2(I)}}{\|\text{pdf}\|_{L^2(I)}}, \tag{2.15}$$

where I is the support of the frequency distribution function, pdf $: I \longrightarrow \mathbb{R}$ is the frequency distribution function, hist $: I \longrightarrow \mathbb{R}$ is the histogram, and the L^2 norm is defined by

$$\|f\|_{L^2(I)} := \left(\int_I f^2(x)\,dx \right)^{\frac{1}{2}} \tag{2.16}$$

Table 2.4 reports the fit error for the Jacobian distributions. We observe that the fit error ranges between 9.5% (left lung of subject S01) and 31.6% (right lung of subject S07), with average values of 14.8% and 18.9% for the left and right lungs, respectively.
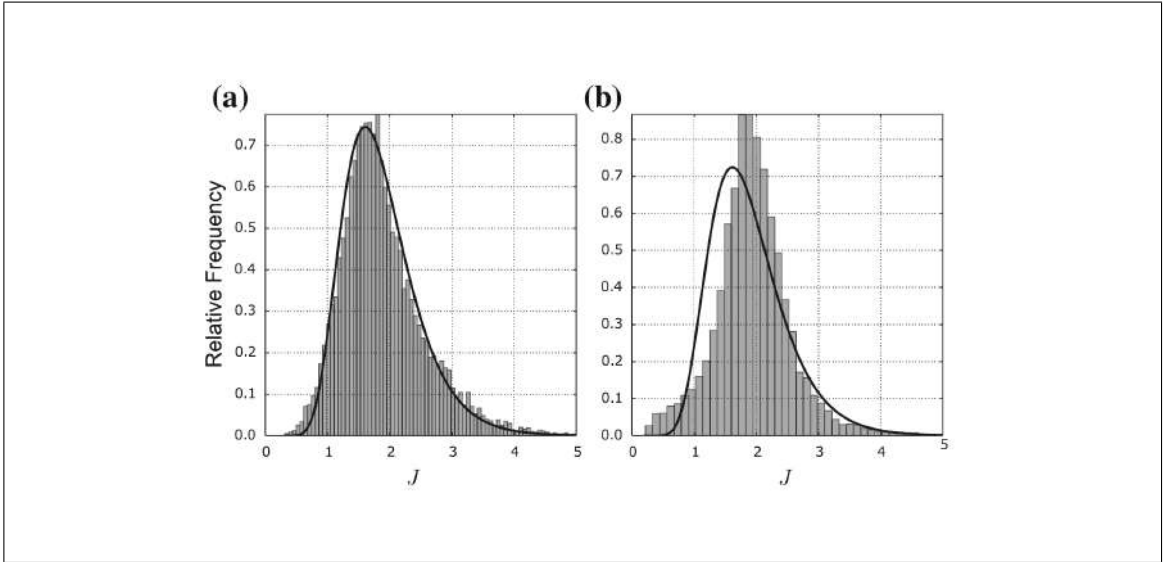
Figure 2.5. Histograms for the Jacobian, and log-normal fit: **(a)** best fit, left lung, S01, **(b)** worst fit, right lung, S07

The histograms and log-normal fit for the best and worst cases are shown in Figure 2.5. Average fit errors for the case of I_1 are 14.4% (LL) and 14.9% (RL), while for I_2 average fit errors are 14.7% (LL) and 16.2% (RL), see Tables A.6 and A.7 of Supplementary Material 2 in Appendix A.3.

Based on the overall good fit of the log-normal distribution to the frequency distributions of the deformation invariants, we propose normalizing the deformation invariant fields obtained for each subject using the score of the log-normal distribution, i.e.,

$$\hat{\Box}(\boldsymbol{X}) := \frac{\log(\Box(\boldsymbol{X})) - \hat{\mu}}{\hat{\sigma}}, \tag{2.17}$$

where $\Box(\boldsymbol{X})$ represents the deformation invariant field, and $\hat{\mu}$ and $\hat{\sigma}$ are the location and scale parameters, respectively, for the subject under analysis.
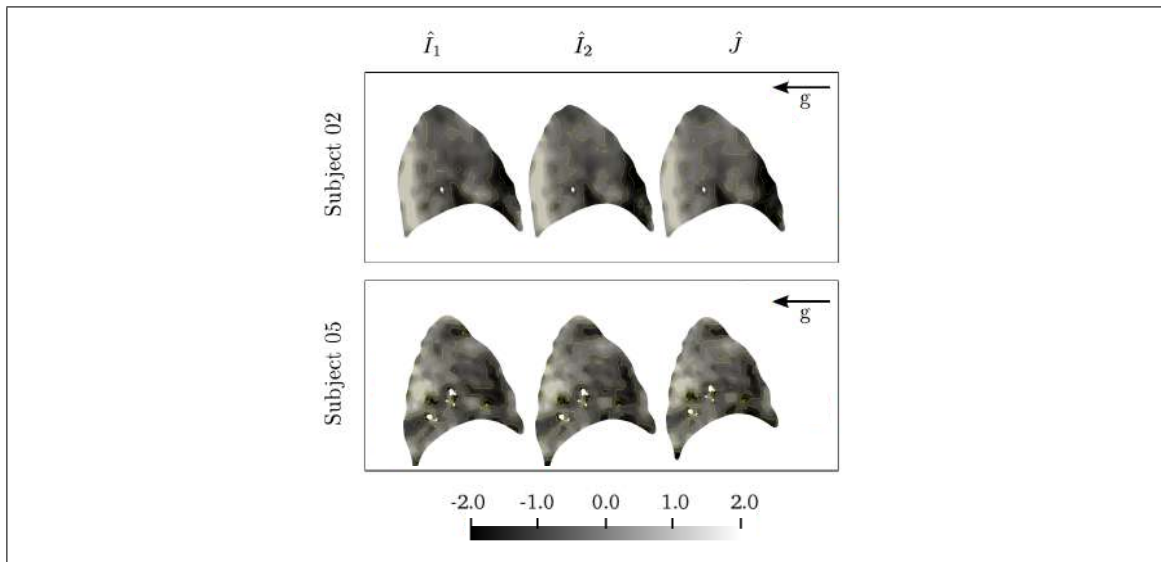
Figure 2.6. Normalized deformation invariant maps for the right lung of two representative subjects. Black arrows indicate the direction of gravity. Yellow lines indicate contour lines at values $-2, -1, 0, 1, 2$.

Figure 2.6 shows the maps of $\hat{I}_1$, $\hat{I}_2$ and $\hat{J}$ for the right lung of the same representative subjects analyzed in Figure 2.3. Similar to the case of non-scaled maps, a high spatial variation of all three normalized invariants is clearly observed for all subjects (see Supplementary Material 3 in Appendix A.4). However, in the normalized form, it is now possible to recognize common spatial patterns of deformation shared by subjects. More precisely, a vertically elongated region of high values for all three deformation invariants is consistently found in the dorsal regions of both subject lungs. Zones of low invariant values are found in the ventral region. These observations suggest an overall spatial gradient of normalized deformation invariants the dorsal-ventral direction, which coincides with the gravitational direction. Further, we note that in normalized form, the three invariant fields characterizing normalized length, surface and volume deformation take very similar values in space for the same subject.
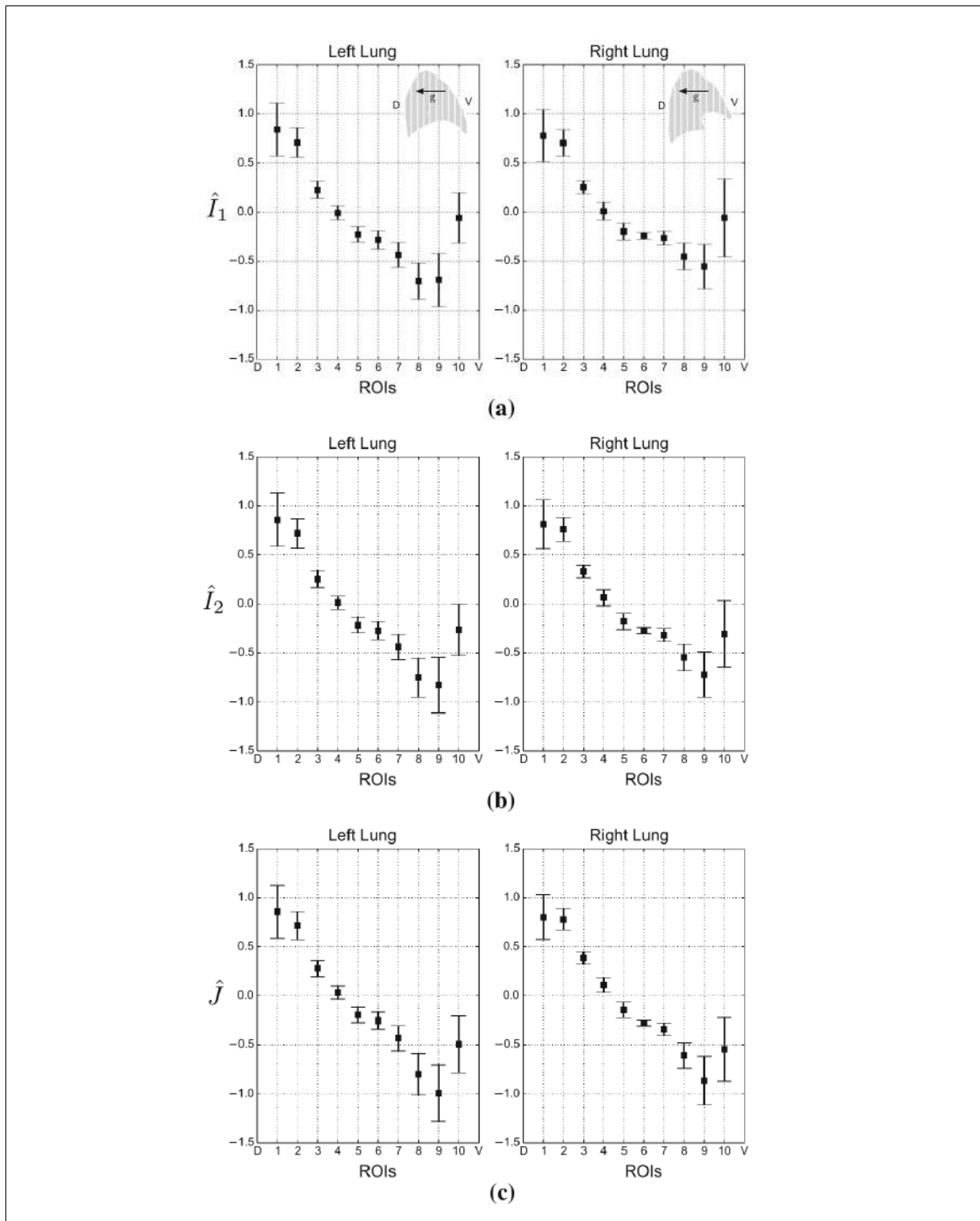
Figure 2.7. Dorsal (D) - ventral (V) distributions of ROI normalized invariants: (a) $\hat{I}_1$, (b) $\hat{I}_2$ and (c) J. *Error bars* show 95% confidence interval

For clarity, the sagittal slices of the two representative subjects (Figures 2.3 and 2.6) and the slices shown in the Supplementary Material A.2 and A.4 often present holes. During the semi-automatic segmentation process, these holes correspond to areas that are not considered part of the lung tissue (i.e., large blood vessels), mainly due to the threshold established in terms of the HU (Hounsfield Units) scale within the CT image. Expert physicians supervised this earlier definition regarding the image intensity threshold.

Figure 2.7 shows the distribution of ROI-averaged normalized deformation invariants along the dorsal-ventral direction for the left and right lungs of all subjects. For all three normalized deformation invariants, higher values are consistently found in the dorsal ROI, whereas lower values are observed in the ventral ROI, both in left and right lungs of all patients. While individual ROI distributions were not all strictly monotonically decreasing (not shown), we do confirm an overall gradient of normalized invariants which decreases in the dorsal-ventral direction. Higher intersubject dispersion is found at the ventral and dorsal ROIs, while interior ROIs present low dispersion around the mean value.

To assess the potential impact of lobar sliding on our results, we performed lobe-by-lobe analysis for the lungs of subject S02. To this end, the lobes of both lungs were segmented in FRC and TLC lung images, to then perform image registration and biomechanical analysis on individual lobes as described in the Methods section.

Figure 2.8$(\mathbf{a})$ shows a slice of the $\hat{I}_1$ map, where we observe, in broad terms, a similar spatial pattern as found in the whole-lung analysis, i.e., zones of high invariant values close to the dorsal region, and zones of low invariant values close to the ventral region, confirming a spatial gradient in the gravitational direction. Figure 2.8$(\mathbf{b})$ shows the comparison between the histograms and log-normal fits for the I_1 distribution of the right lung for the lobe-by-lobe analysis and the whole-lung analysis. Minor differences are found between the approaches when comparing their distributions. However, small differences can be observed near the borders of the lobes when comparing Figure 2.8$(\mathbf{a})$ and 2.6. Similar results were obtained for I_2 and J (not shown).
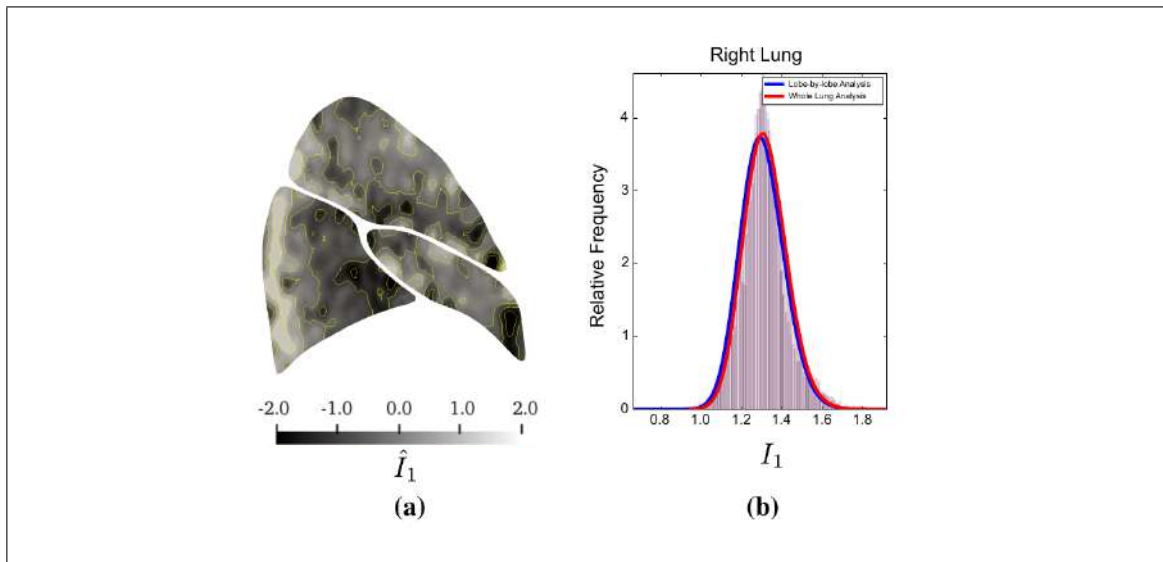
Figure 2.8. Lobe-by-lobe analysis for Subject S02: **(a)** $\hat{I}_1$ for right lung, **(b)** Comparison of histograms and log-normal fit between lobe-by-lobe and whole-lung analysis for I_1. Yellow lines in **(a)** indicate contour lines at $\hat{I}_1 : -2, -1, 0, 1, 2$.

2.4. Discussion

In this work, we systematically performed image-based biomechanical analyses to study the regional deformation in healthy human lungs from CT images, in the search of common spatial patterns of deformation and other statistical information that could potentially characterize healthy lungs in a general manner. At a global scale, our results show that relative volume changes of the left and right lungs are very similar for the subjects under study. This conclusion is reinforced by the results for global volumetric deformation computed directly from image analysis, which also shows small differences between left and right lungs (Table 2.3). Such observation correlates well with the high similarity of ventilation levels between left and right lung found in previous studies using Xenon tests on healthy human subjects (Milic-Emili, Henderson, Dolovich, Trop, & Kaneko, 1966). At a regional level, our study confirms that local volumetric deformation in the lung parenchyma displays marked spatial variations in healthy human subjects spontaneously

breathing in supine position. Spatial variations of regional volumetric deformation have been reported in the literature from studies based on image registration techniques for healthy ovine (Reinhardt et al., 2008), canine (Kaczka, Cao, Christensen, Bates, & Simon, 2011) and human lungs (Amelon et al., 2011; Cao et al., 2012; Jahani et al., 2014; Choi et al., 2013). Similar to the findings reported these studies, our ROI analysis (see Figure 2.7) confirms a marked gradient in regional volumetric deformation along the ventral-dorsal direction, which coincides with the direction of gravity. These results are consistent with the distribution of ventilation in human lungs in supine position, where ventilation in the dorsal regions of the lung is higher than in the ventral regions due to gravity (West, 2012). A novel conclusion of our work is that not only regional volumetric deformation, but also length and surface deformation displays a strong gradient in the gravity direction.

Another key contribution of this work is the quantitative analysis of regional deformation in terms of frequency distributions. In particular, our findings strongly suggest that length, surface and volumetric regional deformation in normal human lungs in supine position follow a log-normal distribution. In turn, this finding motivates the introduction of a simple subject-specific normalization of the regional measures of deformation that allows for a better intersubject spatial comparison, given by Equation 2.17. When maps and distributions are studied without normalization, we observe large variations between subjects that make the direct comparison difficult. We attribute these large variations both to body anatomical differences, as reflected by individual BMI and TLC (Table 2.1), and to the natural variability in the respiratory effort of each subject to reach and maintain TLC during CT acquisition. When normalization is applied, common spatial patterns of regional deformation are readily observed for all three deformation invariants analyzed. In effect, the distribution of normalized Jacobian shown in sagittal planes displays consistent spatial patterns of deformation across all subjects analyzed, with areas of high Jacobian values, above the location parameter (or logarithmic average), consistently found in the dorsal region, see Figure 2.6. Similarly, lower values of volumetric deformation, below the location parameter, are observed in the ventral region in all subjects studied. Interestingly,

spatial fields of length and surface deformation metrics in normalized form have very similar spatial pattern and values to the case of normalized Jacobian (Figure 2.6), confirming a strong correlation with the gravity direction. It is important to remark that normalization of deformation maps removes global information that may be used as a descriptor of lung disease. For example, in the case of air trapping, average volumetric deformation varies between normal and asthmatic lungs (Choi et al., 2013). In asthmatic patients, decreased Jacobian values have been associated with increased air trapping (Choi, Hoffman, Wenzel, Castro, & Lin, 2014) and segmental airway narrowing (Choi et al., 2015). Such features will not be displayed by normalized maps, as we subtract the logarithmic mean value of deformation invariants. Thus, we expect normalized maps to contribute with additional regional information to previously proposed deformation measures, e.g., by identifying local alterations in the spatial patterns of regional deformation.

Throughout this work, we have advocated for the characterization of not only regional volumetric deformation and anisotropy, but also of regional surface and length deformation through the first and second invariants of the right stretch tensor. We note that ADI can be high in many regions of the lung, confirming that regional deformation is anisotropic and cannot be expressed solely in terms of volumetric deformation. Due to the isotropy and objectivity considerations, and the isotropic function representation theorem (Truesdell & Noll, 1965), length and surface deformation, measured in terms of the first and second invariant of the right stretch tensor take special relevance in the constitutive modeling of lung parenchyma. In the case where regional deformation is isotropic, the first and second deformation invariants can be expressed in terms of the Jacobian, i.e., all three invariants would be dependent, and constitutive relations may be expressed only in terms of volumetric deformation. In this work we have confirmed that regional deformation in the in vivo lung parenchyma can be highly anisotropic with random distribution in space (Figure 2.4), a behavior also found in previous in vivo studies of human lungs (Amelon et al., 2011; Choi et al., 2013; Jahani et al., 2014). Thus, one cannot assume that only volumetric deformation will govern the mechanics of parenchyma and should

also consider the role of the first and second deformation invariants. In effect, experimental evidence has shown, through mechanical testing, that the constitutive response of murcine lung parenchyma is highly dependent not only on the Jacobian but also on the first invariant of the square of the right stretch tensor (Rausch et al., 2011), confirming the importance of studying regional length deformation in the lung.

The present study suffers from certain limitations. First, our study considers a small population and does not differentiate gender, age, and physical activity, among many other possible classifications, thus limiting our conclusions about distribution or spatial patterns in general terms. Future contributions should consider larger and more specific populations, in order to be able to characterize deformation metric ranges more accurately, and before attempting to use them as a descriptor of lung disease. Second, small regions of highly localized regional deformation were found close to the lung fissures in some subjects. As recently reported (Amelon et al., 2014), fissure sliding can induce artificially high values of shear strain, which may have a considerable impact in the accuracy of the estimation of maximum and minimum stretch ratios. This effect is directly related to the inherent C^2-continuity imposed by the B-spline interpolation of the deformation mapping field, which is not capable of accommodating sliding or material interface strain jumps, as explained in (Hurtado, Villarroel, et al., 2016). Fissure sliding effect may have an impact in the determination of the principal stretches, potentially raising the deformation invariants to unrealistic levels in regions close to a fissure. However, using lobe-by-lobe analysis we have shown for one subject that the impact of eliminating the lobar fissure region from the registration and biomechanical analysis does not importantly alter the invariant maps, neither the frequency distribution. We attribute this small effect to the fact that regions with high values of regional deformation due to lobar sliding are very localized and within small volumes of tissue. Slight differences of regional deformation near the boundaries of the lobes when comparing the lobe-by-lobe analysis and whole-lung analysis are not entirely clear and may be due to boundary effects. Future contributions should focus in deformable image registration methods that are capable of distinguishing shear strains due to sliding from actual shearing deformation. While sliding has been preliminary addressed

in some recent works (Yin et al., 2010; Pace et al., 2013), a biomechanical analysis that can effectively eliminate spurious shear distortion in the estimation of regional deformation remains an open avenue of research. Third, a limitation related to the method of biomechanical analysis is the potentially poor estimation of strain in regions adjacent to anatomical boundaries, such as the lung surface, small airways and small vessels. For the case of airways and vessels, since the FE mesh is constructed from the segmented lung image, small airways and vessels that are not segmented out will be considered as lung tissue by the FE method, and consequently continuous strain maps will be displayed in those areas. For the case of the lung surface, errors inherent to the semiautomatic segmentation process may result in a FE surface representation that can leave some portions of the lung surface outside the FE mesh, thus inducing to errors by not considering the deformation of the tissue left out the segmentation. We believe this effect may also be responsible for the large deviations from the mean found in the ROI analysis (Figure 2.7) in those regions close to the dorsal and ventral surfaces. This same effect may be responsible for the differences that arise when comparing regional deformation differences between the lobe-by-lobe and whole-lung analyses (see Figure A.1 in the Supplementary Material A.5). Future contributions should focus on developing meshing methods that can effectively capture the lung surface, small airways and vessels, in order to improve the estimation of regional deformation in the surrounding areas. Fourth, the field normalization scheme is limited. Due to the shape of the invariants' frequency distributions (i.e., unimodal and positively skewed), this work proposed a logarithmic normalization and was further used to normalize the 3D maps of regional deformation. However, other normalization alternatives such as Rayleigh or Gamma distributions could also be used for the same purposes. Future contributions should focus on developing new forms of subject-specific normalization or even population-specific normalization. In this regard, a thorough sensitivity analysis between different normalization models could provide a better solution when comparing between subjects.

3. INELASTIC DEFORMABLE IMAGE REGISTRATION

Abstract Deformable image registration (DIR) is an image-analysis method with a broad range of applications in biomedical sciences. Current applications of DIR on computed-tomography (CT) images of the lung and other organs under deformation suffer from large errors and artifacts due to the inability of standard DIR methods to capture sliding between interfaces, as standard transformation models cannot adequately handle discontinuities. In this work, we aim at creating a novel inelastic deformable image registration (i-DIR) method that automatically detects sliding surfaces and that is capable of handling sliding discontinuous motion. Our method relies in the introduction of an inelastic regularization term in the DIR formulation, where sliding is characterized as an inelastic shear strain. We validate the i-DIR by studying synthetic image datasets with strong sliding motion, and compare its results against two other elastic DIR formulations using landmark analysis. Further, we demonstrate the applicability of the i-DIR method to medical CT images by registering lung CT images. Our results show that the i-DIR method delivers accurate estimates of local lung strain that are similar to fields reported in the literature, and that do not exhibit spurious oscillatory patterns typically observed in elastic DIR methods. We conclude that the i-DIR method automatically locates regions of sliding that arise in the dorsal pleural cavity, delivering significantly smaller errors than traditional elastic DIR methods.

3.1. Introduction

Deformable image registration (DIR) is an image-analysis technique used to determine the optimal transformation that establishes the spatial correspondence of a point between two images. When constructing a DIR method, three key elements need to be defined: i) the transformation model, ii) the regularizer, and iii) the similarity measure (Sotiras, Davatzikos, & Paragios, 2013b). These elements allow for the classification of DIR methods, and the reader is referred to (Modersitzki, 2003) for a complete review. In particular, in this work we are concerned with the ability of the method to capture large

displacements in the optimal transformation between medical images. From this perspective, transformation models can be divided into continuous-displacement transformations (Rueckert et al., 1999), which are suitable for small-deformation problems, and incremental diffeomorphic transformations based on the integration of flow equations (Ashburner, 2007; Christensen, Rabbitt, & Miller, 1996), which can capture large deformations in DIR problems. While diffeomorphic methods have proven advantageous in capturing the large-displacement kinematics in DIR, continuous displacement models have been preferred in the field of medical imaging, as they provide a simple and efficient computational framework to DIR (Reinhardt et al., 2008).

DIR has essential applications in radiology, such as the fusion of an anatomical image with a functional image (Oliveira & Tavares, 2014), image-guided radiotherapy (Foskey et al., 2005), and in treatment and surgery planning (Gering et al., 1999). DIR has proven fundamental in the study of the deformation mechanisms that take place at a regional level in human lungs, where the primary inputs for determining regional strain are deformation measures based on the Jacobian matrix of the optimal transformation resulting from DIR of lung computed-tomography (CT) images (Reinhardt et al., 2008; Amelon et al., 2011). DIR-based biomechanical analysis has revealed significant spatial differences in the magnitude, anisotropy, and heterogeneity of regional deformation in the lung of normal human subjects (Amelon et al., 2011; Hurtado, Villarroel, et al., 2016), measured in terms of volumetric change expressed either as a Jacobian (Jahani et al., 2015) or as regional volumetric strain and deformation invariants that quantify linear and surface changes (Hurtado et al., 2017). Further, spatial patterns of regional deformation obtained from DIR have been found to significantly differ from normal lungs in asthmatic patients (Choi et al., 2013) and patients with chronic obstructive pulmonary disease (Bodduluri et al., 2017), highlighting the potential of biomechanical analysis in understanding, and potentially detecting disease progression. Estimates of volumetric strain have been correlated with lung inflammation and injury in mechanically-ventilated lungs, suggesting that regional deformation obtained from DIR can be useful in the prevention of ventilation-induced lung injury in critical-care patients (Retamal et al., 2018b; Hurtado et al., 2020;

Cruces et al., 2020). A fundamental limitation of current DIR techniques and libraries is the poor performance experienced when images display motion discontinuities such as contact and organ sliding. Sliding typically occur inside the human body due to the existing lubricated interfaces between internal structures in the thoracic cage (e.g., lungs, chest wall, heart) (Amelon et al., 2011; Rodarte et al., 1985; Yin et al., 2010); and between the liver and other abdominal organs (e.g., kidney, diaphragm) (von Siebenthal et al., 2007; Hua, Pozo, Taylor, & Frangi, 2017). Interestingly, sliding in the lung fissures has been detected from computed-tomography (CT) images of the lungs using DIR methods, where supraphysiological levels of shearing deformation colocalize with the fissures (Amelon et al., 2014). While useful for anatomy detection purposes, no regional tissue distortion is expected to occur in sliding regions, which invalidates the accuracy of regional deformation estimates from traditional DIR methods in the lungs in regions close to fissures and the pleural cavity. The main responsible for such spurious deformation levels in sliding is the transformation model that most DIR methods assume, typically constructed using interpolation schemes that deliver globally continuous and smooth transformation mappings (Hua et al., 2015). As a consequence, traditional DIR methods cannot capture material interface or motion discontinuities, thus hindering the accuracy of the image registration and the associated biomechanical analysis (Hurtado, Villarroel, et al., 2016).

Traditional DIR techniques have been modified to capture sliding either by using alternative regularization terms, as well as enhanced transformation models (Schmidt-Richberg et al., 2012; Pace et al., 2013; Delmon et al., 2013; Hua et al., 2015). One example of the former is the diffusion-based approach (Thirion, 1998), where the normal component of the displacement field near the sliding boundaries is continuous, and a direction-dependent regularization term is assumed such that it penalizes jumps in the normal direction but allows for a discontinuous displacement field in the tangential direction (Schmidt-Richberg et al., 2012). This direction-dependent registration model shows good registration accuracy but underperforms when the intensity contrast near the boundaries is low, which can be the case of lobar fissures in CT images of the lung. A similar approach that employs local weighting and direction-dependent anisotropic diffusion smoothing resulted in more

realistic displacement fields than methods using global smoothing regularization (Pace et al., 2013). Alternatively, sliding motion in DIR has been approached by using novel transformation models that allow for discontinuities at predefined boundaries. One such example is the use of a linear combination of multiple B-spline functions and a sliding constraint (Delmon et al., 2013). This enhanced formulation of the classical free-form deformation (FFD) model (Rueckert et al., 1999) delivered accurate estimations of the displacement deformation field in 16 patients with lung cancer. A step further is the extension of the FFD free-form deformation method, which consists in enhancing B-spline basis functions with discontinuous functions that have jumps defined at the discontinuity surface (Hua et al., 2015, 2017), a formulation that has been termed extended FFD (XFFD). XFFD has shown to deliver high accuracy when registering synthetic images with strong sliding discontinuities, as well as lung and liver images where high levels of sliding are present. While incorporating additional constraints that account for organ sliding results in better deformation estimates, several limitations preclude them from their direct applicability in the analysis of regional strain deformation in the lungs. A key limitation presented by XFFD models, which is also shared by other B-spline methods (Delmon et al., 2013; Wu, Rietzel, Boldea, Sarrut, & Sharp, 2008) and diffusion-based methods (Schmidt-Richberg et al., 2012; Pace et al., 2013), is the fact that they rely on the definition of the sliding boundaries prior to the DIR analysis, which is typically done using semi-automatic segmentation methods, and largely depends on expert knowledge of the spatial location of the discontinuity boundaries. The a-priori definition of the sliding boundaries and the need for fine grids to capture curved surfaces where sliding occurs largely limit the applicability of current DIR methods in registering lung images, where the pleural cavity and fissures have intricate surface geometries and may not be easy to detect by the non-expert user.

The scientific question that motivates this work reads as follows: Is it possible to accurately capture sliding motion in DIR without the predefined knowledge of the sliding boundaries? To answer this question, in this work we aim at proposing and validating an inelastic DIR (i-DIR) method that allows for the automatic detection of sliding boundaries and that can handle discontinuous sliding motion on such surfaces.

3.2. Materials and Methods

3.2.1. Deformable image registration elastic formulation

In the following we adopt a variational framework for DIR problems (Modersitzki, 2003; Barnafi et al., 2018), which will be the starting point of the i-DIR formulation. Let $\Omega \subset \mathbb{R}^n$ be a domain of interest (image support), $R : \Omega \to \mathbb{R}$ be the *reference* image and $T : \Omega \to \mathbb{R}$ be the *target* image. The DIR problem aims to establish an optimal transformation $\boldsymbol{u} : \Omega \to \mathbb{R}^n$ that best aligns the reference and target images. To this end, we consider the functional space $\mathcal{V} := \boldsymbol{H}^1(\Omega, \mathbb{R}^n)$ and define a similarity functional $\mathcal{D} : \mathcal{V} \to \mathbb{R}$ that penalizes differences between the reference image R and the resampled target image $T \circ (\boldsymbol{id} + \boldsymbol{u})$, where the operator $\circ$ denotes function composition, and $\boldsymbol{id}$ stands for the identity function (i.e., $\boldsymbol{id} \longrightarrow \boldsymbol{id}(\boldsymbol{x}) = \boldsymbol{x}$). In practice, resampling an image considers an interpolation process, which is a type of estimation method where known data values (at the center of the pixel/voxel) are used to estimate new values at unknown points. The scheme used for the resampling of the images considers using cubic b-splines as the interpolation method. A popular choice for the similarity measure in mono-modal applications of DIR (Rueckert & Schnabel, 2011; Schmidt-Richberg, 2014) is the sum of squared-differences

$$\mathcal{D}[\boldsymbol{w}] := \frac{1}{2} \int_{\Omega} [T(\boldsymbol{x} + \boldsymbol{w}(\boldsymbol{x})) - R(\boldsymbol{x})]^2 d\Omega \quad , \forall \, \boldsymbol{w} \in \mathcal{V}, \tag{3.1}$$

which we will consider throughout this work. We remark that other choices of image similarity models such as those based on cross-correlation and mutual information measures can also be included in this formulation (Wells, Viola, Atsumi, Nakajima, & Kikinis, 1996; Barnafi et al., 2018). Further, we define a regularizer $\mathcal{S} : \mathcal{V} \to \mathbb{R}$ that provides smoothness to the optimal transformation as well as it avoids ill-posedness of the DIR problem. A popular choice due to its physical meaning is the elastic regularizer

$$\mathcal{S}[\boldsymbol{w}] := \int_{\Omega} W^e(\nabla \boldsymbol{w}) d\Omega, \tag{3.2}$$

where the elastic energy density takes the form

$$W^e(\nabla \boldsymbol{w}) := \mu \|\nabla \boldsymbol{w} + \nabla \boldsymbol{w}^T\|^2 + \frac{\lambda}{2}(\mathrm{div}\ \boldsymbol{w})^2, \tag{3.3}$$

with ∇ the gradient operator, div the divergence operator, and λ and μ the Lamé constants. With these elements, we define the elastic registration functional as

$$\Pi[\boldsymbol{w}] := \alpha \mathcal{D}[\boldsymbol{w}] + \mathcal{S}[\boldsymbol{w}], \tag{3.4}$$

where $\alpha > 0$ is a weighting parameter. Then, the optimal transformation $\boldsymbol{u}$ is the minimizer of the elastic registration functional, and the DIR problem is formulated as the following variational problem: Find $\boldsymbol{u}$ such that

$$\Pi[\boldsymbol{u}] = \min_{\boldsymbol{w} \in \mathcal{V}} \Pi[\boldsymbol{w}]. \tag{3.5}$$

From equations 3.4 and 3.5, we remark that the similarity term is not convex, so a convex regularizer is added. However, this does not guarantee the convexity of the problem, and, in fact, this is true for a very small value of α. In this sense, there is no guarantee that there will be uniqueness. Still, the problem has at least a global minimum because the similarity is positive, and the regularizer goes to infinity when the solution goes to infinity. This functional is said to be coercive. On the other hand, we note that the optimal transformation $\boldsymbol{u}$ can be interpreted as a displacement field that maps a point between its locations in the reference and target images. Moreover, the choice of the elastic deformation energy as a regularization term confers the DIR problem the physical interpretation of an elasticity problem (Lu, Chen, Olivera H., Ruchala, & Mackie, 2004), which has been widely exploited in the literature (Sotiras et al., 2013b). Further, and based upon this physical interpretation of the optimal transformation $\boldsymbol{u}$, we define the strain tensor operator

$$\boldsymbol{\varepsilon}(\boldsymbol{u}) := \frac{1}{2}\left(\nabla \boldsymbol{u} + \nabla \boldsymbol{u}^T\right), \tag{3.6}$$

and we note that the elastic energy density defined in (3.3) can be rewritten as

$$W^e(\boldsymbol{\varepsilon}) = \mu \boldsymbol{\varepsilon} : \boldsymbol{\varepsilon} + \frac{\lambda}{2}(\mathrm{trace}\ \boldsymbol{\varepsilon})^2, \tag{3.7}$$

where : signifies the tensor scalar (inner) product and trace represents the trace operator. We further define the stress tensor associated to this elastic energy by

$$\boldsymbol{\sigma}(\boldsymbol{\varepsilon}) := \frac{\partial W^e}{\partial \boldsymbol{\varepsilon}} = 2\mu\boldsymbol{\varepsilon} + \lambda\,\mathrm{trace}\,(\boldsymbol{\varepsilon})\boldsymbol{I}, \qquad (3.8)$$

where $\boldsymbol{I}$ is the identity tensor.

3.2.2. The inelastic deformable image registration (i-DIR) method

As discussed in the introduction, the elastic regularizer is not suited to handle discontinuities in the displacement field. As a result, sliding motion is not captured by traditional DIR methods. To address this limitation, here we draw ideas from the mechanics of inelastic solids, which aims at modeling inelastic deformation processes that result in localized softening in a solid. In the following, we briefly summarize the main ingredients of a traditional von Mises plasticity model, for a comprehensive review of the theory of inelastic solids we refer the reader to (Lubliner, 2013). Inelastic deformation in metals is driven by shearing deformation mechanisms, where sliding in the plane of maximum shearing occurs when the shear stress in that plane overcomes a critical yield stress, resembling frictional sliding motion.
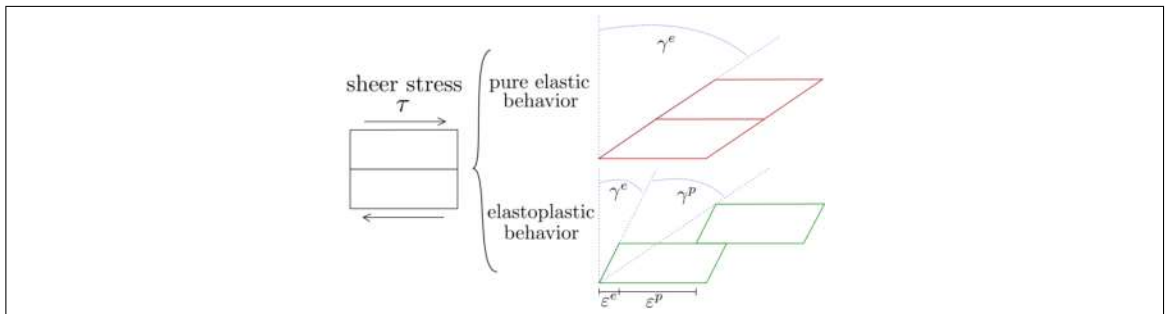
Figure 3.1. Schematics comparing the behaviour between an elastic and an inelastic approach

We note that the mechanical behavior of an inelastic solid is path dependent, which we represent through a time-dependence of the associated displacement field and strain tensors. To model inelastic deformation processes, we adopt the standard additive decomposition of the strain tensor

$$\varepsilon = \varepsilon^e + \varepsilon^p \tag{3.9}$$

where ε^e corresponds to the *elastic strain tensor* which is assumed to disappear as the load is removed, and ε^p is the *inelastic strain tensor* which captures permanent deformations (i.e. sliding) that will remain in the solid after the load is removed. A sketch of this traditional decomposition of deformations is included in Figure 3.1. For the purposes of image registration, we note the inelastic strain tensor will capture sliding that does not generate deformation in a tissue, and therefore we will quantify regional deformation solely based on the elastic strain tensor. The additive decomposition carries onto the instantaneous evolution of strain components, and we note that (3.9) implies that

$$\dot{\varepsilon} = \dot{\varepsilon}^e + \dot{\varepsilon}^p, \tag{3.10}$$

where $\dot{()}$ indicates partial derivatives with respect to time. To reflect the path-dependent nature of inelastic solids, we consider the effective inelastic strain $q \in \mathcal{M} := \boldsymbol{L}^2(\Omega, \mathbb{R})$ as the hardening internal variable. Following a thermodynamic formalism, we assume a free energy density function (for rate-independent plasticity) that extends the elastic energy density (3.7) and takes the form

$$\boldsymbol{A}(\varepsilon, \varepsilon^p, q) = W^e(\varepsilon - \varepsilon^p) + W^p(q), \tag{3.11}$$

where we assume that the stored plastic energy takes the form $W^p = \frac{1}{2}Hq^2$, with H being the hardening modulus. Then, the elastic constitutive relation reads

$$\boldsymbol{\sigma}(\varepsilon^e) = \frac{\partial W}{\partial \varepsilon^e} = 2\mu\varepsilon^e + \lambda \operatorname{trace}(\varepsilon^e)\boldsymbol{I}, \tag{3.12}$$

and the relation between the hardening internal variable and its thermodynamic conjugate stress is

$$\sigma_c(q) = \frac{\partial A}{\partial q} = Hq. \tag{3.13}$$

The inelastic behavior of a solid is modeled by defining a inelastic potential, also known as the yield function, which in the case of a von Mises solid takes the form

$$\Phi(\boldsymbol{\sigma}, \sigma_c) := \sqrt{\frac{3}{2} s_{ij} s_{ij}} - \sigma_c \tag{3.14}$$

where s_{ij} are the components of the deviatoric stress tensor $\boldsymbol{s}$ defined as

$$\boldsymbol{s}(\boldsymbol{\sigma}) := \sigma - \frac{1}{2} \operatorname{trace} \boldsymbol{\sigma} \boldsymbol{I}. \tag{3.15}$$

Following an associative plasticity framework (Lubliner, 2013), the evolution of the inelastic strain tensor is governed by the flow rule

$$\dot{\boldsymbol{\varepsilon}}^p = \dot{\gamma} \frac{\partial \Phi}{\partial \boldsymbol{\sigma}}(\boldsymbol{\sigma}, \sigma_c) = \dot{\gamma} \sqrt{\frac{3}{2}} \frac{\boldsymbol{s}}{\|\boldsymbol{s}\|} \tag{3.16}$$

where $\dot{\gamma}$ is the inelastic multiplier and the norm defined as $\|(\cdot)\| = \sqrt{(\cdot):(\cdot)}$. The evolution of internal variables is also dictated by the gradients of the inelastic potential

$$\dot{q} = -\dot{\gamma} \frac{\partial \Phi}{\partial \sigma_c}(\boldsymbol{\sigma}, \sigma_c) = \dot{\gamma}. \tag{3.17}$$

Finally, an inelastic model must comply with the loading/unloading complimentary conditions

$$\Phi(\boldsymbol{\sigma}, \sigma_c) \leq 0, \qquad \dot{\gamma} \geq 0, \qquad \dot{\gamma} \Phi(\boldsymbol{\sigma}, \sigma_c) = 0. \tag{3.18}$$

Complimentary conditions (3.18) are interpreted as follows: Inelastic deformations will occur ($\dot{\gamma} > 0$) only when the current stress state reaches the yield surface $\Phi(\boldsymbol{\sigma}, \sigma_c) = 0$. Otherwise, the inelastic evolution must be null to comply with (3.18), i.e., $\dot{\gamma} = 0$, which in turn implies that the change in total deformation will correspond only to changes in elastic deformation, as governed by (3.10).

In general, the relationship between $\dot{\varepsilon}^p$ and q is not independent. Let $\bar{\sigma}$ be the effective stress defined as

$$\bar{\sigma} = \sqrt{\frac{3}{2} s_{ij} s_{ij}}. \tag{3.19}$$

Then, the relation between $\dot{\varepsilon}^p$ and q is assumed to follow the *Prandtl-Reuss* flow rule that reads

$$\dot{\varepsilon}_{ij}^p = \dot{\bar{\varepsilon}}^p \left(\frac{3}{2} \frac{s_{ij}}{\bar{\sigma}} \right), \tag{3.20}$$

where $\dot{\bar{\varepsilon}}^p$ stands for the evolution of the accumulated plastic strain.

In view of the plastic flow rule, the accumulated plastic strain is equivalent to q, so by integration of (3.20) and assuming isotropic hardening, we have the following relation,

$$\bar{\varepsilon}^p = \int_0^t \sqrt{\frac{2}{3} \dot{\varepsilon}_{ij}^p \dot{\varepsilon}_{ij}^p} \, dt \equiv q \tag{3.21}$$

(see appendix B.1.1 for details).

3.2.3. Time and space discretization

Given $\dot{\varepsilon}$, the set of equations (3.10), (3.12), (3.13), (3.16) and (3.18) constitutes an inelastic constitutive initial value problem, which has been traditionally solved using a return-mapping algorithm based on an implicit backward-Euler temporal discretization. To this end, the time variable is discretized in generic subintervals $[t_n, t_{n+1}]$. Then, a series of incremental problems are obtained, where the main variables of the inelasticity model are assumed to be known at the time $t = t_n$, and need to be solved for $t = t_{n+1}$, giving rise to classical return-mapping algorithms. The details about the numerical discretization of return mapping algorithms can be found elsewhere (De Souza Neto, Perić, & Owen, 2008). Conveniently, the elastoplastic incremental problems can be reformulated as incremental variational (minimization) problems, which gives rise to the theory of variational updates in the computational solid mechanics community (Radovitzky & Ortiz, 1999; Ortiz & Stainier, 1999; Hurtado & Ortiz, 2013). In the following, we draw ideas from the theory of variational updates in plasticity to formulate the inelastic DIR model. The general

framework consists in formulating the evolution of an elastoplastic solid as a sequence of incremental variational minimization problems. To this end, we first integrate the flow rule (3.16) using a Backward-Euler scheme to obtain

$$\varepsilon_{n+1}^p - \varepsilon_n^p = (q_{n+1} - q_n)\sqrt{\frac{3}{2}}\frac{\boldsymbol{s}(\boldsymbol{\varepsilon}_{n+1} - \boldsymbol{\varepsilon}_{n+1}^p)}{\|\boldsymbol{s}(\boldsymbol{\varepsilon}_{n+1} - \boldsymbol{\varepsilon}_{n+1}^p)\|} \tag{3.22}$$

Solving for ε_{n+1}^p from the non-linear equation (3.22) delivers an incremental update for the inelastic strain tensor, which we express as

$$\varepsilon_{n+1}^p = \varepsilon_{n+1}^{*p}(\boldsymbol{\varepsilon}_{n+1}, q_{n+1}) \tag{3.23}$$

which depends solely of $\boldsymbol{\varepsilon}_{n+1}$ and q_{n+1}. Based on this flow-rule update, we define the effective incremental energy density for $t = t_n$ as (Ortiz & Stainier, 1999),

$$W_n(\boldsymbol{\varepsilon}) = \inf_{q_{n+1}} g_n(\boldsymbol{\varepsilon}, q_{n+1}) \tag{3.24}$$

where,

$$g_n(\boldsymbol{\varepsilon}, q_{n+1}) = \boldsymbol{A}\big(\boldsymbol{\varepsilon}, \varepsilon_{n+1}^{*p}(\boldsymbol{\varepsilon}, q_{n+1}), q_{n+1}\big) - \boldsymbol{A}_n + \Delta t \cdot \psi^*\left(\frac{|q_{n+1} - q_n|}{\Delta t}\right) \tag{3.25}$$

where $\Delta t = t_{n+1} - t_n$, and ψ^* stands for the *dual dissipation potential* (Ortiz & Stainier, 1999) that governs the time evolution of the hardening variable, which in our case is defined as $\psi^* = \sigma_y |\Delta q|$, with $\Delta q = q_{n+1} - q_n$. The minimization problem involved in the definition (3.25) is equivalent to the stationary condition

$$0 \in \frac{\partial \boldsymbol{A}}{\partial q_{n+1}} + \partial\psi^*\left(\frac{|q_{n+1} - q_n|}{\Delta t}\right) \tag{3.26}$$

which, for the rate-independent case reads (see details in appendix B.1.2),

$$\bar{\sigma}_{n+1}^{pre} - 3\mu\Delta q - \sigma_c(q_{n+1}) = \partial\psi^*\left(\frac{|q_{n+1} - q_n|}{\Delta t}\right) \tag{3.27}$$

where $\bar{\sigma}_{n+1}^{pre}$ is the elastic predictor for $\bar{\sigma}_{n+1}$. Substituting (3.13) into (3.27) we obtain

$$\bar{\sigma}_{n+1}^{pre} - 3\mu\Delta q - H(q_n + \Delta q) - \partial\psi^*\frac{|\Delta q|}{\Delta t} = 0 \tag{3.28}$$

where the sub-differential of ψ^* is defined as:

$$\partial\psi^* = \begin{cases} [-\sigma_y, \sigma_y] & \text{if} \quad \Delta q = 0 \\ \sigma_y & \text{if} \quad \Delta q > 0 \\ -\sigma_y & \text{if} \quad \Delta q < 0 \end{cases} \tag{3.29}$$

The solution of Δq from (3.28) involves two mutually exclusive steps, giving rise to a return-mapping algorithm which involves an elastic predictor and a plastic corrector steps, see Appendix B.1.3.

With the definition of the effective incremental energy density, we now postulate the inelastic DIR formulation as a sequence of effective variational problems. For a generic time step, the displacement field $\boldsymbol{u}_n$ is assumed to be known, and we find the displacement field $\boldsymbol{u}_{n+1}$ by solving the problem

$$\Pi_n^{\text{eff}}[\boldsymbol{u}_{n+1}] = \min_{\boldsymbol{w} \in \mathcal{V}} \Pi_n^{\text{eff}}[\boldsymbol{w}], \tag{3.30}$$

where the inelastic DIR functional reads

$$\Pi_n^{\text{eff}}[\boldsymbol{w}] = \mathcal{S}_n^{\text{eff}}[\boldsymbol{w}] + \alpha\mathcal{D}[\boldsymbol{w}], \tag{3.31}$$

and the inelastic regularizing term takes the form

$$\mathcal{S}_n^{\text{eff}}[\boldsymbol{w}] = \int_\Omega W_n(\varepsilon(\boldsymbol{w})). \tag{3.32}$$

To solve the minimization problem (3.30) we consider the stationary condition

$$\mathbf{R}_n[\boldsymbol{w}; \boldsymbol{v}] := \frac{d}{d\epsilon}\Pi_n^{\text{eff}}[\boldsymbol{w} + \epsilon\boldsymbol{v}]_{\epsilon=0} = 0, \qquad \forall \boldsymbol{v} \in \mathcal{V}. \tag{3.33}$$

The residual in (3.33) takes the form

$$\mathbf{R}_n[\boldsymbol{w}; \boldsymbol{v}] := \alpha \int_\Omega \boldsymbol{v} \cdot (T(\boldsymbol{w}) - R)\nabla T(\boldsymbol{w}) + \int_\Omega \varepsilon(\boldsymbol{v}) : \sigma_{n+1}(\varepsilon(\boldsymbol{w})), \tag{3.34}$$

where

$$\boldsymbol{\sigma}_{n+1}(\boldsymbol{\varepsilon}) := \frac{\partial W_n}{\partial \boldsymbol{\varepsilon}}(\boldsymbol{\varepsilon}), \tag{3.35}$$

represents the stress tensor update (Ortiz & Stainier, 1999). The residual equation (3.33) constitutes a nonlinear problem, which we approach by means of linearization. To this end, we consider the Gauteaux differential defined as

$$\mathbf{TR}[\boldsymbol{w}, \boldsymbol{v}; \Delta \boldsymbol{w}] := \alpha \int_\Omega \boldsymbol{v} \cdot \left\{ \nabla T(\boldsymbol{w}) \otimes \nabla T(\boldsymbol{w}) + (T(\boldsymbol{w}) - R)\nabla\nabla T(\boldsymbol{w}) \right\} \cdot \Delta \boldsymbol{w}$$
$$+ \int_\Omega \varepsilon(\boldsymbol{v}) : \mathbf{D}^{ep}_{n+1} \, \varepsilon(\Delta \boldsymbol{w}), \tag{3.36}$$

where

$$\mathbf{D}^{ep}_{n+1}(\boldsymbol{\varepsilon}) := \frac{\partial^2 W_n}{\partial \boldsymbol{\varepsilon}^2}, \tag{3.37}$$

is the consistent tangent tensor, see Appendix B.1.4. Thus, the linearized version of the residual problem reads: Given an initial guess $\boldsymbol{w} \in \mathcal{V}$, find the increment $\Delta \boldsymbol{w}$ such that

$$\mathbf{R}_n[\boldsymbol{w}; \boldsymbol{v}] + \mathbf{TR}[\boldsymbol{w}, \boldsymbol{v}; \Delta \boldsymbol{w}] = 0 \quad \forall \quad \boldsymbol{v} \in \mathcal{V}, \tag{3.38}$$

and we iterate over this linearized problem until a convergence criterion is reached.

To solve the continuous linear variational problem defined in (3.38) we adopt a Ritz-Galerkin finite-element approach. To this end, we construct the finite-element space

$$\mathcal{V}^h = \left\{ v^h : \Omega^h \to \mathbb{R}^n \mid v^h := \sum_{A=1}^m N_A v_A, \text{with } v_A \in \mathbb{R}^n \right\} \subset \mathcal{V}, \tag{3.39}$$

where $\{N_1, \ldots, N_m\}$ is the set of basis functions. Using this finite-element space, we approximately solve the variational problem (3.38), i.e., we solve the problem: Given an initial guess $\boldsymbol{u}^h$, find the increment $\Delta \boldsymbol{u}^h$ such that

$$\mathbf{R}_n[\boldsymbol{u}^h; \boldsymbol{v}^h] + \mathbf{TR}_n[\boldsymbol{u}^h, \boldsymbol{v}^h; \Delta \boldsymbol{u}^h] = 0 \quad \forall \quad \boldsymbol{v}^h \in \mathcal{V}^h. \tag{3.40}$$

Using standard arguments (e.g., see (Hurtado & Henao, 2014)) we can show that (3.40) is equivalent to solving the linear system of equations

$$\mathbf{K}_n \Delta \mathbf{u} = \mathbf{F}_n, \qquad (3.41)$$

where $\Delta \mathbf{u}$ is a vector with the nodal values of the increment $\Delta \boldsymbol{u}^h$, $\mathbf{K}_n$ is the tangent matrix and $\mathbf{R}_n$ is the residual for the previous guess, all of which are defined in Appendix B.1.5. After convergence is reached for the Newton step, the internal variables q at t_{n+1} are updated and stored at the element level. We further note that, in order to provide stability and unisolvence of the problem, we adopt the approach set forth in (Barnafi et al., 2018), where we impose orthogonality conditions to the displacement fields and assume Neumann boundary conditions. We test other alternatives of boundary conditions such as Dirichlet conditions. However, the results were not successful. In particular, we aim to develop a model in which the mesh was not fixed in space and could deform without restrictions (in terms of embedment).

3.2.4. Performance assessment and metrics

The i-DIR method was implemented using an in-house Python code. In order to contrast the results of the i-DIR method with other DIR methods, we considered the open source Nifty Reg library (Modat, Mcclelland, & Ourselin, 2010) which efficiently implements the FFD method (Rueckert et al., 1999) with elastic regularization. To understand the effect of the inelastic regularization term over the purely elastic counterpart for a FE method, we also consider the comparison with an Elastic FEM registration, also coded in Python. To study the performance of the three methods considered here (FFD, Elastic FEM, and i-DIR), we constructed synthetic reference and target images that simulated planar sliding over a chessboard-like image studied by Hua and co-workers (Hua et al., 2017), which we refer to as the synthetic dataset with sliding motion, see Figure 3.2. The synthetic images have a size of 80×80 pixels (with an isotropic pixel spatial resolution of 1[mm] in the x, y direction), and the target image is constructed in such a way that it resembled a dislocation or sliding motion, with a known displacement of 5

pixels. We remark that, as the motion corresponds to a uniform vertical displacement (i.e., rigid body motion in both blocks) of the right-hand side of the image, the exact strain field is equal to zero, as rigid motions do not generate strain. To assess the method's performance on anatomical images, we considered sagittal planes of CT thorax images of a normal volunteer under spontaneous breathing at total lung capacity (reference image) and functional residual capacity (target image), see Figure 3.3. The images were randomly selected from a small CT lung dataset of normal subjects employed in a previous study (Hurtado et al., 2017), and the sagittal planes were arbitrarily chosen so that large deformations were explicitly depicted to capture sliding. The image size of the sagittal slice is 247×346 pixels, where each pixel has an anisotropic spatial resolution of 0.008[mm] and 0.006[mm] in the x, y direction, respectively.
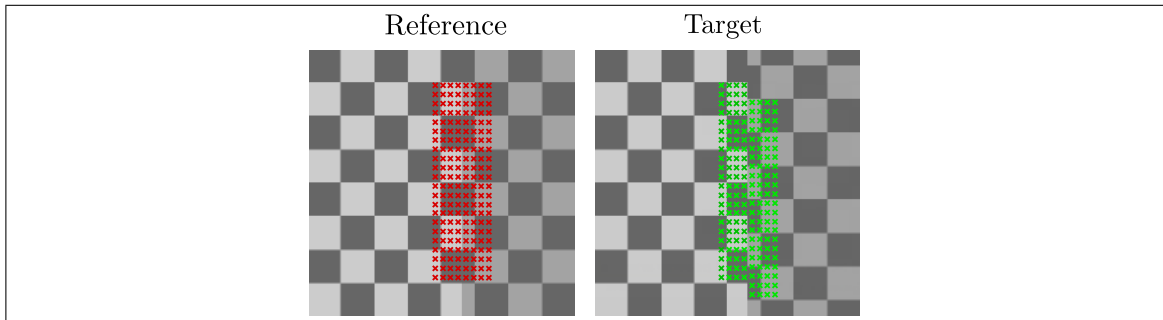
Figure 3.2. Synthetic dataset with sliding motion: Reference (left) and target (right) images. Landmarks used for computing the TRE are shown in red for the reference image and in green for the target image.
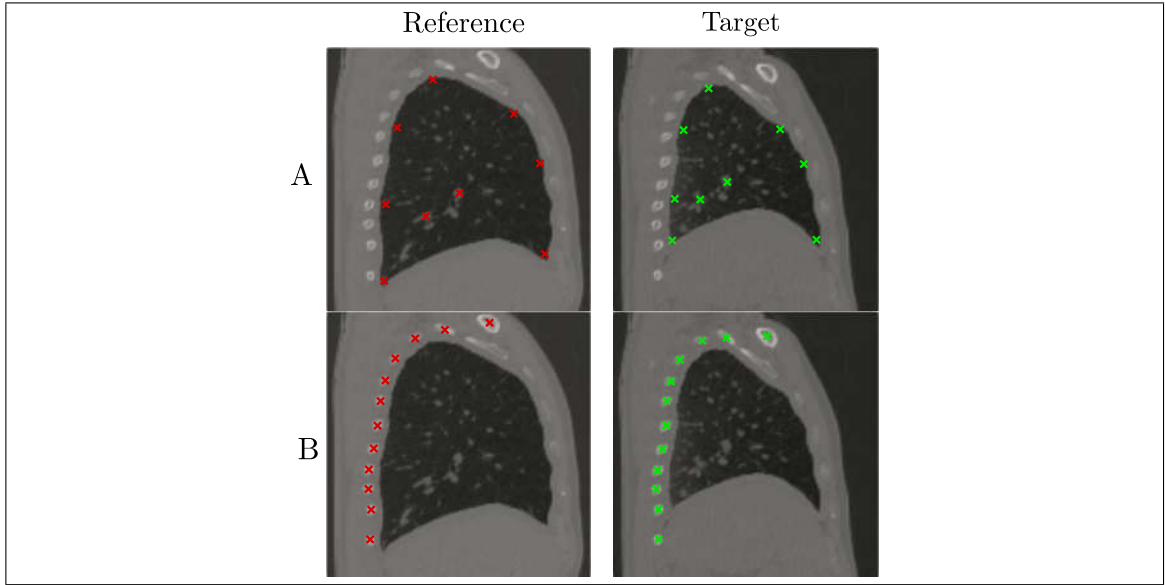
Figure 3.3. Lung dataset: Reference (left) and target (right) images. *Row A*: TRE analysis using landmarks inside the lung. *Row B*: TRE analysis using using landmarks on the dorsal ribs. Red and green marks indicate landmarks in the reference and target images, respectively.

To quantitatively evaluate the performance of the DIR methods, we considered the traditional residual sum of squared differences (RSS) between the reference and resampled images, defined as:

$$RSS = \sum_{i=1}^{m} \sum_{j=1}^{n} (R_{ij} - (T \circ (\boldsymbol{id} + \boldsymbol{u}))_{ij})^2. \tag{3.42}$$

In practice, the resampling process considers an interpolation method using cubic b-splines. In addition, the normalized target registration error (TRE) was also computed. The TRE is defined as

$$TRE = \frac{\sum_{i=1}^{N} \sqrt{(p_i - q_i)^2}}{N} \tag{3.43}$$

where $p_i(x, y)$ and $q_i(x, y)$ are the ith landmark in the target image (fixed landmark) and the moving landmark, respectively, and N is the total number of landmarks. For the synthetic dataset, 375 landmarks were positioned around the discontinuity surface, as shown in Figure 3.2. In the case of the lung dataset, two sets of landmarks were

considered, to analyze the effect of landmark selection and position regarding the sliding surface. The first case considered 9 landmarks positioned entirely inside the lung (Figure 3.3, top row). The second case considered 12 landmarks placed in the ribs of the dorsal region (Figure 3.3, bottom row).

In addition to the RSS and TRE metrics, the resampled image ($T \circ (id + \boldsymbol{u})$), difference image ($R - T \circ (id + \boldsymbol{u})$), and warped reference image (($\boldsymbol{\varphi}, R$)) are reported for all cases. To study the mechanical performance of all the methods studied, we constructed images of the elastic volumetric strain, defined as

$$\varepsilon^e_{vol} := \operatorname{trace}(\boldsymbol{\varepsilon}^e), \tag{3.44}$$

and images of the elastic von Mises strain, which takes the form

$$\varepsilon^e_{vm} := \sqrt{\frac{2}{3}\boldsymbol{\varepsilon}^e : \boldsymbol{\varepsilon}^e}. \tag{3.45}$$

We note that for purely elastic methods (FFD, Elastic FEM), the elastic strain tensor $\boldsymbol{\varepsilon}^e$ is replaced by the total strain tensor $\boldsymbol{\varepsilon}$ in (3.44) and (3.45). Finally, a sensitivity analysis is conducted for the i-DIR method on the synthetic dataset to understand the effect of the initial yield stress on its registration performance. Throughout this chapter, the DIR-based 2D imaging biomechanical models assume to have no out-of-plane deformations. In mechanics, this condition is known as *plane strain*, in which there is zero strain in the direction normal to the axis of the applied forces (i.e., $u_z = 0$). Therefore, although it is a 2D domain, the deformation can be considered volumetric. It is imperative to point out that this assumption is only a hypothesis and that it is not necessarily always fulfilled, which constitutes a limitation of the biomechanical model.

3.2.5. Parameter settings

For the FEM models (elastic FEM and i-DIR), we established an incremental approach for the weighting parameter α. We set an initial value of $\alpha = 0.01$, and once a convergence

tolerance was exceeded, we systematically increased α, until we reach a value of $\alpha = 1400$. Since the problem is not convex, it is necessary to define small increments of α. In practice, the increment ($\Delta\alpha$) is variable and depends on the magnitude of α. For example:

$$
\begin{aligned}
&\text{if} \quad \alpha \leq 1 &&\longrightarrow \quad \Delta\alpha = \quad 11\% \text{ of } \alpha \\
&\text{if} \quad 1 < \alpha \leq 10 &&\longrightarrow \quad \Delta\alpha = \quad 8\% \text{ of } \alpha \\
&\text{if} \quad 10 < \alpha \leq 20 &&\longrightarrow \quad \Delta\alpha = \quad 5\% \text{ of } \alpha \\
&\text{if} \quad 20 < \alpha \leq 80 &&\longrightarrow \quad \Delta\alpha = \quad 4\% \text{ of } \alpha \\
&\text{if} \quad 80 < \alpha \leq 150 &&\longrightarrow \quad \Delta\alpha = \quad 2\% \text{ of } \alpha \\
&\text{if} \quad 150 < \alpha \leq 300 &&\longrightarrow \quad \Delta\alpha = \quad 0.8\% \text{ of } \alpha \\
&\text{if} \quad 300 < \alpha \leq 1000 &&\longrightarrow \quad \Delta\alpha = \quad 0.2\% \text{ of } \alpha \\
&\text{if} \quad \alpha > 1000 &&\longrightarrow \quad \Delta\alpha = \quad 0.07\% \text{ of } \alpha
\end{aligned}
$$

An L-curve analysis was attempted to find an optimal value for α; however, the results were erratic. No other sophisticated method was used to find an optimal α, just by trial and error. For the Lamé constants (μ, λ), the initial yield limit (σ_0) and the hardening modulus (H), we adopted the following heuristic values:

Table 3.1. Parameter settings

Parameter	Value
μ	1.36
λ	0.34
σ_0	0.1
H	0.3

We did not perform any sensitivity analysis regarding parameters μ, λ, and H. We chose them arbitrarily. However, we test different values for σ_0. In particular, we vary

σ_0 between 0.005 and 10 to assess its effect on the performance of the model through the RSS error.

Following the pyramidal approach described in (Modat, Mcclelland, & Ourselin, 2010), the entire registration model consisted of an initial global registration (i.e., affine transformation) and three consecutive local registration processes (FFD algorithm). In the FFD algorithm, cubic B-Spline are used to deform a source image to optimize an objective function based on a normalized mutual information similarity measure and a penalty term. The penalty term associated with the FFD model, also known as bending energy (BE), was set to: $BE_1 = 1 \times 10^{-9}$, $BE_2 = 2.5 \times 10^{-6}$ and $BE_3 = 1 \times 10^{-4}$, for the three local registration respectively. For clarity, when the FFD model is mentioned throughout this chapter, it refers to the full pyramidal model (both global and local registration).

In terms of numerical discretization, both the elastic FEM and i-DIR models, employed structured triangular finite element meshes. As shown in Figure 3.4, the synthetic dataset used a mesh of 5618 elements and a mesh of 18860 elements for the lung dataset, leaving a triangle size of $1.139[\text{mm}^2]$ and $4.531[\text{mm}^2]$ for the synthetic and the lung cases, respectively. For visualization purposes, we further refined our results into structured meshes of size 64800 and 28800 elements for the synthetic and lung dataset, respectively. As for the FFD model, we projected the deformation mapping field (output) and compute the mechanical measures into a refined structured triangular finite element mesh of the same size as the FEM DIR models, in order to have a fair comparison. We remark that for the lung images, we consider the entire image domain in the mesh. Motivated by evaluating how the deformation between the lung and its environment behaves, we decided to mesh the whole domain and not just the isolated lung.
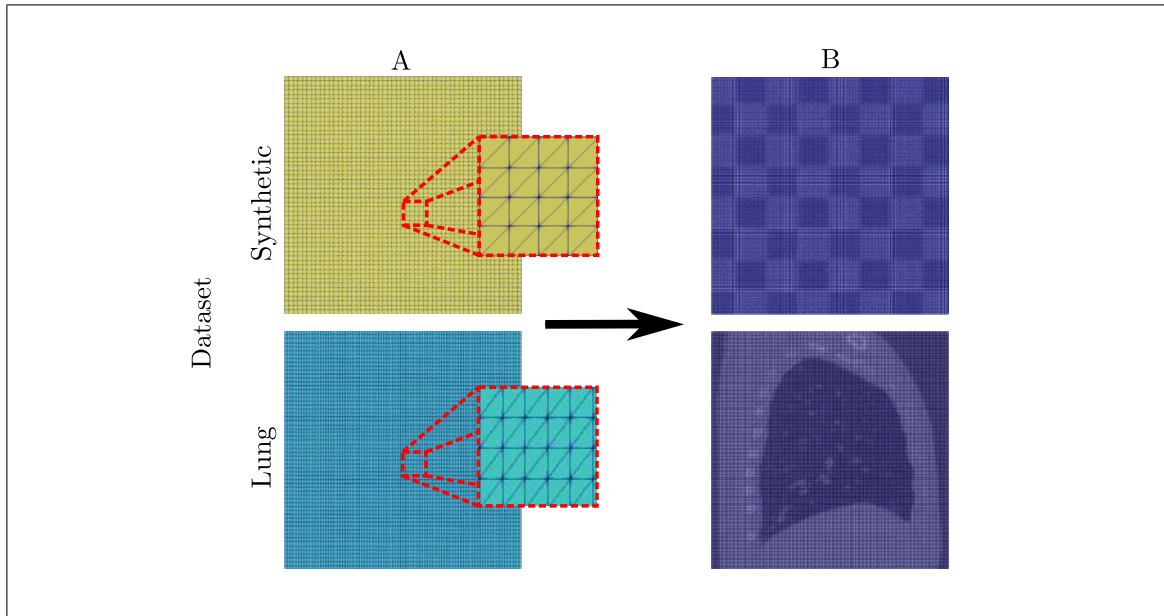
Figure 3.4. Numerical discretization of the synthetic and lung datasets. (Column A) Structured triangular meshes and (Column B) refined structured triangular meshes.

All models, FE discretization, biomechanical analysis, image processing, and statistics, were coded in Python using a processor Intel Core i7-8750H CPU @ 2.20GHz × 12.

3.3. Results

In terms of image color maps, as in Chapter 2, the results shown in this chapter differ from the images in the published article. Its original form can be found in the Supplementary Material B.2.

3.3.1. Synthetic dataset with sliding motion

The performance of each registration model using the synthetic dataset with sliding motion is reported in terms of resampled and difference images in Figure 3.5. The i-DIR method accurately captures the vertical sliding and delivers the best resampled image,

when compared to the other elastic methods (Figure 3.5, top row). Most of the errors in the resampled images are located in a small neighborhood of the line where sliding takes place. When analyzing the difference images (Figure 3.5, bottom row), the FFD method results in considerable voxel-wise differences at the boundaries of the squares that propagate from the sliding line throughout the checkerboard domain. In contrast, small differences are observed around the sliding line in the elastic FEM case. No visible differences are observed for the i-DIR case when compared to the other two methods.

Reference image is included for comparison purposes.
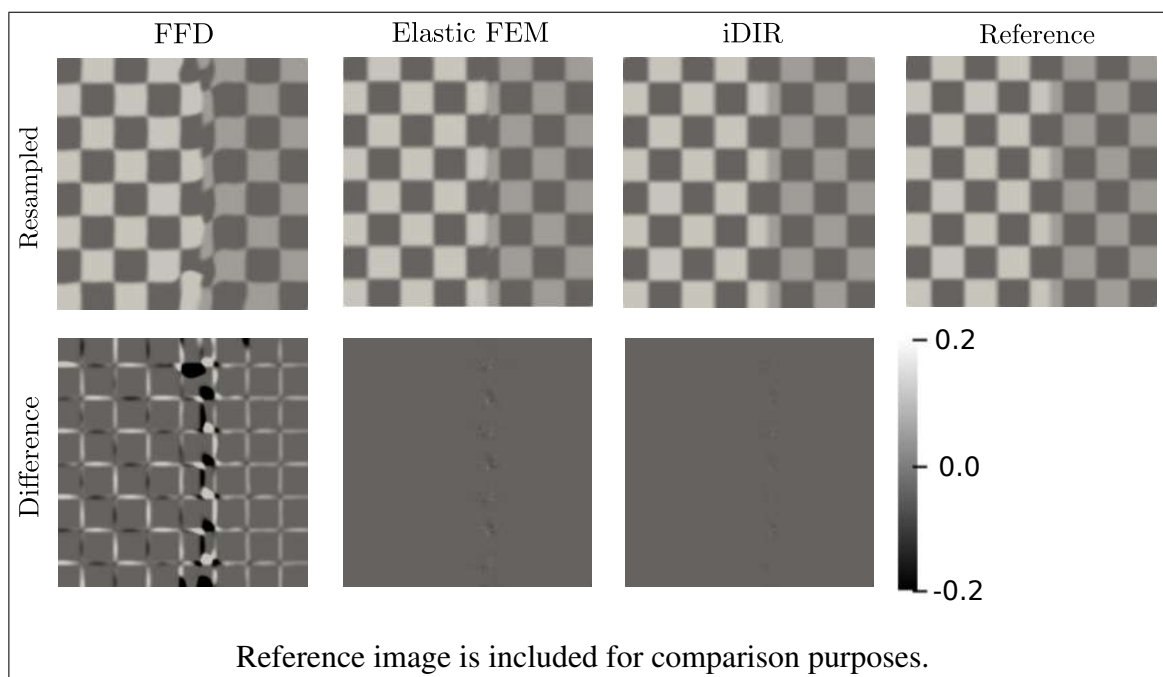
Figure 3.5. Registration of synthetic dataset with sliding motion. (Top row) resampled images using FFD, Elastic FEM and i-DIR methods and Reference image, (bottom row) difference images. Colorbar indicates the intensity (normalized between $[-1, 1]$) difference between images.

Warped reference images showing the resulting displacement field for each method are reported in Figure 3.6. A close-up around the sliding region shows a continuous displacement field with a vortex-like pattern over the sliding line that slowly dissipates to the right for the FFD case. A similar displacement field pattern is observed for the elastic FEM case, but with an attenuated vortex pattern. In contrast, the i-DIR method delivers a

uniformly vertical displacement field on the region to the right of the sliding line, and zero displacements to the left of the sliding line, being able to identify the discontinuity surface as well as capturing the discontinuous displacement field.
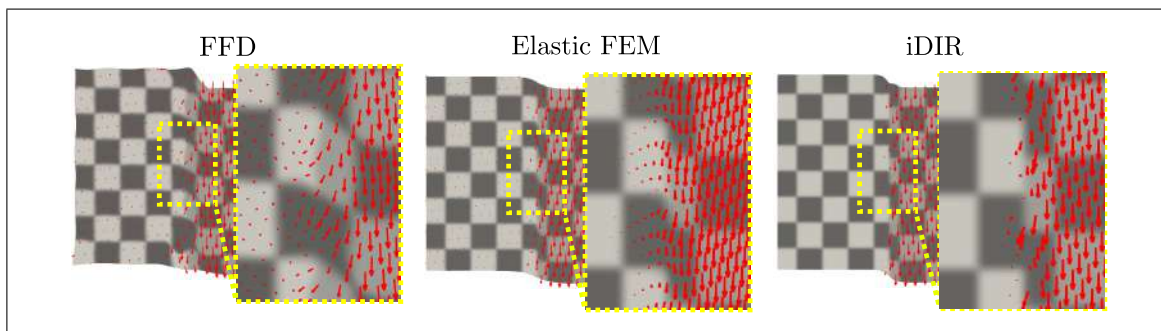
Figure 3.6. Warped reference image and displacement field for the synthetic dataset with sliding motion. Red arrows show the displacement field in a neighborhood of the sliding plane

The RSS and TRE metrics for all three methods are shown in Table 3.2. The i-DIR method delivers the lowest values for these performance metrics, followed by the Elastic FEM method.

Table 3.2. Performance metrics for the synthetic dataset

Model	RSS	TRE
FFD	16.32	1.17
Elastic FEM	3.19	0.46
i-DIR	0.28	0.22

Figure 3.7 shows the elastic deformation fields associated to the three registration methods. The elastic volumetric strain displayed by the FFD model, shows an erratic pattern throughout the entire image, with high values of both compressive (peak value of -1.22) and expansive (peak value of 0.83) deformation near the vicinity of the discontinuity

surface. The case of the elastic FEM model delivers a volumetric strain field with localized strain concentrations around the sliding surface with peak values of -0.75 and 1.27. In contrast, the i-DIR model delivers a volumetric strain field that is zero in the majority of the region of analysis, with small concentrations around the sliding surface with peak values of -0.39 and 0.63. The resulting elastic von Mises strain field, which characterizes shear distortions, is shown in the bottom row of Figure 3.7. Similarly to the case of volumetric strain, the FFD method results in a highly oscillating field that take on non-zero values everywhere in the image domain, reaching peak values of 1.72. The Elastic FEM method displays high strain concentrations around the sliding plane with peak von Mises strain values that are similar to the FFD case (2.38), but the strain field rapidly dissipate away from the discontinuity plane. In contrast, the i-DIR results in a narrow region around the sliding plane with low values (peak value of 0.38), with the rest of the image domain resulting in zero von Mises strain.
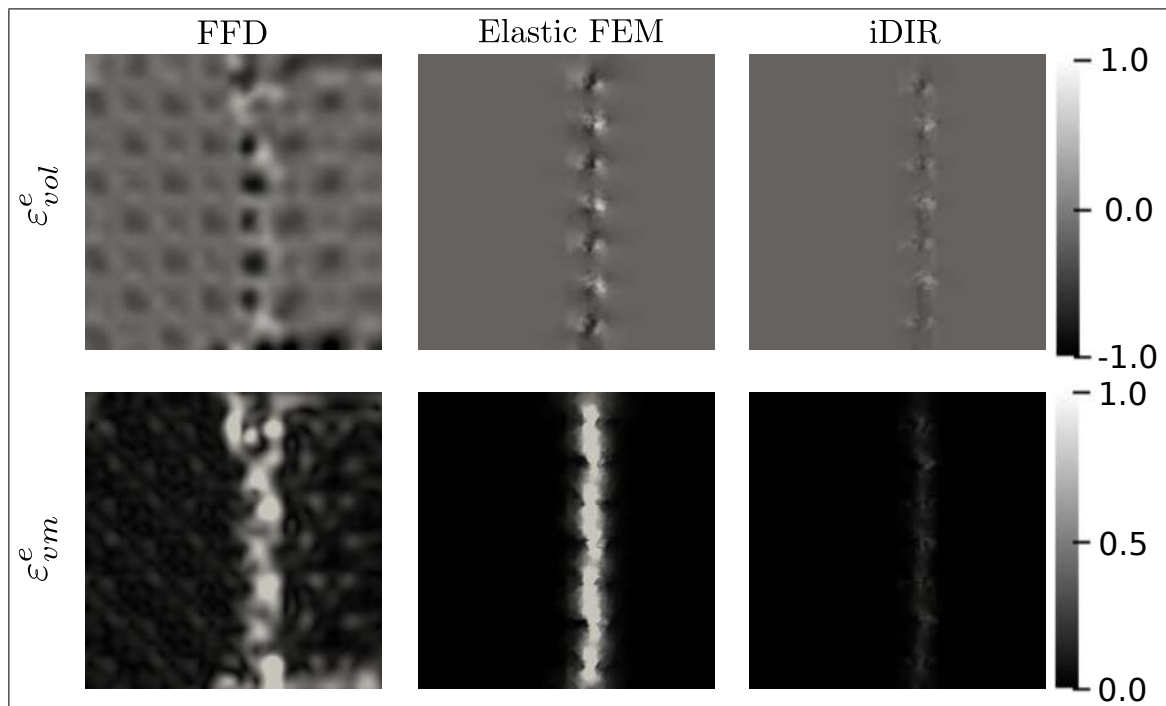
Figure 3.7. Elastic deformation fields for the synthetic dataset with sliding motion resulting from the different registration methods: elastic volumetric strain (top row, colorbar displays strain magnitude), and elastic von Mises strain (bottom row, colorbar displays strain magnitude).

The sensitivity of the RSS error to the value of the initial yield stress in the i-DIR method is shown in Figure 3.8. Yield stress values smaller that 0.1 result in RSS errors that do no change considerably, delivering the highest accuracy observed for all three methods. In contrast, yield stress values above 1.0 deliver a much higher RSS error, which approaches that of the Elastic FEM method, see Table 3.2.
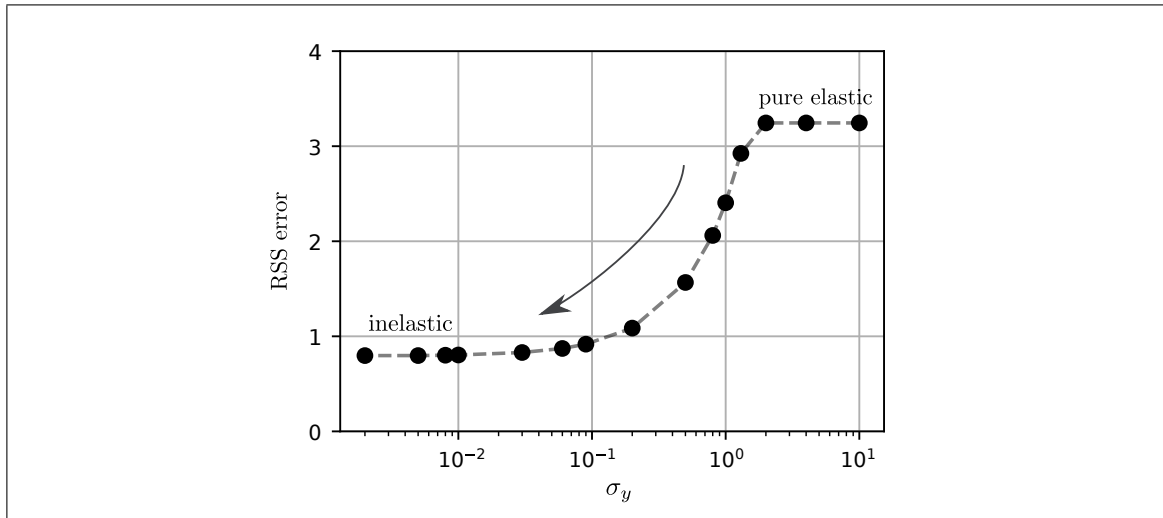
Figure 3.8. Sensitivity of the i-DIR method, measured in terms of RSS error, to the choice of initial yield stress value.

3.3.2. Registration of lung CT images

Resampled and difference images for the lung CT dataset are shown in Figure 3.9, top row. All three methods deliver similar results of the resampled image. We note however, that resampled images from both the FFD and Elastic FE methods show distorted rib cuts in the dorsal region, while the ribs are accurately resampled in the case of the i-DIR method. The misalignment of the ribs is also observed in the difference images of the FFD and Elastic FEM cases, see Figure 3.9, bottom row. In contrast, the i-DIR case reports zero difference values in the regions where ribs are located.
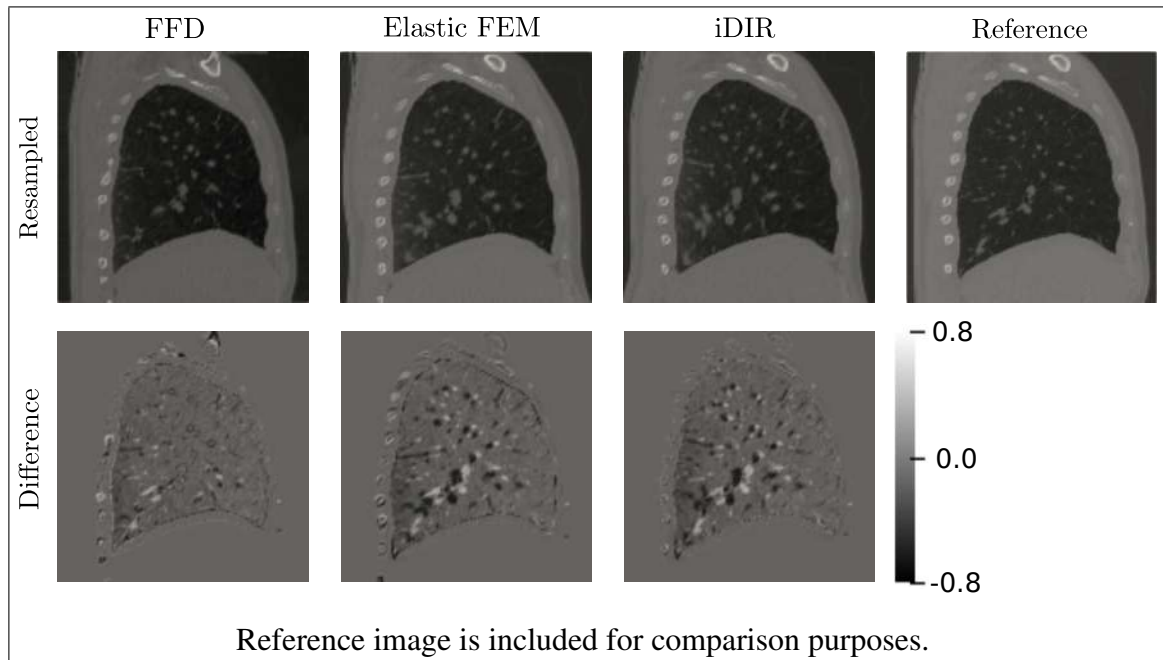
Figure 3.9. Registration of the lung dataset and comparison between methods. (Top row) resampled images, (bottom row) difference images. Colorbar indicates the intensity (normalized between $[-1, 1]$) difference between images.

Warped reference images are shown in Figure 3.10, where a close-up shows the displacement fields around the sliding pleural cavity. A continuous, and almost uniform upward displacement field is observed for the case of the FFD and Elastic FE methods. In contrast, the i-DIR method delivers an upward displacement field inside the lung, right next to a region comprising the ribs with null displacement, with the jump in displacement magnitude located on the sliding pleural cavity.
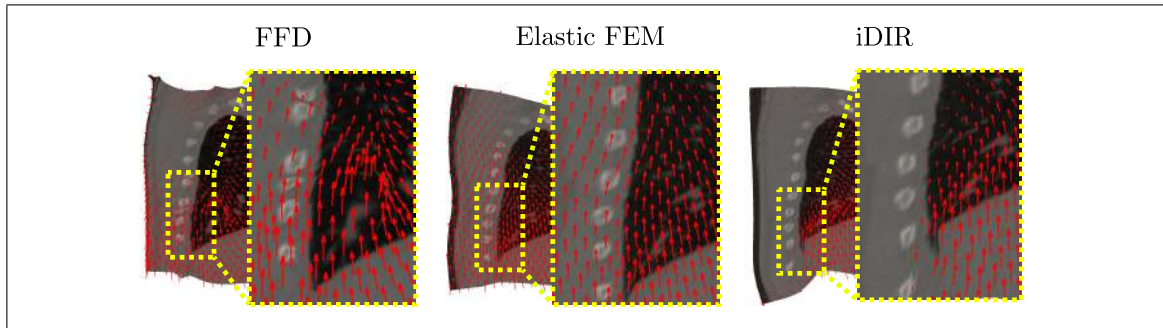
Figure 3.10. Warped reference image and displacement field for the lung dataset. Red arrows show the displacement field in a neighborhood of the sliding surface.

Performance metrics for the lung dataset are included in Table 3.3. We note that all three methods result in similar values for the case of RSS and TRE using inside-lung landmarks. However, the i-DIR method shows a remarkable advantage over the other methods for the case of TRE using rib landmarks.

Table 3.3. Performance metrics for the lung dataset.

Model	RSS	TRE (inside-lung landmarks)	TRE (rib landmarks)
FFD	11.64	6.82	13.98
Elastic FEM	13.25	6.74	13.68
i-DIR	12.24	6.99	0.77

The elastic volumetric strain distribution resulting from the registration of lung images are shown in Figure 3.11, top row. The FFD model delivers a highly oscillating field that results in excessive strain values with peaks as high as -1.68 and 1.02, located both inside and outside the lung domain. In contrast, the Elastic FEM model displays a more uniform volumetric strain distribution inside the lung, with a smooth pattern of strain. However, high strain localizations are observed outside the lung in the dorsal region where the ribs

are located, with oscillating values. The i-DIR model delivers a smooth distribution of volumetric strain inside the lung, that quickly transitions to small levels of strain immediately outside the lung. Further, the largest strain levels are found in the regions near the diaphragm. Outside the lung, we mostly observe zero volumetric deformation throughout the remaining image domain. The von Mises strain fields are shown in Figure 3.11, bottom row. Similarly to the case of volumetric strain, the FFD model delivers a highly oscillating field with a peak value in the order of 1.7 both outside and inside the lung. The Elastic FEM method results in a distribution with smaller strain magnitudes, which in some parts of the lung boundary are rapidly reduced to zero. In the case of the i-DIR method, a smooth distribution of non-zero strain is observed inside the lung with the highest values close to the diaphragm and dorsal region. The von Mises strain distribution sharply decays to zero in the regions outside the lung.
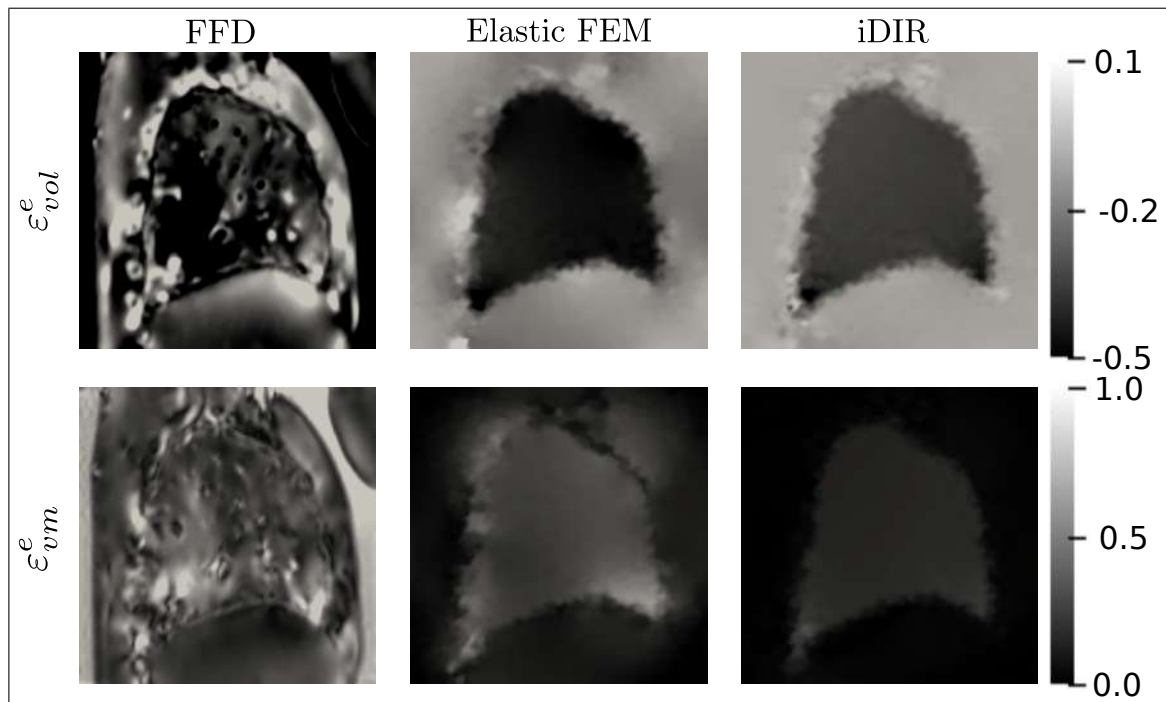

Figure 3.11. Elastic deformation fields for the lung dataset resulting from the different registration methods: elastic volumetric strain (top row, colorbar displays strain magnitude), and elastic von Mises strain (bottom row, colorbar displays strain magnitude).

3.4. Discussion

The results for the synthetic dataset with sliding motion show that among the three DIR methods studied, the i-DIR delivers the best resampled image, accurately accommodating the sliding motion, see Figure 3.5, top row. We note that the elastic DIR methods suffer from spurious displacements around the sliding line that result in distorted resampled images, see Figure 3.5, bottom row. Further, the i-DIR method is capable of capturing the discontinuous displacement field imposed by the sliding motion, while elastic DIR methods fail to capture the jump in displacements and result in spurious displacement fields, see Figure 3.6. Further, we have shown that for this example, the i-DIR method consistently delivers RSS and TRE metrics that confirm the superior performance of the i-DIR method when compared to the Elastic FEM and FFD methods, see Table 3.2. Other methods proposed in the literature have also shown a remarkable performance in the registration of the synthetic dataset with sliding motion. In particular, the XFFD method has shown to be capable of accurately capture the sliding motion by introducing a discontinuous transformation model that delivers an optimal resampling (Hua et al., 2017). To this end, the XFFD method necessitates the definition of the sliding surface *a priori* in order to deliver accurate and efficient results. Here, we have shown that the i-DIR method does not require *a priori* information about the sliding surface. Further, the sliding plane did not coincide with any element edges in the discretization. This feature represents an important advantage over existing methods, as the i-DIR is capable of detecting sliding discontinuities in an automatic way, lending itself to the registration of images with arbitrary sliding discontinuities.

From the perspective of quantifying local deformation by means of DIR, we remark that the sliding mechanism present in the synthetic dataset corresponds to a rigid (sliding) motion between two adjacent blocks, and therefore no deformation is expected to occur in any of the blocks after sliding. Figure 3.7 shows that the FFD method induces spuriously high levels of both volumetric and deviatoric deformations around the sliding plane,

which is consistent with previous findings for the synthetic dataset with sliding motion (Hua et al., 2017). Similarly to the case of the displacement field, the strong warping and deformation propagates throughout the image domain, creating nonphysical high volumetric and deviatoric strain levels away from the discontinuity. The error in the strain predictions is strongly attenuated by the elastic FE method, which still concentrates high values in a neighborhood of the sliding plane. In contrast, the i-DIR method reports low levels of deviatoric deformation on a narrow band around the discontinuity surface, and negligible errors in the estimation of volumetric strain, see Figure 3.7. This result shows that the i-DIR method not only automatically captures the sliding motion with accuracy, but also delivers precise estimates of the strain fields, even in the present of strong discontinuities.

The sensitivity of the iDIR model to the yield stress parameter shows that for parameter values $\sigma_y \leq 10^{-2}$ no appreciable improvement is obtained in terms of the RSS error. Further, we note that high values of yield stress deliver errors that are equal to those reported by the Elastic FEM method. These results show that tuning the yield stress parameter is essential for obtaining accurate results from the registration process.

The i-DIR method was also assessed in the analysis of medical CT images of the lung, where sliding is expected to occur when registering images from resting states to maximal inspiration effort (Amelon et al., 2014). When comparing resampled images, we showed that the i-DIR method delivered errors in registering the domains inside the lung that are comparable to those found in elastic DIR methods, see Figure 3.9. This conclusion is supported by the performance metrics RSS and TRE for the case of inside-lung landmarks reported in Table 3.3, where no marked differences are observed among the FFD, Elastic FEM and i-DIR methods. However, when assessing anatomical structures that are outside the lung, i.e. ribs, we observe that the i-DIR accurately resamples them to the correct location, whereas elastic DIR methods fail to achieve a reasonable result, see Figure 3.9,

bottom row. This observation is confirmed by the results obtained in the TRE when using rib landmarks, where the i-DIR delivers errors that are one order of magnitude smaller than the error provided by elastic DIR methods, see Table 3.3. Once again, we attribute the good performance of the i-DIR method to its ability to handle discontinuous sliding motion by considering inelastic deformations in those regions, a feature not displayed by elastic methods, see Figure 3.10. We note that none of the models perceives the sliding between the lobes. This shortcoming is partly due to the resolution of the meshes that cannot distinguish the thin boundaries of the lung lobes and the fact that part of this sliding mechanism is volumetric, which is ignored as it is a 2D analysis. This issue constitutes one of the main limitations of the current model, and it is one of the reasons why we emphasize the sliding between the lung and the ribs.

The evaluation of the elastic strain fields from registering lung CT images results in conclusions similar to those obtained in the case of the synthetic image: elastic DIR methods introduce highly oscillating fields both for the volumetric and deviatoric components of the elastic strain tensor, see Figure 3.11. We remark here that previous works on lung image registration have reported oscillatory strain fields when using elastic DIR methods that employ B-splines or other smooth and continuous basis functions for the construction of the deformation model (Cao et al., 2012; Hua et al., 2017). However, these oscillations have been shown to hinder the accuracy of the estimations of local pulmonary deformation, as they arise due to the inability of the deformation model to capture discontinuities in the displacement field (Hurtado, Villarroel, et al., 2016). Notably, the i-DIR method delivers a smooth distribution of elastic strain inside the lung domain, with a sharp decay outside that approaches a state of no deformation. Further, the spatial patterns of volumetric strain delivered by the i-DIR method are in good agreement with those reported in the literature for normal human lungs that have been analyzed by isolating the lung domain (Hurtado et al., 2017), where larger volumetric strains are observed in the dorsal (dependent) and basal regions of the lung.

In conclusion, we have introduced a novel inelastic model for DIR that automatically captures sliding without *a priori* knowledge or assumptions about the spatial location of discontinuities or the need of a segmentation to denote the slipping domain. We note that other DIR formulations have been proposed in the literature to handle motion discontinuities without the need of segmenting the sliding region before the analysis (Schmidt-Richberg et al., 2012) In order to do so, these methods consider some assumptions related to the specific physiological behavior of the organ. For the case of the lungs, slipping motion is restricted to the edges of the image, and slippage occurs along the edge of the image. We note that these assumptions are not required by the i-DIR method, and therefore it represents a truly automatic technique for the detection of discontinuities in DIR of arbitrary images. The key ingredient to achieve this performance is the introduction of an inelastic energy term, which automatically locates regions of high shearing deformation associated to sliding and locally modifies the effective mechanical properties, allowing for higher levels of shear deformation in localized domains. We remark that, while inelastic formulations are standard in the field of computational mechanics (Ortiz & Stainier, 1999), the inclusion of inelastic energy regularizers is novel in the field of image analysis, and, to the best of our knowledge, has not been pursued in the past in the field of DIR. For the application of lung images, it is worth mentioning that we aim at automatically capture sliding, particularly between the lung boundary and the ribs (clearly identified within the images), and not necessarily improve the registration accuracy inside the lung. The above is supported by the results obtained when measuring the RSS error, which demonstrates that our i-DIR model holds a comparable performance with traditional DIR methods, especially in areas with no sliding. However, the inelastic model is considerably superior in capturing slippage at the lung edges, which is again substantiated by a better performance when measuring the TRE using rib-landmarks.

The present work can be extended in several directions. One limitation of the current computer implementation of the i-DIR method is the large wall-clock time required to solve the optimization problem, which can take up to 40 times the time required by

optimized elastic DIR methods (see Appendix B.3). This limitation may be alleviated by implementations that leverage the power of GPUs in DIR libraries (Modat, Mcclelland, & Ourselin, 2010). In addition, due to the high computational demands, the current version of the i-DIR method has only been applied to 2D images. We remark that the motion and deformation analysis based on 2D images of the thorax constitutes an important limitation of this work in the biomechanical characterization of the lung. However, we also remark that under normal conditions, the dominant orientation of displacements in the lung is in the apico-basal direction (Amelon et al., 2011), which is included in the sagittal images considered in this study. Future extensions should focus on DIR implementations for 3D CT thoracic images, based on which a complete biomechanical study can be performed to fully understand the 3D nature of deformations in the lung. In addition, we note that due to the large level of strains experienced by the lung under full inspiration, the elastic energy component employed in the i-DIR formulation may not be suitable, as it corresponds to the elastic deformation energy for small strain levels (Lubliner, 2013). To overcome this limitation, hyperelastic warping formulations have been proposed which employ elastic energy terms that are compatible with large deformation (Genet, Stoeck, von Deuster, Lee, & Kozerke, 2018). The use of hyperelastic energy terms in the future versions of the i-DIR method constitutes a promising avenue of research.

4. CONCLUSIONS AND OUTLOOK

4.1. Conclusions

The use of continuum mechanics in conjunction with advanced medical imaging provides the necessary components to develop a quantitative framework for estimating regional deformations in lungs. In this regard, deformable registration models are useful to estimate transformation mapping fields which leads to the study of deformation mechanisms in lungs. The study of the mechanical behavior of the lung parenchyma is something that the scientific community is working on and where promising results have been obtained regarding the possibility of classifying healthy and diseased subjects. Various lung conditions and lung diseases manifests by a structural and mechanical alteration. Furthermore, the non-physiological levels of lung strain and stress that develop during mechanical ventilation commonly develop inflammation at the cellular level, resulting in tissue damage. Consequently, knowledge of lung biomechanics may be beneficial for the diagnosis of lung diseases and the development of safer strategies during ventilatory support therapies.

Chapter 2 describes an image-based biomechanical quantification model that measures regional deformation in normal human lungs. This work adds the concept of surface and length deformation to volumetric and anisotropy regional deformation. The results show spatial variations of regional volumetric deformation and distribution of regional volumetric deformation in supine human lungs that are consistent with the literature. This indicates greater deformation in the dorsal regions of the lung due to the effects of gravity. The normalized distribution of length and surface deformation are similar to the spatial pattern observed in the normalized Jacobian, suggesting a strong correlation with the direction of gravity. High values of anisotropy were shown in various regions of the lung without any spatial trend, confirming that the regional deformation of the lung is spatially heterogeneous. Since deformation energy in soft tissues not only depends on volumetric deformation, but also on surface and linear stretch, the confirmation that these additional

metrics are not uniform in the normal lung highlights the importance of assessing the 1st and 2nd invariants of the right stretch tensor and their relationship with disease onset and progression in futures studies.

During the study of regional deformation in the normal lung, we encountered an important limitation in the analyses performed. B-spline-based registration models that do not take into account the sliding kinematics of the organs, cannot accurately measure strain near the boundaries and fissures of lungs. For example, the intrinsic C^2- continuity established by the B-spline interpolation of the deformation mapping field observed in spline-based DIR models, results in a pointless effort when measuring discontinuities and material interface. As a result, non-physiological deformations arise near sliding surfaces within the lung. These deformations are characterized by regions with highly localized regional deformation near discontinuous surfaces where deformation is not expected to occur.

To address the problem of tissue sliding, Chapter 3 introduces a novel inelastic DIR model with the ability to automatically capture discontinuous boundaries in the context of regional lung deformation. An inelastic regularizer is introduced into the DIR model that automatically detects sliding surfaces by directly assessing the shear-induced deformation and modifying the elastic response in regions where high shearing occurs. Although inelastic formulations are widely used in the field of computational plasticity, the inclusion of an inelastic energy regularizer is a highly novel approach within the field of image analysis. The results show that the i-DIR model provides accurate estimates of local strain in the boundaries of the lung without spurious oscillatory patterns that are frequently observed in conventional elastic DIR methods without the need of defining the sliding surface before the analysis. However, the i-DIR model reveals various deficiencies in its applicability to a large-scale analysis of pulmonary deformations. The main limitation is the large number of degrees of freedom that the model holds, resulting in a high computational cost when solving the optimization problem. Consequently, the current i-DIR model is limited

and only supports 2D images. This restriction makes the characterization of regional lung deformation suboptimal since the volumetric nature of the deformation is neglected.

4.2. Future work

Extending the i-DIR model to support 3D images should produce a more comprehensive representation of regional lung deformation. This is a key aspect of lung biomechanical quantification since the deformation of the lung is known to be volumetric in nature. Future efforts should focus on developing a parallel implementation using GPUs and possibly migrating the source code to another language, such as native C/C++. Once the i-DIR supports the use of 3D images, the model should be applied and validated in the study of early disease biomarkers related to mechanical changes (deformation) of lung tissue. This study should consider healthy and diseased subjects to establish and identify differences in regional deformation within the lung. Considering sliding mechanisms inside the lung, a thorough description of regional deformation should include anisotropic indices, length, surface and volumetric deformation.

In many applications of mechanical engineering, the theory of infinitesimal deformations (small deformations) cannot be applied without introducing significant errors, especially in problems where the underlying deformation processes are described by large deformations, as in the case of lung deformations (Modersitzki, 2003). In the context of lung mechanics, additional improvement of the i-DIR model could focus on developing an inelastic model using a large deformation framework, such as a *finite strain elastoplastic* or *hyperelastic* model.

The clinical diagnosis of diseases can benefit in many ways from technological and computational advances. The integration of different medical image-based analysis methods is expected to help improve the clinical diagnosis of lung diseases. With the aim of causing synergies in the early detection of lung damage, it would be interesting to complement the information from image-based models of different nature. In this sense, once the

clinical validation of the i-DIR model has been carried out, the additional information that the pulmonary biomechanical analysis could offer might likely complement computational techniques focused on the extraction of biomarkers that indicate pulmonary abnormalities.

Complementary image-based techniques that may be valuable to the study of the state of lung tissue are focused on the extraction of biomarkers directly from the anatomical image. This feature extraction process, known as *Radiomics* or *Texture Image Analysis*, has great potential in terms of disease diagnosis and prognosis (Mao, 2010; Parekh & Jacobs, 2016). Quantification models based on statistical metrics attempt to study the distribution of intensities in the image (texture pattern analysis) or the morphology of previously segmented structures (shape-analysis). Conveniently, machine learning models are combined with feature extraction techniques to analyze the pixel information within the image in an entirely automatic procedure. The extraction of meaningful biomarkers is accomplished by systematically training large image datasets from healthy and diseased patients. In this context, Yang et al. work on the quantification and classification of pulmonary emphysema from chest tomography images. Their model consists of segmenting and quantifying emphysema and then training unsupervised models. Ultimately, the trained texture pattern model can classify the disease by defining emphysema subtypes. The automatic model can code standard emphysema subtypes, holding a significant correlation with clinical characteristics (Yang et al., 2017). In the same line of research, Wang and colleagues developed an artificial intelligence model based on convolutional neural networks (CNN) capable of classifying texture patterns in lung images. The model showed a notable classification performance (higher than 83%) to differentiate five types of tissue patterns: healthy, emphysema, ground glass, fibrosis, and micronodules (Wang et al., 2018). Expanding the research areas for the study of lung function, future work on the subject should aim to improve and validate automatic texture-based quantification models to detect particular anomalies inside predefined regions of interest and establish a strong correlation with mechanical changes inside the lung.

REFERENCES

Abidi, A. I., & Singh, S. (2020). *Deformable registration techniques for thoracic ct images* (1st ed.). Springer Singapore. doi: 10.1007/978-981-10-5837-0

Al-Mayah, A., Moseley, J., Velec, M., & Brock, K. K. (2009). Sliding characteristic and material compressibility of human lung: parametric study and verification. *Medical physics*, *36*, 4625–33. doi: 10.1118/1.3218761

Amelon, R. E., Cao, K., Ding, K., Christensen, G. E., Reinhardt, J. M., & Raghavan, M. L. (2011). Three-dimensional characterization of regional lung deformation. *Journal of Biomechanics*, *44*(13), 2489–2495.

Amelon, R. E., Cao, K., Reinhardt, J. M., Christensen, G. E., & Raghavan, M. (2012). Estimation of lung lobar sliding using image registration. In R. C. Molthen & J. B. Weaver (Eds.), *Medical imaging 2012: Biomedical applications in molecular, structural, and functional imaging* (Vol. 8317, pp. 416 – 423). SPIE. doi: 10.1117/12.911614

Amelon, R. E., Cao, K., Reinhardt, J. M., Christensen, G. E., & Raghavan, M. L. (2014). A measure for characterizing sliding on lung boundaries. *Annals of Biomedical Engineering*, *42*(3), 642–650. doi: 10.1007/s10439-013-0920-5

Ashburner, J. (2007). A fast diffeomorphic image registration algorithm. *NeuroImage*, *38*(1), 95 - 113.

Barnafi, N. A., Gatica, G. N., & Hurtado, D. E. (2018). Primal and Mixed Finite Element Methods for Deformable Image Registration Problems. *SIAM Journal on Imaging Sciences*, *11*(4), 2529–2567.

Bodduluri, S., Bhatt, S. P., Hoffman, E. A., Newell, J. D., Martinez, C. H., Dransfield, M. T., . . . COPDGene Investigators (2017). Biomechanical CT metrics are associated with patient outcomes in COPD. *Thorax*. Retrieved from http://www.ncbi.nlm.nih.gov/pubmed/28044005

Bodduluri, S., Newell, J. D. J., Hoffman, E. A., & Reinhardt, J. M. (2013). Registration-based lung mechanical analysis of chronic obstructive pulmonary disease (COPD) using a supervised machine learning framework. *Academic radiology*, *20*, 527–36. doi: 10.1016/j.acra.2013.01.019

Broit, C. (1981). *Optimal registration of deformed images* (Unpublished doctoral dissertation). Computer and Information Science, University of Pennsylvania.

Cao, K., Christensen, G., Ding, K., Du, K., Raghavan, M., Amelon, R., . . . Reinhardt, J. (2012, 10). Tracking regional tissue volume and function change in lung using image registration. *International journal of biomedical imaging*, *2012*, 956248. doi: 10.1155/2012/956248

Caselles, V., Kimmel, R., & Sapiro, G. (1997, 02). Geodesic active contours. *International Journal of Computer Vision*, *22*, 61-79. doi: 10.1023/A:1007979827043

Choi, S., Hoffman, E. A., Wenzel, S. E., Castro, M., Fain, S. B., Jarjour, N. N., . . . Lin, C.-l. (2015). Quantitative assessment of multiscale structural and functional alterations in asthmatic populations. *Applied Physiology*, *c*, 1286–1298. doi: 10.1152/japplphysiol.01094.2014

Choi, S., Hoffman, E. A., Wenzel, S. E., Castro, M., & Lin, C.-l. (2014). Improved CT-based estimate of pulmonary gas trapping accounting for scanner and lung-volume variations in a multicenter asthmatic study. *Applied Physiology*, *v*, 593–603. doi: 10.1152/japplphysiol.00280.2014

Choi, S., Hoffman, E. A., Wenzel, S. E., Tawhai, M. H., Yin, Y., Castro, M., & Lin, C.-l. (2013). Registration-based assessment of regional lung function via volumetric CT images of normal subjects vs . severe asthmatics. *Applied Physiology*, 730–742. doi: 10.1152/japplphysiol.00113.2013

Christensen, G., Rabbitt, R., & Miller, M. (1996, 02). Deformable template using large deformation kinematics. *IEEE Transactions on Image Processing*, *5*, 1435-47.

Christensen, G., Song, J. H., Lu, W., El Naqa, I., & Low, D. (2007, 07). Tracking lung tissue motion and expansion/compression with inverse consistent image registration and spirometry. *Medical physics*, *34*, 2155-63. doi: 10.1118/1.2731029

Computational geometry algorithms library. (2016). Retrieved from `http://www.cgal.org`

Cotes, J., Chinn, D., & Miller, M. (2006). *Lung function physiology, measurement and application in medicine* (6th ed.). Blackwell.

Cruces, P., Retamal, J., Hurtado, D. E., Erranz, B., Iturrieta, P., González, C., & Diaz, F. (2020). A physiological approach to understand the role of respiratory effort in the progression of lung injury in SARS-CoV-2 infection. *Critical Care*, *24*, 494.

Crum, W., Hartkens, T., & Hill, D. (2004). Non-rigid image registration: Theory and practice. *The British journal of radiology*, *77 Spec No 2*, S140-53. doi: 10.1259/bjr/25329214

Cruz Mena, E., & Moreno Bolton, R. (1999). *Aparato respiratorio fisiología y clínica* (4th ed.). Mediterraneo.

D'Angelo, E., Loring, S. H., Gioia, M. E., Pecchiari, M., & Moscheni, C. (2004). Friction and lubrication of pleural tissues. *Respiratory physiology & neurobiology*, *142*(1), 55-68. doi: 110.1016/j.resp.2004.05.006

Delmon, V., Rit, S., Pinho, R., & Sarrut, D. (2013). Registration of sliding objects using direction dependent B-splines decomposition. *Physics in Medicine and Biology*, 1303–1314.

De Souza Neto, E. A., Perić, D., & Owen, D. R. J. (2008). *Computational Methods for Plasticity: Theory and Applications*. Chichester, UK: John Wiley & Sons,.

Ding, K., Yin, Y., Cao, K., Christensen, G. E., Lin, C.-L., Hoffman, E. A., & Reinhardt, J. M. (2009). Evaluation of lobar biomechanics during respiration using image registration. In G.-Z. Yang, D. Hawkes, D. Rueckert, A. Noble, & C. Taylor (Eds.), *Medical image computing and computer-assisted intervention – miccai 2009* (pp. 739–746). Springer Berlin Heidelberg.

Dreyfuss, D., & Saumon, G. (1998). Ventilator-induced lung injury: lessons from experimental studies. *American journal of respiratory and critical care medicine*, *157*(1), 294–323.

Eskandari, M., Kuschner, W. G., & Kuhl, E. (2015). Patient-specific airway wall remodeling in chronic lung disease. *Annals of biomedical engineering*, *43*, 2538-51. doi: 10.1007/s10439-015-1306-7

Foskey, M., Davis, B., Goyal, L., Chang, S., Chaney, E., Strehl, N., ... Joshi, S. (2005). Large deformation 3D image registration in image-guided radiation therapy. *Physics in Medicine and Biology*, 5869–5892.

Freed, A. D., & Einstein, D. R. (2012). Hypo-elastic model for lung parenchyma. *Biomechanics and Modeling in Mechanobiology*, *11*, 557–573. doi: 10.1007/s10237-011-0333-z

Gattinoni, L., Caironi, P., Cressoni, M., Chiumello, D., Ranieri, V. M., Quintel, M., ... Bugedo, G. (2006). Lung recruitment in patients with the acute respiratory distress syndrome. *New England Journal of Medicine*, *354*(17), 1775-1786. doi: 10.1056/NEJMoa052052

Gattinoni, L., Carlesso, E., Cadringher, P., Valenza, F., Vagginelli, F., & Chiumello, D. (2003). Physical and biological triggers of ventilator-induced lung injury and its prevention. *The European Respiratory Journal*, *22*(47 suppl), 15s–25s. doi: 10.1183/09031936.03.00021303

Gattinoni, L., Pelosi, P., Suter, P. M., Pedoto, A., Vercesi, P., & Lissoni, A. (1998). Acute respiratory distress syndrome caused by pulmonary and extrapulmonary disease. Different syndromes? *American journal of respiratory and critical care medicine*, *158*, 3–11. doi: 10.1164/ajrccm.158.1.9708031

Genet, M., Stoeck, C. T., von Deuster, C., Lee, L. C., & Kozerke, S. (2018). Equilibrated warping: Finite element image registration with finite strain equilibrium gap regularization. *Medical Image Analysis*, *50*, 1–22.

Gering, D. T., Nabavi, A., Kikinis, R., Grimson, W. E. L., Hata, N., Everett, P., ... Wells, W. M. (1999). An integrated visualization system for surgical planning and guidance using image fusion and interventional imaging. *Proceedings of the International Conference on Image Computing and Computer-Assisted Intervention - MICCAI*, 809–819.

Hajnal, J., Hawkes, D., & Hill, D. (2001). *Medical image registration* (1st ed.). CRC Press.

Hobrack, S., Haberthür, D., Stampanoni, M., Schittny, J., & Wall, W. (2011, 05). Local strain distribution in real three-dimensional alveolar geometries. *Annals of biomedical engineering*, *39*, 2835-43. doi: 10.1007/s10439-011-0328-z

Hoppin, F. G., Lee, G. C., & Dawson, S. V. (1975). Properties of lung parenchyma in distortion. *Journal of Applied Physiology*, *39*(5), 742-751. doi: 10.1152/jappl.1975.39.5.742

Hua, R., Pozo, J. M., Taylor, Z. A., & Frangi, A. F. (2015). Discontinuous Non-rigid Registration using Extended Free-Form Deformations.. doi: 10.1117/12.2082597

Hua, R., Pozo, J. M., Taylor, Z. A., & Frangi, A. F. (2017). Multiresolution eXtended Free-Form Deformations (XFFD) for non-rigid registration with discontinuous transforms. *Medical Image Analysis*, *36*, 113–122. Retrieved from `http://dx.doi.org/10.1016/j.media.2016.10.008` doi: 10.1016/j.media.2016.10.008

Hurtado, D. E., Castro, S., & Gizzi, A. (2016). Computational modeling of non-linear diffusion in cardiac electrophysiology: A novel porous-medium approach. *Computer Methods in Applied Mechanics and Engineering*, *300*, 70 - 83. Retrieved from `http://www.sciencedirect.com/science/article/pii/S0045782515003679` doi: https://doi.org/10.1016/j.cma.2015.11.014

Hurtado, D. E., Erranz, B., Lillo, F., Sarabia-Vallejos, M., Iturrieta, P., Morales, F., … Cruces, P. (2020). Progression of regional lung strain and heterogeneity in lung injury: assessing the evolution under spontaneous breathing and mechanical ventilation. *Annals of Intensive Care*, *10*, 107.

Hurtado, D. E., & Henao, D. (2014, 05). Gradient flows and variational principles for cardiac electrophysiology: Toward efficient and robust numerical simulations of the electrical activity of the heart. *Computer Methods in Applied Mechanics and Engineering*, *273*. doi: 10.1016/j.cma.2014.02.002

Hurtado, D. E., & Ortiz, M. (2013). Finite element analysis of geometrically necessary dislocations in crystal plasticity. *International Journal for Numerical Methods in Engineering*, *93*, 66–79.

Hurtado, D. E., Villarroel, N., Andrade, C., Retamal, J., Bugedo, G., & Bruhn, A. (2017). Spatial patterns and frequency distributions of regional deformation in the healthy human lung. *Biomechanics and Modeling in Mechanobiology*, *16*, 1413–1423. doi: 10.1007/s10237-017-0895-5

Hurtado, D. E., Villarroel, N., Retamal, J., Bugedo, G., & Bruhn, A. (2016). Improving the accuracy of registration-based biomechanical analysis: A finite element approach to lung regional strain quantification. *IEEE Transactions on Medical Imaging*, *35*(2), 580–588. doi: 10.1109/TMI.2015.2483744

Jahani, N., Choi, S., Choi, J., Iyer, K., Hoffman, E. A., & Lin, C.-l. (2015). Assessment of regional ventilation and deformation using 4D-CT imaging for healthy human lungs during tidal breathing. *Applied Physiology*, 1064–1074. doi: 10.1152/japplphysiol.00339.2015

Jahani, N., Yin, Y., Hoffman, E. A., & Lin, C.-L. (2014). Assessment of regional non-linear tissue deformation and air volume change of human lungs via image registration. *Journal of Biomechanics*, *47*(7), 1626 - 1633. doi: https://doi.org/10.1016/j.jbiomech.2014.02.040

Kaczka, D. W., Cao, K., Christensen, G. E., Bates, J. H. T., & Simon, B. A. (2011). Analysis of regional mechanics in canine lung injury using forced oscillations and 3d image registration. *Annals of biomedical engineering*, *39*. doi: 10.1007/s10439-010-0214-0

Lai-Fook, S. J. (2004). Pleural mechanics and fluid exchange. *Physiological Reviews*, *84*(2), 385-410. doi: 10.1152/physrev.00026.2003

Lew, K. (2010). *The amazing human body - respiratory system*. Marshall Cavendish Benchmark.

Lu, W., Chen, M. L., Olivera H., G. H., Ruchala, K. J., & Mackie, T. R. (2004). Fast free-form deformable registration via calculus of variations. *Physics in Medicine*

and Biology, *49*(14), 3067–3087.

Lubliner, J. (2013). *Plasticity Theory*. Mineola, New York: Dover Publications.

Lynch, D., & Newell, J., Jr. (2009, 09). Quantitative imaging of copd. *Journal of thoracic imaging*, *24*, 189-94. doi: 10.1097/RTI.0b013e3181b31cf0

Maintz, J., & Viergever, M. A. (1998). A survey of medical image registration. *Medical Image Analysis*, *2*(1), 1 - 36. doi: https://doi.org/10.1016/S1361-8415(01)80026-8

Mallow, C., & Isakow, W. (2019, 04). Risk factors for loss of lung sliding in a medical intensive care population with acute respiratory failure. *Journal of Bronchology & Interventional Pulmonology*, *26*(2), 102–107. doi: 10.1097/lbr.0000000000000525

Mao, Y. (2010). *Biomedical imaging*. IntechOpen. Retrieved from `https://books.google.cl/books?id=GSqhDwAAQBAJ`

Mentzelopoulos, S. D., Roussos, C., & Zakynthinos, S. G. (2005). Prone position reduces lung stress and strain in severe acute respiratory distress syndrome. *The European Respiratory Journal*, *25*(3), 534-44.

Mercer, R. R., & Crapo, J. D. (1990). Spatial distribution of collagen and elastin fibers in the lungs. *Journal of Applied Physiology*, *69*(2), 756-765. doi: 10.1152/jappl.1990.69.2.756

Milic-Emili, J., Henderson, J. A., Dolovich, M. B., Trop, D., & Kaneko, K. (1966). Regional distribution of inspired gas in the lung. *Journal of Applied Physiology*, *21*(3), 749-759. doi: 10.1152/jappl.1966.21.3.749

Mitzner, W. (2011, 10). Mechanics of the lung in the 20th century. *Comprehensive Physiology*, *1*, 2009-27. doi: 10.1002/cphy.c100067

Modat, M., Mcclelland, J., & Ourselin, S. (2010). Lung registration using the NiftyReg package. In *Miccai2010 workshop: Medical image analysis for the clinic - a grand challenge 2010* (pp. 33–42).

Modat, M., Ridgway, G., Taylor, Z., Lehmann, M., Barnes, J., Hawkes, D., ... Ourselin, S. (2010, 10). Fast free-form deformation using graphics processing units. *Computer methods and programs in biomedicine*, *98*, 278-84. doi: 10.1016/j.cmpb.2009.09.002

Modersitzki, J. (2003). *Numerical methods for image registration* (1st ed.). Oxford University Press. doi: 10.1093/acprof:oso/9780198528418.001.0001

Office-For-National-Statistics. (2020, November). *Causes of death over 100 years.* Retrieved from `https://www.ons.gov.uk/peoplepopulationandcommunity/birthsdeathsandmarriages/deaths/articles/causesofdeathover100years/2017-09-18`

Ogden, R. (1984). *Non-Linear Elastic Deformations.* Mineola, NY: Dover Publications, Inc.

Oliveira, F. P., & Tavares, J. M. R. (2014). Medical image registration: a review. *Computer Methods in Biomechanics and Biomedical Engineering*, *17*(2), 73-93.

Ortiz, M., & Stainier, L. (1999). The variational formulation of viscoplastic constitutive updates. *Computer Methods in Applied Mechanics and Engineering*, *171*(3-4), 419–444.

Pace, D. F., Aylward, S. R., & Niethammer, M. (2013). A Locally Adaptive Regularization Based on Anisotropic Diffusion for Deformable Image Registration of Sliding Organs. *IEEE Transactions on Medical Imaging*, *32*(11), 2114–2126.

Parekh, V., & Jacobs, M. (2016, 03). Radiomics: A new application from established techniques. *Expert Review of Precision Medicine and Drug Development*, *1*, 207-226. doi: 10.1080/23808993.2016.1164013

Paula, L. F., Wellman, T. J., Winkler, T., Spieth, P. M., Güldner, A., Venegas, J. G., . . . Vidal Melo, M. F. (2016). Regional tidal lung strain in mechanically ventilated normal lungs. *Journal of Applied Physiology*, *121*(6), 1335-1347. doi: 10.1152/japplphysiol.00861.2015

Radovitzky, R., & Ortiz, M. (1999). Error estimation and adaptive meshing in strongly nonlinear dynamic problems. *Computer Methods in Applied Mechanics and Engineering*, *172*(1-4), 203–240.

Rausch, S., Martin, C., Bornemann, P., Uhlig, S., & Wall, W. (2011). Material model of lung parenchyma based on living precision-cut lung slice testing. *Journal of the Mechanical Behavior of Biomedical Materials*, *4*(4), 583 - 592. doi:

https://doi.org/10.1016/j.jmbbm.2011.01.006

Reinhardt, J. M., Ding, K., Cao, K., Christensen, G. E., Hoffman, E. A., & Bodas, S. V. (2008). Registration-based estimates of local lung tissue expansion compared to xenon CT measures of specific ventilation. *Medical image analysis*, *12*(6), 752–763. doi: 10.1016/j.media.2008.03.007

Retamal, J., Hurtado, D. E., Villarroel, N., Bruhn, A., Bugedo, G., Amato, M. B. P., . . . Borges, J. B. (2018a). Does Regional Lung Strain Correlate With Regional Inflammation in Acute Respiratory Distress Syndrome During Nonprotective Ventilation? An Experimental Porcine Study*. *Critical Care Medicine*, *46*, e591-e599. doi: 10.1097/CCM.0000000000003072

Retamal, J., Hurtado, D. E., Villarroel, N., Bruhn, A., Bugedo, G., Amato, M. B. P., . . . Borges, J. B. (2018b). Does regional lung strain correlate with regional inflammation in acute respiratory distress syndrome during nonprotective ventilation? an experimental porcine study. *Critical Care Medicine*, *46*(6).

Roan, E., & Waters, C. M. (2011). What do we know about mechanical strain in lung alveoli? *American journal of physiology. Lung cellular and molecular physiology*, *301*, L625-35. doi: 10.1152/ajplung.00105.2011

Rodarte, R. D., J. R.and Hubmayr, Stamenovic, D., & Walters, B. J. (1985). Regional lung strain in dogs during deflation from total lung capacity. *Applied physiology*, *58*(1), 164-172. doi: 10.1152/jappl.1985.58.1.164

Rogers, K. (2011). *The human body. the respiratory system* (1st ed.). Britannica.

Rueckert, D., & Schnabel, J. A. (2011). Medical Image Registration. In T. M. Deserno (Ed.), *Biomedical image processing* (pp. 131–154). Springer-Verlag Berlin Heidelberg.

Rueckert, D., Sonoda, L. I., Hayes, C., Hill, D. L., Leach, M. O., & Hawkes, D. J. (1999). Nonrigid registration using free-form deformations: application to breast MR images. *IEEE Transactions on Medical Imaging*, *18*(8), 712–21.

Schmidt-Richberg, A. (2014). *Registration methods for pulmonary image analysis* (1st ed.). Springer Vieweg. doi: 10.1007/978-3-658-01662-3

Schmidt-Richberg, A., Werner, R., Handels, H., & Ehrhardt, J. (2012). Estimation of slipping organ motion by registration with direction-dependent regularization. *Medical Image Analysis*, *16*(1), 150–159.

Sotelo, J., Urbina, J., Valverde, I., Tejos, C., Irarrazaval, P., Andia, M., . . . Hurtado, D. (2016). 3d quantification of wall shear stress and oscillatory shear index using a finite-element method in 3d cine pc-mri data of the thoracic aorta. *IEEE Transactions on Medical Imaging*, *35*(6), 1475-1487. doi: 10.1109/TMI.2016.2517406

Sotelo, J., Urbina, J., Valverde, I., Tejos, C., Irarrazaval, P., Uribe, S., & Hurtado, D. (2015). Quantification of wall shear stress using a finite-element method in multi-dimensional phase-contrast mr data of the thoracic aorta. *Journal of Biomechanics*, *48*(10), 1817 - 1827. doi: https://doi.org/10.1016/j.jbiomech.2015.04.038

Sotiras, A., Davatzikos, C., & Paragios, N. (2013a). Deformable medical image registration: A survey. *IEEE Transactions on Medical Imaging*, *32*(7), 1153-1190. doi: 10.1109/TMI.2013.2265603

Sotiras, A., Davatzikos, C., & Paragios, N. (2013b). Deformable medical image registration: A survey. *IEEE Transactions on Medical Imaging*, *32*(7), 1153–1190.

Spaggiari, E., Zompatori, M., Verduri, A., Chetta, A., Bnà, C., Ormitti, F., . . . Rabaiotti, E. (2005, 01). Early smoking-induced lung lesions in asymptomatic subjects. correlations between high resolution dynamic ct and pulmonary function testing. *La Radiologia medica*, *109*, 27-39.

Thirion, J.-P. (1998). Image matching as a diffusion process: an analogy with maxwell's demons. *Medical Image Analysis*, *2*(3), 243 - 260.

Truesdell, C., & Noll, W. (1965). *The nonlinear field theories of mechanics.* Springer-Verlag Berlin Heidelberg.

Valenza, F., Guglielmi, M., Maffioletti, M., Tedesco, C., Maccagni, P., Fossali, T., . . . Gattinoni, L. (2005, February). Prone position delays the progression of ventilator-induced lung injury in rats: Does lung strain distribution play a role? *Critical Care Medicine*, *33*(2), 361–367. doi: 10.1097/01.CCM.0000150660.45376.7C

Viergever, M. A., Maintz, J. A., Klein, S., Murphy, K., Staring, M., & Pluim, J. P. (2016). A survey of medical image registration – under review. *Medical Image Analysis*, *33*, 140 - 144. doi: https://doi.org/10.1016/j.media.2016.06.030

Vlahakis, N. E., Schroeder, M. A., Limper, A. H., & Hubmayr, R. D. (1999). Stretch induces cytokine release by alveolar epithelial cells in vitro. *The American journal of physiology*, *277*(1), L167–73.

von Siebenthal, M., Székely, G., Gamper, U., Boesiger, P., Lomax, A., & Cattin, P. (2007). 4d mr imaging of respiratory organ motion and its variability. *Physics in Medicine and Biology*, *52*, 1547-1564.

Wang, Q., Zheng, Y., Yang, G., Jin, W., Chen, X., & Yin, Y. (2018). Multi-scale rotation-invariant convolutional neural networks for lung texture classification. *IEEE Journal of Biomedical and Health Informatics*, *22*(1), 184-195. doi: 10.1109/JBHI.2017.2685586

Ward, J. P. (2010). *The respiratory system at a glace* (3rd ed.). Wiley-Blackwell.

Wellman, T., Winkler, T., Costa, E., Musch, G., Harris, R., Zheng, H., . . . Melo, M. (2014). Effect of local tidal lung strain on inflammation in normal and lipopolysaccharide-exposed sheep. *Critical care medicine*, *42*. doi: 10.1097/CCM.0000000000000346

Wells, W. M., Viola, P., Atsumi, H., Nakajima, S., & Kikinis, R. (1996). Multi-modal volume registration by maximization of mutual information. *Medical Image Analysis*, *1*(1), 35–51.

West, J. B. (2012). *Respiratory physiology the essentials* (9th ed.). Lippincott Williams & Wilkins.

West, J. B. (2013). *Pulmonary pathophysiology the essentials* (8th ed.). Lippincott Williams & Wilkins.

Whittemore, S. (2004). *The respiratory system*. Chelsea House.

World-Health-Organization. (2020, November). *The top 10 causes of death.* Retrieved from `https://www.who.int/news-room/fact-sheets/detail/the-top-10-causes-of-death`

Wu, Z., Rietzel, E., Boldea, V., Sarrut, D., & Sharp, G. C. (2008). Evaluation of deformable registration of patient lung 4DCT with subanatomical region segmentations. *Medical Physics*, 775–781.

Yang, J., Angelini, E., Balte, P., Hoffman, E., Austin, J., Smith, B., . . . Laine, A. (2017, 09). Unsupervised discovery of spatially-informed lung texture patterns for pulmonary emphysema: The mesa copd study. In (Vol. 10433, p. 116-124). doi: 10.1007/978-3-319-66182-7_14

Yin, Y., Hoffman, E. A., & Lin, C.-L. (2010). Lung lobar slippage assessed with the aid of image registration. In T. Jiang, N. Navab, J. P. W. Pluim, & M. A. Viergever (Eds.), *Medical image computing and computer-assisted intervention – miccai 2010* (pp. 578–585). Berlin, Heidelberg: Springer Berlin Heidelberg.

Yushkevich, P. A., Piven, J., Hazlett, H. C., Smith, R. G., Ho, S., Gee, J. C., & Gerig, G. (2006). User-guided 3d active contour segmentation of anatomical structures: Significantly improved efficiency and reliability. *NeuroImage*, *31*(3), 1116 - 1128. doi: https://doi.org/10.1016/j.neuroimage.2006.01.015

APPENDIX

A. FIRST APPENDIX

A.1. Registration parameters

As described in (Modat, Mcclelland, & Ourselin, 2010), the entire image registration process included four sequential stages: one global registration and three local registrations. All parameters used in each of the stages is described below.

1st step: **Global registration**.

An affine transformation based on a block matching algorithm is used for an initial global registration. The size of the block was set to 4^3 voxels and the neighbourhood area of a block has been defined such that the block in the reference image and the block in the floating image always overlap by at least one voxel. A cross-correlation metric is used, as a similarity measure.

2nd step: **First local registration**.

First local registration stage considers only 2 registration levels of a 4-level pyramidal approach. In other words, warping was performed on 3-time and twice downsampled images. The control point spacing has been set to 6 voxel-width. The maximal number of iterations per level was set to 500 and the weight of the bending-energy penalty term to 0.01%. After computation of the NMI gradient, it is smoothed using a Gaussian kernel with standard deviation set to half the control point spacing size (3 voxels width). No penalty term based on the Jacobian determinant has been used for this stage. The aim of the initial local registration was to quickly register the main structures in the lung.

Table A.1. Parameters for first local registration.

Parameter	Value
"-maxit"	"500"
"-ln"	"4"
"-lp"	"2"
"-smoothGrad"	"3"
"-be"	"0.0001"
"-sx"	"-6"
"-sy"	"-6"
"-sz"	"-6"

3rd step: **Second local registration**.

The second local registration stage was performed on twice down-sampled input images. The NMI gradient is still smoothed with the same kernel size, the bending-energy weight is set the 0.1% and the Jacobian-based penalty term is introduced with the same weight. The maximal number of iteration is set to 500. The aim of this stage was to quickly align the border of the lung.

Table A.2. Parameters for second local registration.

Parameter	Value
"-maxit"	"500"
"-ln"	"3"
"-lp"	"1"
"-smoothGrad"	"3"
"-be"	"0.001"
"-jl"	"0.001"
"-sx"	"-6"
"-sy"	"-6"
"-sz"	"-6"

4th step: **Third local registration**.

This last stage was performed using three levels in the pyramidal approach: 3-time, twice and once down-sampled images. The penalty term weights were both set to 0.1% and no smoothing was performed on the NMI gradient field. The maximal number of iterations was set to 300 for each of the three levels. The goal of the final stage was to established a detailed alignment of the entire lung.

Table A.3. Parameters for third local registration.

Parameter	Value
"-maxit"	"300"
"-ln"	"4"
"-lp"	"3"
"-be"	"0.001"
"-jl"	"0.001"
"-sx"	"-6"
"-sy"	"-6"
"-sz"	"-6"

A.2. Supplementary Material 1

Supplementary Material 1: Invariant + SRI + ADI maps for all subjects
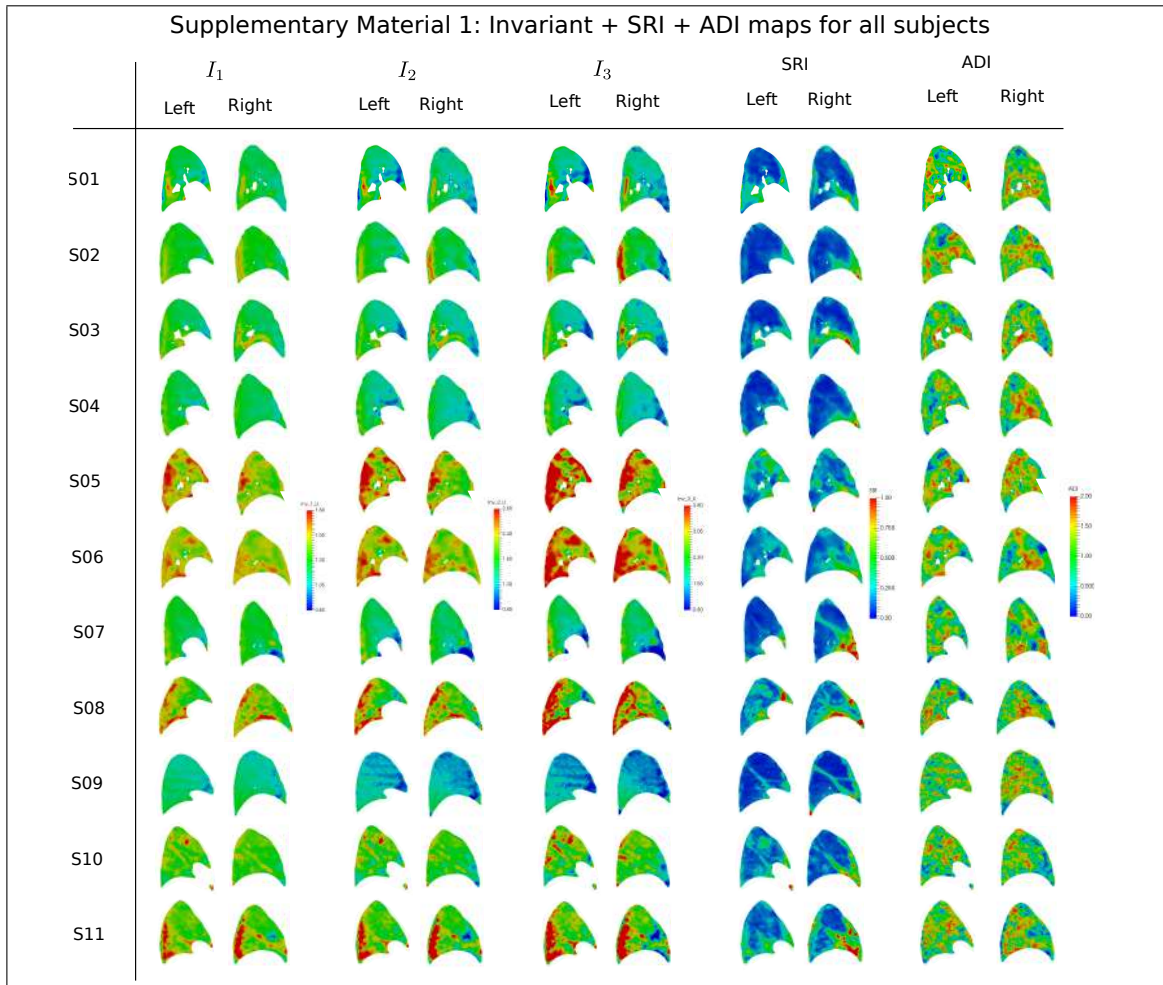
A.3. Supplementary Material 2

Table A.4. Statistical measures for the left lung (LL) and right lung (RL) distributions of I_1

Subject	Mean		Std		Kurt.		Skew.	
	LL	RL	LL	RL	LL	RL	LL	RL
S01	1.249	1.236	0.135	0.117	0.717	1.972	0.738	0.933
S02	1.303	1.319	0.093	0.107	0.940	1.065	0.731	0.543
S03	1.273	1.286	0.114	0.142	0.885	0.219	0.579	0.723
S04	1.245	1.218	0.092	0.068	1.537	1.272	0.568	0.536
S05	1.552	1.491	0.122	0.122	0.763	0.487	0.422	0.203
S06	1.502	1.498	0.097	0.099	1.200	0.939	-0.057	0.176
S07	1.260	1.253	0.098	0.096	1.896	2.045	0.408	0.368
S08	1.460	1.466	0.165	0.154	0.046	1.904	-0.042	0.428
S09	1.140	1.136	0.073	0.079	1.433	2.171	0.346	0.681
S10	1.376	1.362	0.112	0.101	0.522	1.136	0.216	-0.040
S11	1.460	1.445	0.171	0.184	0.961	1.209	0.869	0.704

Table A.5. Statistical measures for the left lung (LL) and right lung (RL) distributions of I_2

| Subject	Mean		Std		Kurt.		Skew.	
	LL	RL	LL	RL	LL	RL	LL	RL
S01	1.538	1.503	0.334	0.291	1.425	3.425	0.978	1.240
S02	1.681	1.710	0.249	0.294	1.331	1.382	0.822	0.637
S03	1.593	1.609	0.290	0.359	1.861	0.901	0.821	0.902
S04	1.535	1.463	0.223	0.171	1.816	1.630	0.680	0.589
S05	2.338	2.171	0.371	0.360	0.864	0.661	0.503	0.326
S06	2.218	2.189	0.283	0.294	0.992	0.991	-0.026	0.258
S07	1.577	1.531	0.249	0.233	2.083	1.738	0.681	0.184
S08	2.079	2.068	0.474	0.414	0.313	0.651	0.191	0.227
S09	1.291	1.274	0.166	0.180	1.942	3.094	0.494	0.874
S10	1.862	1.817	0.305	0.276	0.738	1.043	0.393	0.089
S11	2.085	2.021	0.511	0.549	1.959	2.489	1.154	1.130

Table A.6. Log-normal fit: location and scale parameters, and fit error for I_1

Subject	$\hat{\mu}$		$\hat{\sigma}$		Error (%)	
	LL	RL	LL	RL	LL	RL
S01	0.217	0.208	0.106	0.092	10.1	14.7
S02	0.262	0.273	0.070	0.080	10.2	11.2
S03	0.237	0.245	0.089	0.107	13.9	14.8
S04	0.216	0.196	0.073	0.055	16.0	18.1
S05	0.436	0.396	0.078	0.082	14.1	18.0
S06	0.405	0.402	0.065	0.066	15.4	14.5
S07	0.228	0.223	0.077	0.076	24.6	20.3
S08	0.372	0.377	0.115	0.105	18.0	10.3
S09	0.129	0.125	0.063	0.068	9.1	12.1
S10	0.316	0.306	0.081	0.075	7.4	12.4
S11	0.372	0.360	0.114	0.125	20.1	17.7
				Average	14.4	14.9

Table A.7. Log-normal fit: location and scale parameters, and fit error for I_2

Subject	$\hat{\mu}$		$\hat{\sigma}$		Error (%)	
	LL	RL	LL	RL	LL	RL
S01	0.408	0.390	0.209	0.184	9.4	13.2
S02	0.509	0.522	0.144	0.171	9.9	14.6
S03	0.450	0.452	0.178	0.214	12.2	13.5
S04	0.418	0.374	0.143	0.115	14.7	14.9
S05	0.837	0.761	0.158	0.168	15.3	18.9
S06	0.788	0.774	0.132	0.136	18.7	16.8
S07	0.443	0.414	0.158	0.157	25.8	24.4
S08	0.704	0.705	0.239	0.208	18.0	13.1
S09	0.247	0.233	0.128	0.138	11.0	14.0
S10	0.608	0.585	0.165	0.157	8.3	16.1
S11	0.707	0.669	0.232	0.263	17.9	19.2
				Average	14.7	16.2

A.4. Supplementary Material 3

Supplementary Material 3: Normalized invariant maps for all subjects
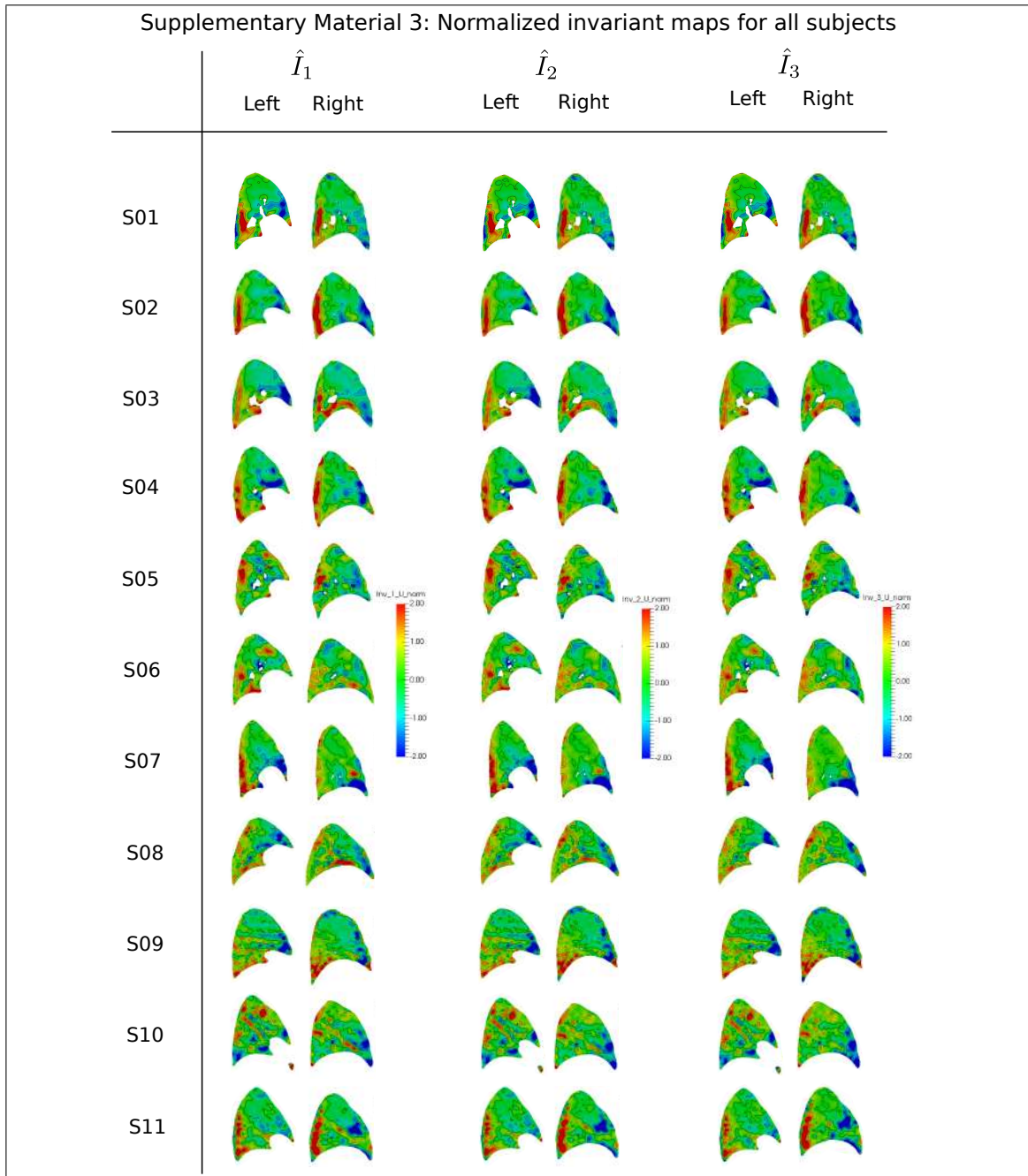
A.5. Supplementary Material 4
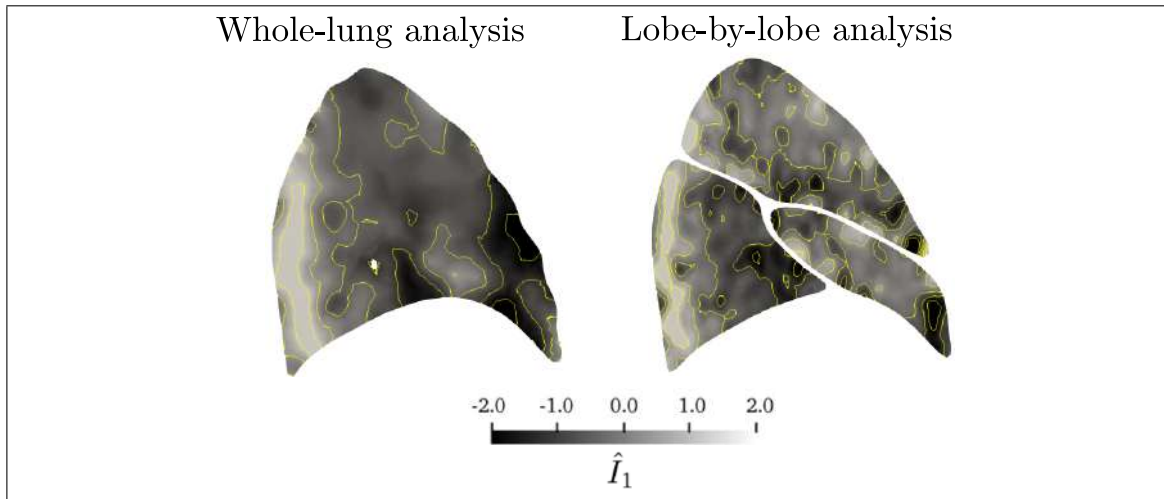
Figure A.1. Side by side between the whole-lung analysis and lobe-by-lobe analysis in terms of $\hat{I}_1$.

B. SECOND APPENDIX

B.1. Mathematical definitions and demonstrations

B.1.1. Relation between the rate of plastic strain and the internal variables.

In general, the relationship between $\dot{\varepsilon}^p$ and q is not independent and is given by the *Prandtl-Reuss* flow rule:

$$\dot{\varepsilon}_{ij}^p = \dot{\bar{\varepsilon}}^p \left(\frac{3}{2} \frac{s_{ij}}{\bar{\sigma}} \right) \tag{B.1}$$

where $\dot{\bar{\varepsilon}}^p$ stands for the evolution of the accumulated plastic strain and $\bar{\sigma}$ for the effective stress, which for the von Mises model takes the form

$$\bar{\sigma} = \sqrt{\frac{3}{2} s_{ij} s_{ij}}. \tag{B.2}$$

For multi-axial plasticity we can rewrite the flow rule (3.20) as,

$$\dot{\varepsilon}_{ij}^p = \dot{\bar{\varepsilon}}^p M_{ij} \tag{B.3}$$

where $\boldsymbol{M} \equiv M_{ij} = \frac{3}{2} \frac{s_{ij}}{\bar{\sigma}}$ stands for the instantaneous direction of plastic flow. Similarly, the effective stress (B.2) can be expressed as

$$\bar{\sigma} = \sigma_{ij} M_{ij}. \tag{B.4}$$

Going a step back and clearing $\dot{\bar{\varepsilon}}^p$ from (B.1) we have,

$$\dot{\bar{\varepsilon}}^p = \sqrt{\frac{2}{3} \dot{\varepsilon}_{ij}^p \dot{\varepsilon}_{ij}^p} \tag{B.5}$$

which in view of the plastic flow rule, is analogous to

$$\dot{\bar{\varepsilon}}^p = \dot{q} \tag{B.6}$$

Then by integration of (B.5) and again, assuming isotropic hardening, we have the following relation,

$$\bar{\varepsilon}^p = \int_0^t \sqrt{\frac{2}{3} \dot{\varepsilon}_{ij}^p \dot{\varepsilon}_{ij}^p} \, dt \equiv q \tag{B.7}$$

Finally, we compute the driving forces for q as,

$$y = -\frac{\partial \boldsymbol{A}}{\partial q} = \frac{\partial W^e}{\partial \varepsilon_{ij}^e} M_{ij} - \frac{\partial W^p}{\partial q}(q) = \sigma_{ij} M_{ij} - \frac{\partial W^p}{\partial q}(q) \tag{B.8}$$

$$y = \bar{\sigma} - \sigma_c. \tag{B.9}$$

B.1.2. Incremental flow rule update

Following an incremental flow rule of the type,

$$\varepsilon_{n+1}^p = \varepsilon_n^p + \Delta q \boldsymbol{M} \tag{B.10}$$

$$= \varepsilon_n^p + \Delta q \frac{3}{2} \frac{\boldsymbol{s}_{n+1}}{\bar{\sigma}_{n+1}} \tag{B.11}$$

let

$$g_n(\boldsymbol{\varepsilon}_{n+1}, q_{n+1}) = \boldsymbol{A}\big(\boldsymbol{\varepsilon}_{n+1}, \varepsilon_{n+1}^p(q_{n+1}), q_{n+1}\big) - \boldsymbol{A}_n + \Delta t \cdot \psi^* \left(\frac{|q_{n+1} - q_n|}{\Delta t} \right) \tag{B.12}$$

Then we seek to minimize (B.12) with respect to q_{n+1}, such that,

$$\frac{\partial g_n}{\partial q_{n+1}} = 0 \qquad \Longrightarrow \qquad \inf_{q_{n+1}} g_n(\boldsymbol{\varepsilon}_{n+1}, q_{n+1}) \tag{B.13}$$

we solve the above in a sub-differential way, such that

$$0 \in \frac{\partial \boldsymbol{A}}{\partial q_{n+1}} + \partial \psi^* \left(\frac{|q_{n+1} - q_n|}{\Delta t} \right) \tag{B.14}$$

$$0 \in \frac{\partial W^e}{\partial \boldsymbol{\varepsilon}^e_{n+1}} \cdot \frac{\partial \boldsymbol{\varepsilon}^e_{n+1}}{\partial q_{n+1}} (\boldsymbol{\varepsilon}_{n+1} - \boldsymbol{\varepsilon}^p_n - (q_{n+1} - q_n)\boldsymbol{M}) + \frac{\partial W^p}{\partial q}(q_{n+1}) + \partial \psi^* \left(\frac{|q_{n+1} - q_n|}{\Delta t} \right) \tag{B.15}$$

$$0 \in -\boldsymbol{\sigma}_{n+1} \cdot \boldsymbol{M} + \frac{\partial W^p}{\partial q}(q_n + \Delta q) + \partial \psi^* \left(\frac{|\Delta q|}{\Delta t} \right) \tag{B.16}$$

$$0 \in -\bar{\sigma}_{n+1} + \frac{\partial W^p}{\partial q}(q_n + \Delta q) + \partial \psi^* \left(\frac{|\Delta q|}{\Delta t} \right) \tag{B.17}$$

Recalling that the von Mises flow vector is purely deviatoric (De Souza Neto et al., 2008), we have that

$$\boldsymbol{s}_{n+1} = 2\mu \boldsymbol{\varepsilon}^e_{n+1}$$

$$= 2\mu (\boldsymbol{\varepsilon}_{n+1} - \boldsymbol{\varepsilon}^p_{n+1})$$

$$= 2\mu \left(\boldsymbol{\varepsilon}_{n+1} - \boldsymbol{\varepsilon}^p_n - \Delta q \frac{3}{2} \frac{\boldsymbol{s}_{n+1}}{\bar{\sigma}_{n+1}} \right)$$

$$= 2\mu (\boldsymbol{\varepsilon}_{n+1} - \boldsymbol{\varepsilon}^p_n) - 2\mu \Delta q \frac{3}{2} \frac{\boldsymbol{s}_{n+1}}{\bar{\sigma}_{n+1}}$$

$$\boldsymbol{s}_{n+1} = \boldsymbol{s}^{pre}_{n+1} - 3\mu \Delta q \frac{\boldsymbol{s}_{n+1}}{\bar{\sigma}_{n+1}} \tag{B.18}$$

Since the predictive and updated deviatoric stress are co-linear ($\boldsymbol{s}_{n+1} \parallel \boldsymbol{s}^{pre}_{n+1}$), we can state that,

$$\boldsymbol{M} = \frac{3}{2} \frac{\boldsymbol{s}_{n+1}}{\bar{\sigma}_{n+1}} = \frac{3}{2} \frac{\boldsymbol{s}^{pre}_{n+1}}{\bar{\sigma}^{pre}_{n+1}} \tag{B.19}$$

$$\implies \boldsymbol{s}_{n+1} = \frac{\boldsymbol{s}^{pre}_{n+1}}{\bar{\sigma}^{pre}_{n+1}} \bar{\sigma}_{n+1} \tag{B.20}$$

From the above we can re-write (B.18) as,

$$\boldsymbol{s}_{n+1} = \boldsymbol{s}^{pre}_{n+1} - 3\mu\Delta q \frac{\boldsymbol{s}^{pre}_{n+1}}{\bar{\sigma}^{pre}_{n+1}} \tag{B.21}$$

$$\boldsymbol{s}_{n+1} = \left(1 - \frac{3\mu\Delta q}{\bar{\sigma}^{pre}_{n+1}}\right) \boldsymbol{s}^{pre}_{n+1} \tag{B.22}$$

Now replacing (B.20) in (B.22), we have,

$$\frac{\boldsymbol{s}^{pre}_{n+1}}{\bar{\sigma}^{pre}_{n+1}} \bar{\sigma}_{n+1} = \left(1 - \frac{3\mu\Delta q}{\bar{\sigma}^{pre}_{n+1}}\right) \boldsymbol{s}^{pre}_{n+1} \tag{B.23}$$

$$\implies \bar{\sigma}_{n+1} = \bar{\sigma}^{pre}_{n+1} - 3\mu\Delta q \tag{B.24}$$

Going a step back to (B.17) we can explicitly define,

$$\bar{\sigma}^{pre}_{n+1} - 3\mu\Delta q \in \frac{\partial W^p}{\partial q}(q_n + \Delta q) + \partial\psi^*\left(\frac{|\Delta q|}{\Delta t}\right) \tag{B.25}$$

Finally, assuming that $W^p = \frac{1}{2}Hq^2_{n+1}$ and $\psi^* = \sigma_y|\Delta q|$, we can rewrite (B.25) as:

$$\bar{\sigma}^{pre}_{n+1} - 3\mu\Delta q - H(q_n + \Delta q) - \sigma_y = 0 \tag{B.26}$$

which eventually delivers,

$$\Delta q = \frac{\bar{\sigma}^{pre}_{n+1} - Hq_n - \sigma_y}{3\mu + H} \tag{B.27}$$

B.1.3. Return mapping algorithm

The solution of Δq in (B.27) involves a two mutually exclusive steps:

i) An elastic predictor, such that,

$$
\begin{aligned}
\Delta q &= 0 \\
q_{n+1}^{pre} &= q_n \\
\bar{\sigma}_{n+1}^{pre} &= \{2\mu(\varepsilon_{n+1} - \varepsilon_{n+1}^p(q_{n+1}^{pre})) + \lambda \operatorname{trace}(\varepsilon_{n+1} - \varepsilon_{n+1}^p(q_{n+1}^{pre}))\boldsymbol{I}\} \cdot \boldsymbol{M} \\
&= \sqrt{\tfrac{3}{2} \boldsymbol{s}_{n+1}^{pre} \cdot \boldsymbol{s}_{n+1}^{pre}}
\end{aligned}
\tag{B.28}
$$

replacing in (B.26), we have

$$
\bar{\sigma}_{n+1}^{pre} - Hq_n - [-\sigma_y, \sigma_y] = 0
\tag{B.29}
$$

$$
\implies \begin{cases}
\bar{\sigma}_{n+1}^{pre} \leq Hq_n + \sigma_y \\
\bar{\sigma}_{n+1}^{pre} \geq -Hq_n - \sigma_y
\end{cases}
\tag{B.30}
$$

and

ii) A plastic corrector, where we have two possible cases:

a) if the elastic trial lies within the elastic domain

$$
\Phi(\bar{\sigma}_{n+1}^{pre}) \leq 0 \qquad \implies \qquad \bar{\sigma}_{n+1}^{pre} \in [-\sigma_y, \sigma_y]
\tag{B.31}
$$

there is no plastic evolution within the time interval (t_n, t_{n+1}), and therefore we update our variables:

$$
(\cdot)_{n+1} = (\cdot)_{n+1}^{pre}
\tag{B.32}
$$

and

b) otherwise, we have plastic flow (or elasto-plastic evolution). By a traditional Newton-Raphson linearization we solve the following

$$
\bar{\sigma}_{n+1}^{pre} - 3\mu\Delta q - H(q_n + \Delta q) - \sigma_y = 0
\tag{B.33}
$$

and then we update the following variables at t_{n+1},

$$\varepsilon^p_{n+1} = \varepsilon^p_n + \Delta q \frac{3}{2} \frac{s_{n+1}}{\bar{\sigma}_{n+1}} \tag{B.34}$$

$$q_{n+1} = q_n + \Delta q \tag{B.35}$$

$$\varepsilon^e_{n+1} = \varepsilon_{n+1} - \varepsilon^p_{n+1} \tag{B.36}$$

$$\boldsymbol{\sigma}_{n+1} = \lambda \operatorname{trace}(\varepsilon^e_{n+1})\boldsymbol{I} + 2\mu\varepsilon^e_{n+1} \tag{B.37}$$

$$\mathbf{D}^{ep}_{n+1} = 2\mu \left(1 - \frac{3\mu\Delta q}{\bar{\sigma}^{pre}_{n+1}} \right) \mathbf{I}_d + 6\mu^2 \left(\frac{\Delta q}{\bar{\sigma}^{pre}_{n+1}} - \frac{1}{3\mu + H} \right) \bar{\boldsymbol{M}}_{n+1} \otimes \bar{\boldsymbol{M}}_{n+1} + K\boldsymbol{I} \otimes \boldsymbol{I} \tag{B.38}$$

where K is the bulk modulus, $\bar{\boldsymbol{M}}_{n+1} \equiv \sqrt{\frac{2}{3}}\boldsymbol{M}_{n+1} = \frac{\boldsymbol{s}^{pre}_{n+1}}{\|\boldsymbol{s}^{pre}_{n+1}\|}$ is the unit plastic flow vector and $\mathbf{I}_d$ is the fourth order deviatoric projection tensor defined as,

$$\mathbf{I}_d \equiv \mathbf{I}_S - \frac{1}{3}\boldsymbol{I} \otimes \boldsymbol{I} \tag{B.39}$$

with $\mathbf{I}_S = \frac{1}{2}(\delta_{ik}\delta_{jl} + \delta_{il}\delta_{jk})$ as the fourth order symmetric identity tensor.

B.1.4. Effective incremental energy

The **effective** incremental energy can be defined as follows,

$$W_n(\varepsilon) = \inf_{q_{n+1}} g_n(\varepsilon, q_{n+1}) = g_n(\varepsilon, q^*_{n+1}(\varepsilon)) \tag{B.40}$$

where,

$$q^*_{n+1}(\varepsilon) \in \operatorname{argmin} g_n(\varepsilon, q_{n+1}) \tag{B.41}$$

such that,

$$\frac{\partial g_n}{\partial q_{n+1}}(\varepsilon, q^*_{n+1}(\varepsilon)) = 0 \tag{B.42}$$

Conveniently know the effective potential depends solely in $\varepsilon = \varepsilon_{n+1}$. Following this definition, we compute the first and second derivative of W_n, where,

$$\mathrm{D}W_n(\varepsilon) = \frac{\partial g_n}{\partial \varepsilon}(\varepsilon, q_{n+1}^*(\varepsilon)) \tag{B.43}$$

$$= \frac{\partial g_n}{\partial \varepsilon}(\varepsilon, q_{n+1}^*(\varepsilon)) + \frac{\partial g_n}{\partial q_{n+1}}(\varepsilon, q_{n+1}^*(\varepsilon)) \cdot \frac{\partial q_{n+1}^*}{\partial \varepsilon}(\varepsilon) \tag{B.44}$$

but since $\frac{\partial g_n}{\partial q_{n+1}}(\varepsilon, q_{n+1}^*(\varepsilon)) = 0$, we have that for a fully implicit scheme,

$$\mathrm{D}W_n(\varepsilon) = \frac{\partial g_n}{\partial \varepsilon}(\varepsilon, q_{n+1}^*(\varepsilon)) \equiv \boldsymbol{\sigma}_{n+1} \tag{B.45}$$

where $\boldsymbol{\sigma}_{n+1}$ are the stresses at $t = t_{n+1}$.

Then we compute,

$$\mathrm{D}^2 W_n(\varepsilon) = \frac{\partial^2 g_n}{\partial \varepsilon \partial \varepsilon}(\varepsilon, q_{n+1}^*(\varepsilon)) + \frac{\partial^2 g_n}{\partial \varepsilon \partial q_{n+1}}(\varepsilon, q_{n+1}^*(\varepsilon)) \cdot \frac{\partial q_{n+1}^*}{\partial \varepsilon}(\varepsilon) \tag{B.46}$$

where we can redefine $\frac{\partial q_{n+1}^*}{\partial \varepsilon}(\varepsilon)$ deriving (B.42) by $\frac{\partial}{\partial \varepsilon}$, such that,

$$\frac{\partial^2 g_n}{\partial q_{n+1} \partial \varepsilon}(\varepsilon, q_{n+1}^*(\varepsilon)) + \frac{\partial^2 g_n}{\partial q_{n+1} \partial q_{n+1}}(\varepsilon, q_{n+1}^*(\varepsilon)) \cdot \frac{\partial q_{n+1}^*}{\partial \varepsilon}(\varepsilon) = 0 \tag{B.47}$$

$$\implies \frac{\partial q_{n+1}^*}{\partial \varepsilon}(\varepsilon) = -\left\{ \frac{\partial^2 g_n}{\partial q_{n+1} \partial q_{n+1}}(\varepsilon, q_{n+1}^*(\varepsilon)) \right\}^{-1} \cdot \frac{\partial^2 g_n}{\partial q_{n+1} \partial \varepsilon}(\varepsilon, q_{n+1}^*(\varepsilon)) \tag{B.48}$$

replacing in (B.46), we have that for a fully implicit scheme,

$$\mathrm{D}^2 W_n(\varepsilon) = \frac{\partial^2 g_n}{\partial \varepsilon \partial \varepsilon}(\varepsilon, q_{n+1}^*(\varepsilon)) - \frac{\partial^2 g_n}{\partial \varepsilon \partial q_{n+1}}(\varepsilon, q_{n+1}^*(\varepsilon)) \cdot \left\{ \frac{\partial^2 g_n}{\partial q_{n+1} \partial q_{n+1}}(\varepsilon, q_{n+1}^*(\varepsilon)) \right\}^{-1}$$
$$\cdot \frac{\partial^2 g_n}{\partial q_{n+1} \partial \varepsilon}(\varepsilon, q_{n+1}^*(\varepsilon)) \tag{B.49}$$

$$\mathrm{D}^2 W_n(\varepsilon) \equiv \mathbf{D}_{n+1}^{ep} \tag{B.50}$$

where $\mathbf{D}_{n+1}^{ep}$ is known as the consistent tangent modulus at $t = t_{n+1}$.

B.1.5. Finite-element discretization of the i-DIR formulation

Let:

$$\boldsymbol{u} \approx u_i^h := \sum_{A=1}^{n} N_A u_{iA} = \mathbf{N}(x)\mathbf{u} \tag{B.51}$$

$$\boldsymbol{v} \approx v_j^h := \sum_{A=1}^{n} N_A v_{jA} = \mathbf{N}(x)\mathbf{v} \tag{B.52}$$

$$\varepsilon(\nabla\boldsymbol{u}) \approx \varepsilon(\nabla\boldsymbol{u}^h) := \sum_{A=1}^{n} B_A u_{iA} = \mathbf{B}(x)\mathbf{u} \tag{B.53}$$

$$\varepsilon(\nabla\boldsymbol{v}) \approx \varepsilon(\nabla\boldsymbol{v}^h) := \sum_{A=1}^{n} B_A v_{jA} = \mathbf{B}(x)\mathbf{v} \tag{B.54}$$

where N_A are the shape functions, $\mathbf{N}$ is the matrix of global shape functions, and $\mathbf{B}$ is the global strain-displacement matrix.

$$\mathbf{N} = \begin{bmatrix} N_1 & 0 & 0 & N_2 & \cdots & N_i & 0 & 0 \\ 0 & N_1 & 0 & 0 & \cdots & 0 & N_i & 0 \\ 0 & 0 & N_1 & 0 & \cdots & 0 & 0 & N_i \end{bmatrix} \tag{B.55}$$

$$\mathbf{B} = \begin{bmatrix} \mathbf{B}_1 & \mathbf{B}_2 & \mathbf{B}_3 & \cdots \mathbf{B}_i \end{bmatrix} \tag{B.56}$$

$$\mathbf{B}_i = \begin{bmatrix} \frac{\partial N_i}{\partial x} & 0 & 0 \\ 0 & \frac{\partial N_i}{\partial y} & 0 \\ 0 & 0 & \frac{\partial N_i}{\partial z} \\ \frac{\partial N_i}{\partial y} & \frac{\partial N_i}{\partial x} & 0 \\ 0 & \frac{\partial N_i}{\partial z} & \frac{\partial N_i}{\partial y} \\ \frac{\partial N_i}{\partial z} & 0 & \frac{\partial N_i}{\partial x} \end{bmatrix} \tag{B.57}$$

Substituting the approximations (B.51)-(B.54) into the linear variational problem (3.40) we obtain the linear system of equations defined in (3.41), where the tangent matrix and residual vector are defined as

$$\mathbf{K}_n := \alpha \int_{\Omega^h} \mathbf{N}^T \left\{ \nabla T(\boldsymbol{u}_n^h) \otimes \nabla T(\boldsymbol{u}_n^h) + (T(\boldsymbol{u}_n^h) - R)\nabla\nabla T(\boldsymbol{u}_n^h) \right\} \mathbf{N} \\ + \int_{\Omega^h} \mathbf{B}^T \boldsymbol{D}_{n+1}^{ep}(\varepsilon(\boldsymbol{u}_n^h))\mathbf{B}, \tag{B.58}$$

$$\mathbf{F}_n := \alpha \int_{\Omega^h} \mathbf{N}^T (T(\boldsymbol{u}_n^h) - R)\nabla T(\boldsymbol{u}_n^h) + \int_{\Omega^h} \mathbf{B}^T \sigma_{n+1}(\varepsilon(\boldsymbol{u}_n^h)), \tag{B.59}$$

which are constructed by numerically evaluating the element expressions and assembling their contributions into the global matrix and vector using standard finite-element techniques, see, e.g., (Hurtado & Henao, 2014).

B.2. Images in its original version (article version)

FFD   Elastic FEM   iDIR   Reference

Resampled

Difference

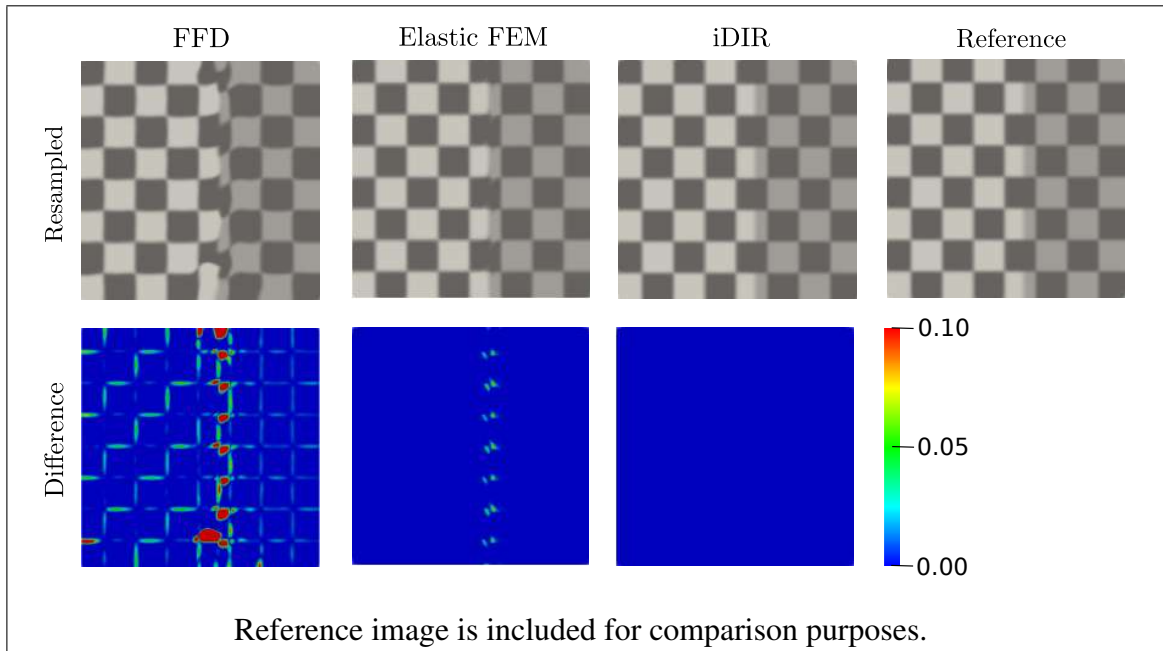Reference image is included for comparison purposes.

Figure B.1. Registration of synthetic dataset with sliding motion. (Top row) resampled images using FFD, Elastic FEM and i-DIR methods and Reference image, (bottom row) difference images. Colorbar indicates the absolute intensity difference between images.
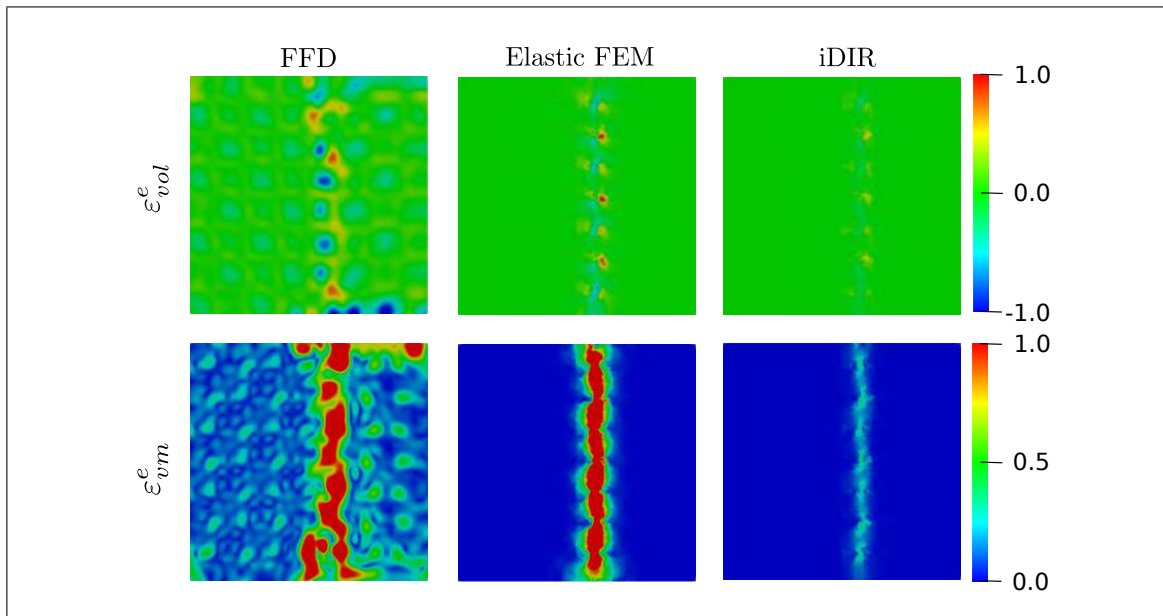
Figure B.2. Elastic deformation fields for the synthetic dataset with sliding motion resulting from the different registration methods: elastic volumetric strain (top row, colorbar displays strain magnitude), and elastic von Mises strain (bottom row, colorbar displays strain magnitude).
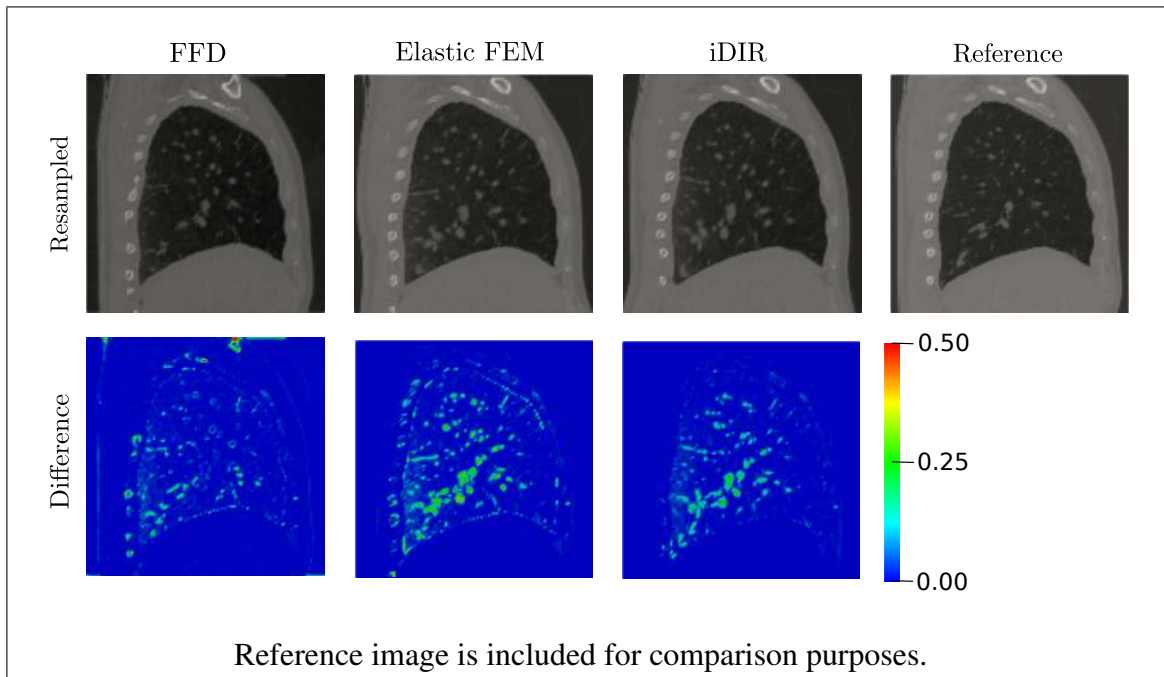
Figure B.3. Registration of the lung dataset and comparison between methods. (Top row) resampled images, (bottom row) difference images. Colorbar indicates the absolute difference between images.
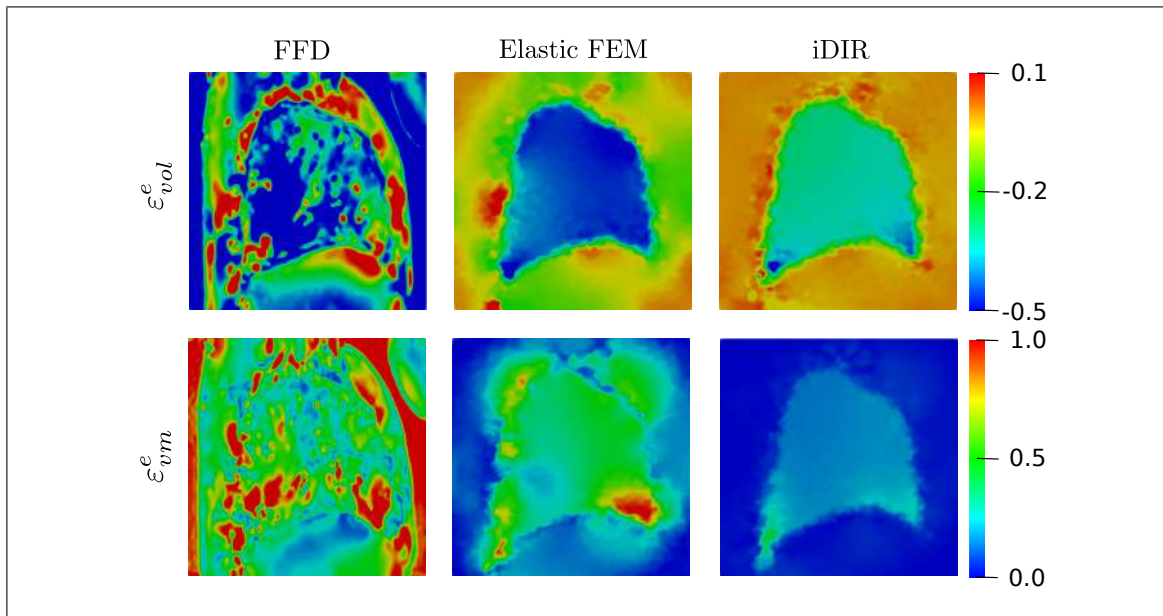
Figure B.4. Elastic deformation fields for the lung dataset resulting from the different registration methods: elastic volumetric strain (top row, colorbar displays strain magnitude), and elastic von Mises strain (bottom row, colorbar displays strain magnitude).

B.3. Processing time

Table B.1. Processing time of the lung dataset considering the meshing and the optimization scheme.

Model	Time [min]
FFD	46.3
Elastic FEM	1759.4
i-DIR	1828.8